University of Wisconsin Milwaukee

UWM Digital Commons

August 2020

Effect of Force and Confinement on Chemical Reaction Kinetics

Alejandro Boscoboinik
University of Wisconsin-Milwaukee

EFFECT OF FORCE AND CONFINEMENT ON

CHEMICAL REACTION KINETICS

by

Alejandro M. Boscoboinik

A Dissertation Submitted in

Partial Fulfillment of the

Requirements for the Degree of

Doctor of Philosophy

in Chemistry

at

The University of Wisconsin-Milwaukee

August 2020

ABSTRACT

EFFECT OF FORCE AND CONFINEMENT ON CHEMICAL REACTION KINETICS

by

Alejandro M. Boscoboinik

The University of Wisconsin-Milwaukee, 2020
Under the Supervision of Professor Wilfred T. Tysoe

This work studies model systems that are relevant to understanding the fundamentals of surface chemical processes. A Cu(100) single crystal surface modified by methyl thiolate species, formed from the adsorption of dimethyl disulfide, is used for modeling the effect of an external force in a chemical reaction. Furthermore, 2D-Zeolite is synthesized, characterized and postulated as a model system for studying chemistry in confined space. Furfural adsorption on Pd(111) is studied under different experimental conditions by means of infrared reflection-absorption spectroscopy. Furfural uptake experiments from sub-monolayer to multilayer coverages and sequential heating lead to an analysis of conformational changes and tilting angles as a function of coverage and temperature. Finally, surface self-assembly processes are explored by means of Monte Carlo simulations that produce results with potential use as a general computational model for studying the interconnection of distributed particles on surfaces.

To my parents Graciela and Jorge, my brothers, Simon and Anibal, and my partner Tecolota.

TABLE OF CONTENTS

LIST OF FIGURES

LIST OF TABLES

ACKNOWLEDGMENTS

Chapter 1: Introduction

The transformation of matter, in which there is a change in the chemical state of a substance involved, is known as chemical reaction. These transformations are often initiated by heat, light and electricity, and its study is covered by the fields of thermo- photo- and electro-chemistry. However, chemical reactions can be mechanically activated by the influence of a force. This belongs to the field of mechanochemistry, and that is the theme of the main body of the work described in this thesis. Mechanical activation is perhaps one of the oldest methods of inducing chemical reactions; Theophrastus of Eresus (c. 371 – c. 287 BC) reported, over two millennia ago, the mechanochemical reduction of cinnabar to mercury.[1] A myriad of scientists has proposed theoretical models for understanding the effect of a force (regularly in the form of stress, force per unit area) in a chemical reaction. Tracking back the connections between these scientists is quite clear that Prandtl [2] and Eyring [3] have led to the developments researchers have reported hereto. While the fields of investigation in which mechanochemistry has been addressed are vast, there seems to be a common ground. That is, at the fundamental level, the effect of a force is evidently influencing the system under study, and a reaction can still be treated as a thermally driven.[4] Recently a wide range of organic and inorganic mechanochemical syntheses have been reported, [5–9] and mechanochemical process are ubiquitous in biology.[10–12] Perhaps the most economically important class of mechanochemical reactions involves lubricant additives that react at a sliding interface to form friction- or wear-reducing films.[13] For example, the film formed by a common antiwear engine oil additive, zinc dialkyl dithiophosphate (ZDDP), has recently been shown to be mechanochemically induced.[14] Identifying how lubricant additives react at surfaces is important for reducing macroscopic and microscopic friction (e.g. in cars and micromachines).[15] In spite of

these experimental and theoretical advances, we have yet to perform experiments to achieve atomic-scale fundamental understanding on the validity of the data reported and theories proposed. In this work, mechanochemistry, and confinement effects, are explored at a fundamental level through controlled experiments in well-defined environments.

Chapter 2 describes the materials and methods used in this work and the importance of working in ultra-high vacuum (UHV) conditions.

A film of methyl thiolates produced by dosing dimethyl disulfide (DMDS) on Cu(100) will be the chemical model system utilized in Chapters 3 and 4 for studying mechanochemistry from a fundamental point of view. This methyl thiolate film has been considered, among other dialkyl disulfides, to be sufficiently reactive that it could form the basis of lubricants for sliding copper-copper interfaces at room temperature.[16] The mechanically induced rate of a chemical reaction is described by the Bell model.[17] There, the rate constant k for a reaction under an applied stress σ is given by $k(\sigma) = k_0 \exp(\sigma \Delta V^{\ddagger}/k_B T)$, where k_B is the Boltzmann constant, k_0 is the reaction rate in the absence of stress, $\Delta V^{\ddagger}$ is known as the activation volume, and T is the absolute temperature. While exponential increases in reaction rates with stress have been reported, there are currently no quantitative measurements on well-defined model systems. This is addressed in Chapter 3 by using contact-mode Atomic Force Microscopy (cmAFM) to measure the kinetics of mechanochemically induced C-S bond cleavage in methyl thiolates on Cu(100) in UHV. The mechanochemical reaction is studied by analyzing the evolution of the topography of the surface as a function of time at various contact pressures.

Chapter 4 describes experiments corresponding to the study of the methyl thiolate film under the influence of both normal and directional lateral stress. There, we analyze topography changes

resulting from sliding, as a function of dwell time at a specific load of the AFM tip on top of the sample.

In Chapter 5, we provide a strategy for the study confinement effects by first exploring the trapping of noble gases in 2D-aluminosilicate, and then exploring an alternative, inexpensive, bulk synthesis method for the aforementioned 2D-material.

While being of great practical importance, the field of mechanochemistry is still significantly unexplored at the fundamental level, both experimentally and theoretically. Aiming at understanding mechanistic and kinetic aspects of force-induced reactions, the results of this work enable placing descriptions of mechanochemical processes on a firm theoretical footing. This work is a step forward toward the objective of making quantitative predictions of mechanochemical reactions.

Other related projects are included as Appendices. A precursor for obtaining more valuable feedstocks, furfural, is studied in Appendix 1 and the structural changes of furfural adsorbed on a Pd(111) single crystal primarily measured by surface infrared spectroscopy is studied. Appendix 2 describes work that was started before arriving in UWM, but which I actively continued while at UWM, namely, developing strategies for producing directed nanoscale self-assembled molecular structures using Monte Carlo simulations. Some of the strategies that were developed were later expanded and applied experimentally in work lead by Dr. Dustin Olson. This appendix includes only the prior work I led and my contributions to the collaboration with Dr. Olson as well as future relevant plans related with the project.

Chapter 2: Materials and Methods

2.1 Introduction

Fundamental surface-science studies generally involve investigating well-defined model systems at the atomic scale, i.e.: using clean, well-defined single crystal surfaces that can then be exposed to adsorbates. These adsorbates can potentially diffuse on the surface, interact with each other by short- or long-range interactions to form superstructures, induce restructuring of the substrate, and/or undergo chemical reactions. Therefore, careful preparation of the sample and the reactants is of crucial importance to obtain reproducible results related to the processes occurring at the atomic scale. Working in ultrahigh vacuum (UHV) conditions (where $P < \sim 1x10^{-9}$ Torr) is necessary to ensure the rate of adsorption of background species is low enough so that an experiment can be carried within hours with the minimum amount of contamination. Under these conditions, the mean-free path of the molecules is generally larger than the dimensions of the experimental vacuum chamber, so that gas-phase collisions become rare events. Hence, on the time frame of the experiments, gas-phase reactions can be ignored and attention focused on studying surface processes of interest. This allows adsorbates to be introduced in a controlled manner. Taking these issues into consideration, UHV conditions are used for all experiments unless specified otherwise. The strategies that are used to obtain such conditions and the experimental techniques that can be used under these conditions are described below.

2.2 UHV Technology

Stainless-steel chambers are the basis for our experimental apparatus, which is held under ultrahigh vacuum conditions to control the adsorption of molecules and diminish the influence of contaminants from the background gases adsorbing onto the sample.

2.2.1 UHV Chambers

Stainless-steel chambers contain the experimental environment under ultrahigh vacuum conditions. They are capable of accommodating the needed UHV-compatible equipment through flanged ports. These consist of items such as windows, leak valves, sample manipulators, spectroscopic probes, vacuum pumps, etc. UHV seals are achieved by using knife-edged unions, also known as Conflat flanges, on all the ports where the parts are connected. These sharp edges meet on both sides of copper gaskets to produce a tight and reliable leak-free seal between the two components connected. The process for achieving the UHV conditions after the chamber is closed involves a sequence of adequate pumping mechanisms. However, by merely pumping the chamber is not sufficient. This is primarily because of the low rate of water desorption from the inner walls of the chamber that limits the base pressure than can be obtained in the chamber. Therefore, in order to accelerate the water desorption, the chamber is heated by a heating tape attached to the outer surface of the stainless-steel, which is covered by aluminum foil to proceed to perform a bakeout process. The chamber temperature is monitored to adjust the current through the resistive tape to achieve a temperature of approximately 120 $^{\circ}$C for approximately 48 Hs. The aluminum foil helps to keep the chamber at consistent temperatures preventing heat loss and the appearance of cold spots. After cooling the system, the necessary UHV conditions are achieved. Typical pressures after bakeout are in the order of $\sim 10^{-11}$ Torr.

The experimental apparatus used for the work here presented is mounted on a rigid frame that supports the whole vacuum system. In some cases, the frame is supported on pneumatic air legs to minimize the influence of external vibrations for experiments that are sensitive to changes in the environment, such as scanning probe microscopies. In the UHV atomic force microscope (AFM), scanning tunneling microscope (STM) apparatus that was primarily used during this work, the two

main vacuum vessels are used as a preparation chamber in which the samples can be cleaned and characterized, and a scanning probe microscopy (SPM) chamber that is used to image the surface, separated from each other by a gate valve. Each vessel is separately pumped by an ion pump. The preparation chamber is connected to a turbomolecular pump through a small high-pressure cell (at the right of Figure 2.1). The SPM chamber is connected to a second turbo molecular pump through a load lock (at the left of Figure 2.1). All chambers can be isolated by gate valves (VAT Inc.). The introduction or removal of samples and scanning probe tips from the system can be performed using a transfer arm that connects the load-lock to the SPM chamber. Furthermore, the sample or tip holder can be transferred from the SPM chamber to the preparation chamber using a second transfer arm (MDC LLC) which has a mounting stage similar to that in the SPM chamber. These stages have electrical connections to allow the temperature measurement (through a thermocouple) and controlled electron-beam heating. Further details on the design of this versatile assembly are well described elsewhere.[18] In this work, Auger electron spectroscopy (AES) and low-energy-electron diffraction (LEED) techniques are included as an Omicron LEED/Auger system mounted in the preparation chamber. An ion gun is used for Ar^+ sputtering for cleaning purposes. At the SPM chamber, the microscopy technique utilized in this work is contact mode Atomic Force Microscopy (cmAFM).
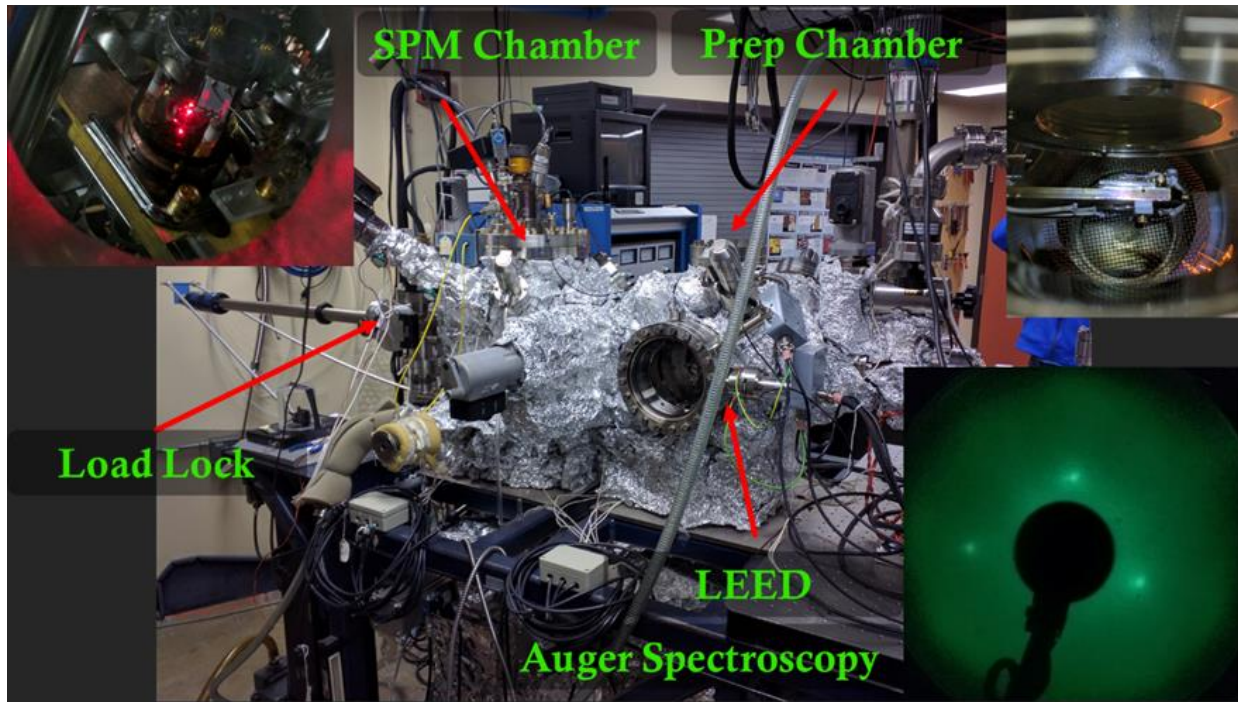
Figure 2.1: UHV Chamber Experimental Setup

2.2.2 Vacuum Pumps

There are generally four different types of pumps utilized to achieve UHV conditions, namely, mechanical (rotary) pumps, turbomolecular pumps, diffusion pumps, and ion pumps.

2.2.2.1 Rotatory (Mechanical) Pumps

Rotary pumps produce mechanical rotary work, which is translated into fluid movement. Even though only pressures on the low milliTorr range can be achieved, due to the nature of the pumping mechanism, they are crucial components for achieving UHV conditions. They are utilized for rough pumping and backing turbomolecular and diffusion pumps. They consist of a rotor in which vanes are mounted, see Figure 2.2. While rotating, the vanes displace the gas inside the housing, promoting suction from one side and subsequent displacement of the gas towards the exhaust through the rotational cycle inside the circular cavity. These moving parts need to be tightly sealed

and lubricated, which is achieved by continuous exposure to a lubricating, low-vapor pressure vacuum oil.
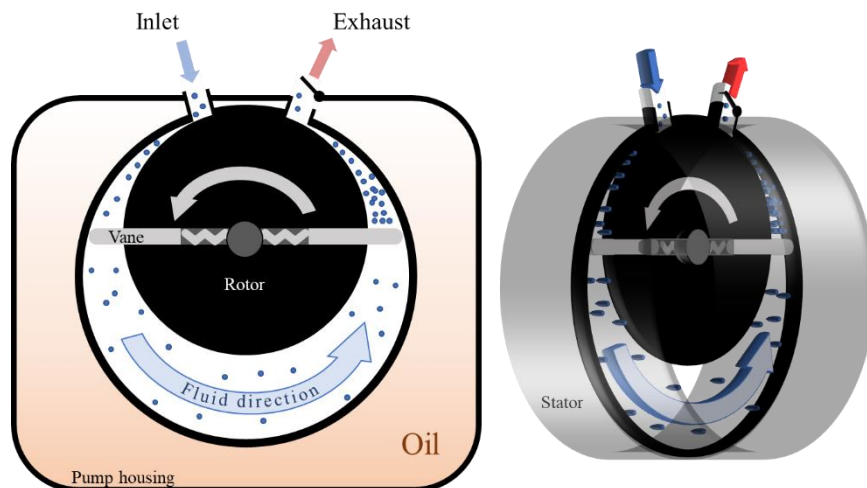
Figure 2.2: Mechanical pump diagram.

2.2.2.3 Turbomolecular Pumps

Turbomolecular pumps, invented in 1958 by W. Becker,[19,20] are mechanical ultrahigh vacuum pumps. Within a reasonable period of time, turbomolecular pumps are capable of reducing the pressure of the pumped system from an intermediate vacuum ($\sim10^{-4}$ Torr, obtained using a rotary pump) to good high-vacuum conditions ($\sim10^{-9}$ Torr). They consist of sets of blades organized as displayed in the diagram of Figure 2.3. Within these sets of blades, the stator and rotor blades can be recognized. The molecules which enter the inlet (from the vacuum system), collide with the moving blades and receive an additional momentum in the moving direction of the blade producing the displacement of the gases towards the next stages. This mechanism repeats until the accelerated molecules travel through the whole set of stages to leave the pump through an outlet. These expensive devices are to be backed by a mechanical (rotary) pump before they started and while they are being turned off. A spin-down process, in which a venting valve is used to allow gas into

the turbomolecular pump, can accelerate the process. A backing pump is needed because the rotational speed of these blades under normal operation is ~ 75 thousand revolutions per minute (krpm) and, to reach and operate under those conditions, the heat generated by frictional processes and molecular collisions needs to be minimized. In order to reduce the friction, the operation is started when the pressure on the pump is at ~10^{-3} Torr, and magnetic bearings are generally used to minimize energy dissipation. A major drawback of mechanical and turbomolecular pumps is their introduction of vibrations to the experimental system. This is especially inconvenient for vibrational-sensitive experiments, such as in the case of this work when using AFM or STM.
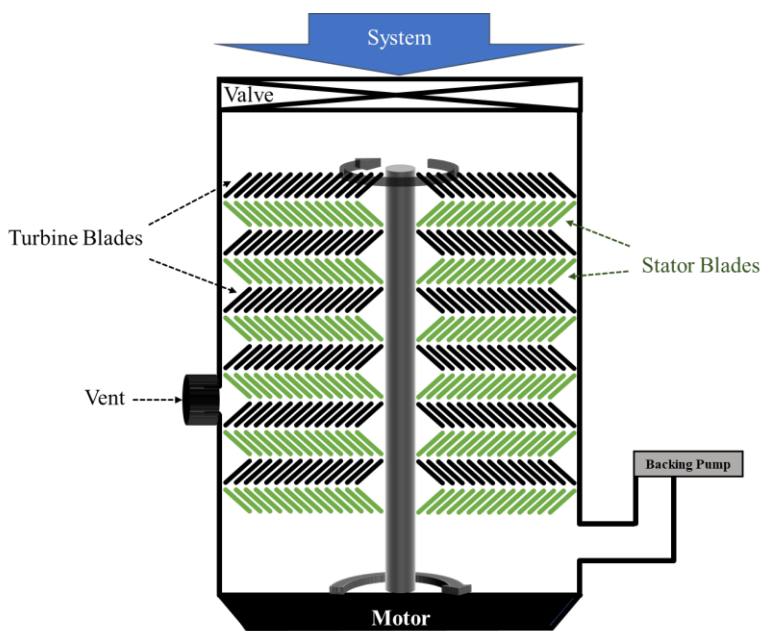
Figure 2.3: Turbomolecular pump schematic diagram.

2.2.2.4 Diffusion Pumps

Oil diffusion pumps are high-speed pumping devices capable of achieving pressures down to the 10^{8-9} Torr. Invented in 1915 by Wolfang Gaede,[21] they consist of a jet shaped structure (see schematics in Figure 2.4). A high-speed upwards flow is generated by boiling oil of low vapor pressure (to prevent back-streaming of the oil into the chamber). This high-speed vaporized oil is

then deflected by the jet type design and then leading to a net flow of gasses away from the vacuum system. The latter causes the system pressure to drop, and the oil inside the diffusion pump is condensed by the cooled walls of the device and is recovered at the bottom to restart the cycle leaving the entrained gas to be removed by means of a rotary pump. While these pumps have the benefit of simplicity, low cost, high pumping speed, and low final pressures, the backstreaming of oil is a risk that has to be carefully managed. If either the cold trap or the backing pump experience operational problems, the vacuum system could be exposed to diffusion pump oil. In this case, the pump is often controlled by interlocks that turn off the diffusion pump if the pressure becomes too high or the cooling is impeded.
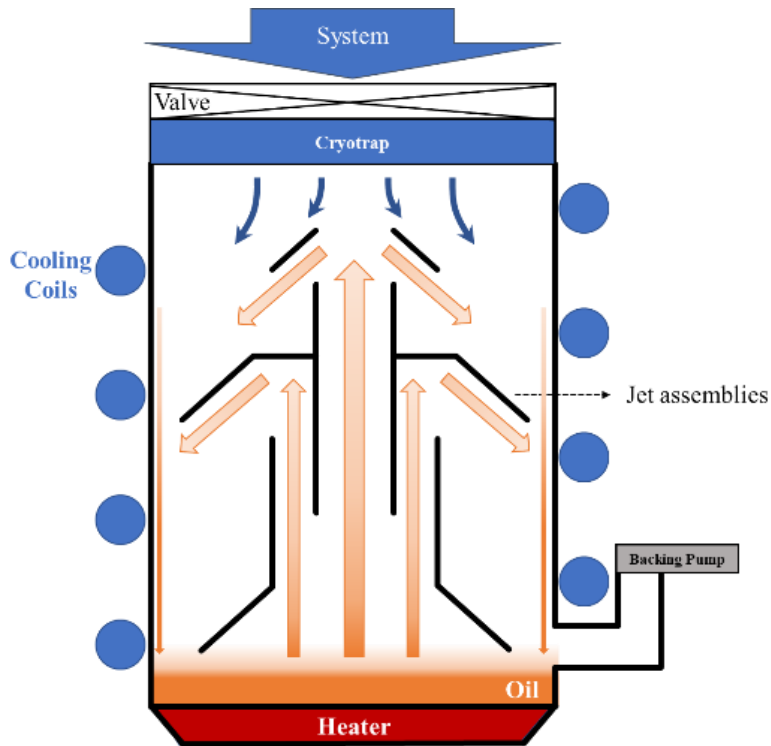
Figure 2.4: Diffusion pump schematic diagram.

2.2.2.5 Ion Pumps

Ion pumps are the modern primary choice for achieving UHV conditions. With these pumps, pressures can reach as low as 10^{-11} Torr and have the benefits of not introducing vibrations to the system because of the lack of moving parts, as shown in Figure 2.5. The latter means that the pump does not require oil and backstream is not a problem. These long-lasting pumps work by accelerating ionized molecules (from the anode) towards plates (cathode) generally made of a titanium alloy. The accelerated molecules collide with the cathode with enough kinetic energy to be buried in it and potentially cause sputtering of the titanium plates leaving clean reactive material exposed for continuing this process. This is also known as gettering. High DC voltage applied between the anode and the cathode initiate the ionization by plasma discharge. This is enhanced by the acceleration of electrons in helical trajectories (Penning trap), as a result of the presence of strong magnetic fields (1-2 kG), increasing the probability of collisions with incoming gas molecules. Furthermore, ion pumps are advantageous devices in the sense that they do not need to be backed by a mechanical pump. However, the range of operation is pressures lower than 10^{-5} Torr, which means that an ion pump cannot be started until the system is operating under this condition. In terms of speed, ion pumps are slower than turbomolecular and diffusion pumps for the same physical size and more expensive. Finally, it should be noted that non-reactive gases such as argon will be pump very slowly because they are not efficiently gettered. Prolonged exposures to this noble gas should be avoided since the chemisorption assisted process will be negligible, and the continuous sputtering of the titanium surfaces will translate into decreasing the lifespan of these expensive pumps.
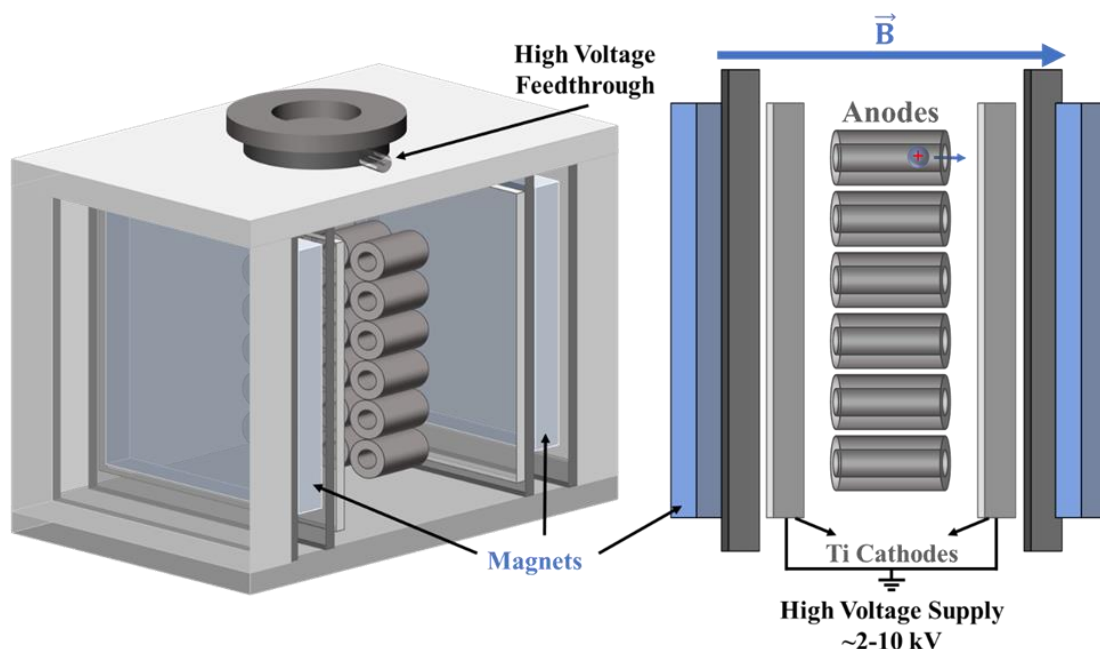
Figure 2.5: Ion pump diagram.

2.2.5 Gas Handling Line and Chemical Purification

In the vacuum equipment used in this research, gas-handling systems constructed of Pyrex is utilized to contain and introduce gases into the UHV chambers through high-precision variable leak valves. These assemblies are generally mounted to the chamber frame, and built in-situ by a glassblower. A schematic diagram of a gas handling line is shown in Figure 2.6. Usually pumped by diffusion and rotary mechanical pumps, these gas-handling lines can reach pressures of 10^{-7} Torr without baking. The pressure is measured by using a cold cathode gauge which is sensitive in the 10^{-7} Torr to milliTorr range. Above that pressure, a diaphragm and/or capacitance manometer in the milliTorr to Torr range is used. The chemical samples, commonly contained in glass vials (for vapors or liquids) or cylinders (for gasses), are attached to the gas line via ¼" Swagelok valves. The liquid samples are purified by sequential freeze-pump-thaw cycles before being loaded to the gas-line. Often, two or more sections of this glass manifold can be isolated by

12

closing glass valves with Teflon stopcocks to isolate each section to contain a specific sample. The latter allows the introduction of more than one gas or vapor into the chamber simultaneously or sequentially, preventing the time delay spent on evacuating the line for the sequential scenario. Once loaded, the gas or vapor is introduced in the chamber by using variable leak-valves, connected to the gas line sections by glass-to-metal seals. The purity of the gases can also be monitored after leaking into the chamber using a mass spectrometer.
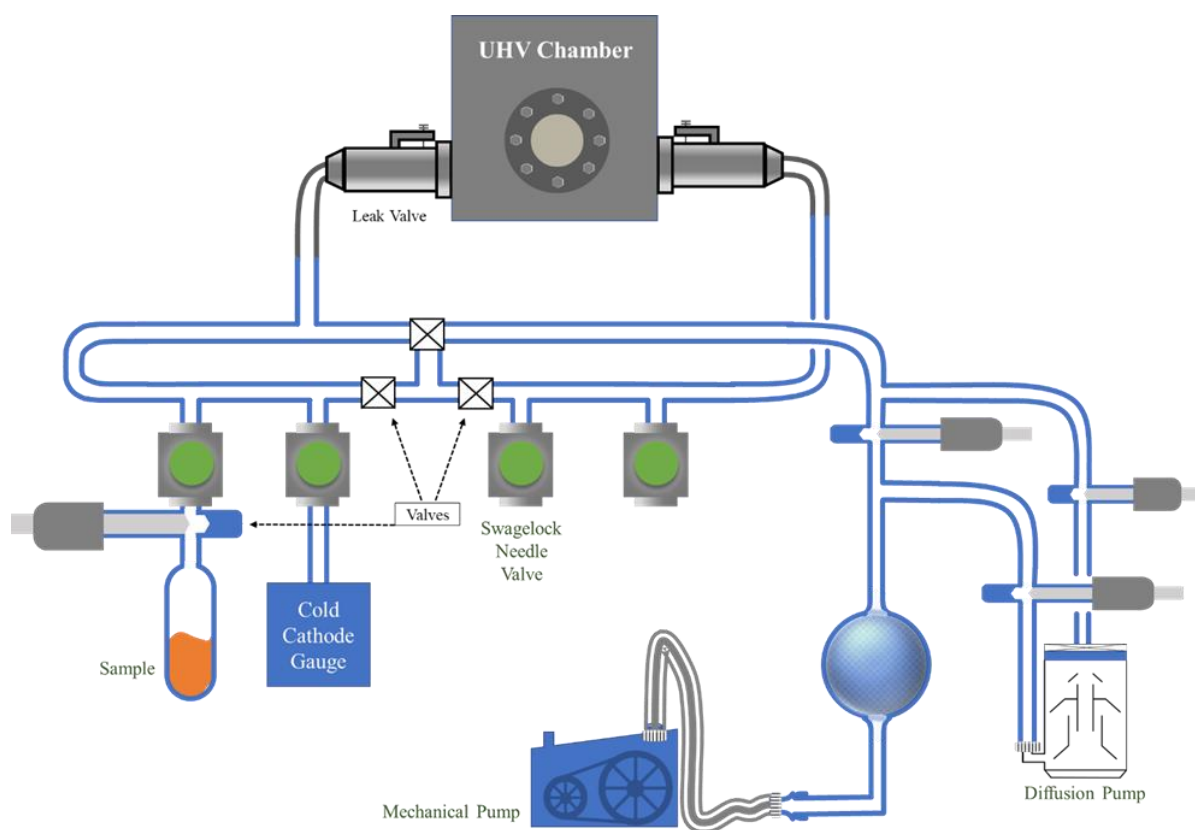
Figure 2.6: Gas Handling Line diagram.

13

2.3 Fundamentals of the Techniques

2.3.1 Contact mode – Atomic Force Microscope (cmAFM)

The Atomic Force Microscope (AFM), invented in 1985 by IBM scientists Gerd Binning and Calvin Forrest Quate,[22] is a microscopy technique without optical lenses. Images are collected by scanning a fine tip over the surface and measuring the topography from the variation in the height of the tip as a function of position. Generally, the height of the tip is measured by reflecting a laser beam from the rear surface of a flat cantilever and directed to a quadrant photodetector. On the other side of the cantilever, there is a tip, ideally ending in a single atom (see Figure 2.7). When the tip interacts with the surface, the cantilever bends vertically and twists laterally, causing the laser beam to deflect. The deflection is sensed by the quadrant photodetector. The vertical and lateral displacements on the detector provide detailed information on both normal and lateral properties related to forces and friction, respectively.[23] This information can be used to produce topography images as well as friction maps of the surface and investigate surface properties at the atomic scale.
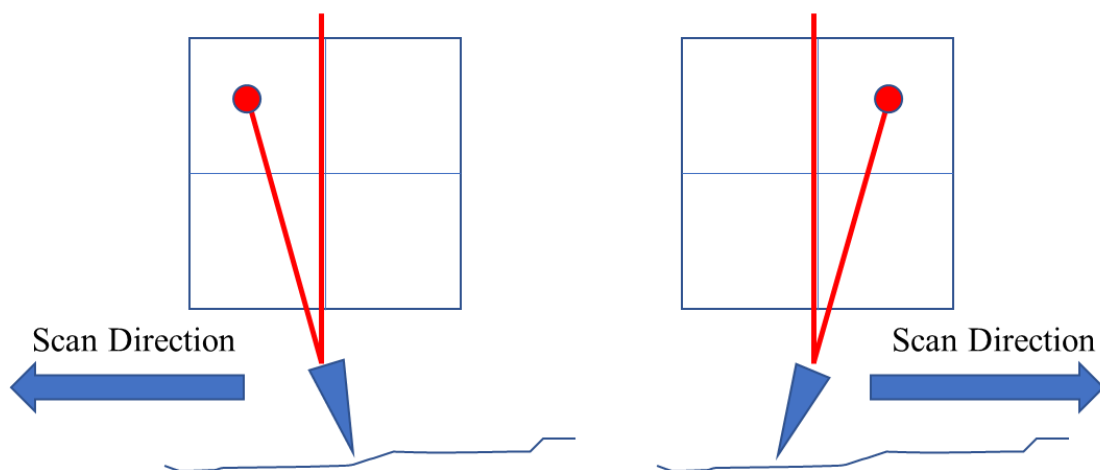
Figuire 2.7: Schematic of quadrant photodetector showing the laser deflection from the rear surface of the cantilever while the tip rasters the surface in different directions, shown in the left and right images.

In contact mode atomic force microscopy studies, the normal load is held constant by a feedback loop mechanism that controls the vertical position of the cantilever using a piezoelectric material. Hence, scanning probe microscopies generally work by taking advantage of expanding or contracting a piezoelectric material under an applied voltage across the crystal. The small change in size per unit cell adds up over billions or trillions of unit cells and produces measurable but very precise size differences. By scanning the surface and keeping the normal load constant (constant deflection) by means of a feedback loop, the applied correction voltage maps the surface topography of the sample. The quadrant photodetector outputs four voltages proportional to the intensity of light captured by each quadrant. When the spot moves, the light is distributed differently, increasing in some quadrants at the expense of signal decrease on the other quadrants. By the mathematical manipulation of the four signals, the vertical (due to cantilever bending) and lateral (due to cantilever twisting) deflections of the laser can be measured. This provides a measurement of the local normal and lateral force respectively.[24]

Dictated by Hook's law, the tip-surface interaction force F_N is determined by the bending of the cantilever Δz, which is sensed by the deflections of the laser from its equilibrium position,

$$F_N = k\Delta z \tag{2.1}$$

where k is the cantilever spring constant. Figure 2.8 shows a scanning electron microscopy (SEM) image of an n-type Silicon tip of a nominal radius of 8 nm and a cantilever constant of 0.5 N/m. The spring constant for normal bending can be calculated from its geometry [25] as,

$$k = \frac{Ewt^3}{4l} \tag{2.2}$$

where E is Young's modulus of the material, w is the width, l is the length, and t the thickness of the cantilever. These dimensions can be obtained from SEM images. Another way to determine the thickness is from the resonance frequency of the cantilever, f as,

$$t = \frac{2\sqrt{12}\pi}{1.875^2} \sqrt{\frac{\rho}{E}} f l^2 \tag{2.3}$$

where ρ, is the mass density of the material. In the case of silicon, $\rho = 2330$ kg/m^3 and $E = 1.69 \times 10^{11}$ N/m^2, then thickness becomes,

$$t = 7.23 \times 10^{-4} \text{ s/m} \times f l^2 \tag{2.4}$$

The spring constant and parameters from force distance (F/z) curves such as the ones depicted in Figure 2.9 are used for converting the precise force signal from mV into nN.
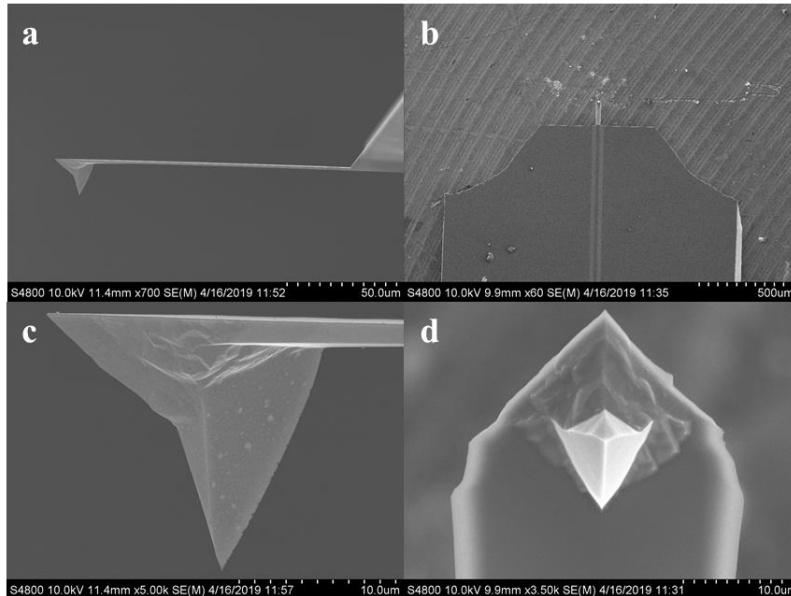
Figure 2.8: Scanning electron microscopy images of a commonly used commercial n-type silicon AFM tip. (a) Side view of the cantilever, (b) top view of the cantilever, (c) and (d) close-up views of (a) and (b) respectively. Images were taken in collaboration with Dr. Dustin R. Olson.
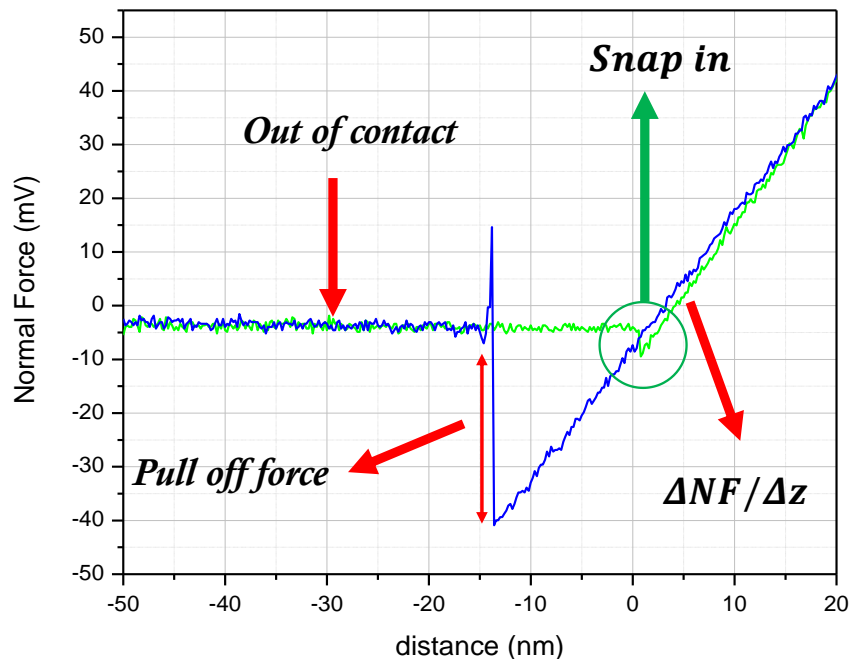
Figure 2.9: Force distance curve, the green line originating from left (-50 nm to 0 nm) shows the out -of- contact regime of the linear lever approach (here the distance axis corresponds to vertical displacement, z in nm) which continues until the long-range attractive interaction forces cause the tip to "snap-in" until it is balanced by repulsive forces between the tip and the surface to produce a vertical deflection of ~-5 mV (Normal Force axis, NF). After snap-in, the tip and the surface are now in contact, and the vertical position displacement continues to produce a linear increase in the vertical deflection of the laser with a slope given by $\Delta NF/\Delta z$ as dictated by Hooke's law. Once the end of the approaching distance has been reached (+20 nm for the depicted scenario), then the tip retracts (blue line). As the cantilever moves away from the surface, it is observed that the interaction forces exceed the snap-in forces due to adhesion forces leading to the so call "pull-off" force needed to detach the tip and return to the out of contact regime situation and the force to achieve this characterizes the interfacial surface adhesion at the nanoscale.

The possibility of carefully looking at the adhesion forces from F/z curves, topography images of the mapped surface along with friction maps, can be correlated, for example, to a certain degree of physical/chemical change.[26] For instance, removal of material either by chemical reactions or lateral displacement of the surface species will lead to changes in depth and possibly friction. Through chemical reaction, it is possible not only to remove but also add surface material.[27,28] Topographically, indistinguishable surfaces could present distinctive friction characteristics and, therefore, different properties.

2.3.2 Infrared Reflection-Absorption Spectroscopy (IRRAS)

Being one of the most powerful structural techniques in surface sciences, IRRAS, a nondestructive technique, takes advantage of dipole selection rule, which states that, with p-polarized infrared light (Ip) incident of the surface, only adsorbates with vibrational modes perpendicular to the surface are exited. This is because parallel polarized radiation (Ip) with respect to the plane of incidence produces a phase shift dependent on the angle of incidence, leading to the intensity of the component of the radiation normal to the surface being almost twice as intense as the incident radiation when working at a grazing angle of approximately 82 degrees. However, for the case of perpendicular polarized radiation (Is), the phase shift is nearly 180° for all incidence angles, the net amplitude of the IR radiation parallel to the substrate surface is zero as shown in Figure 2.10. Vibrational modes of the adsorbed molecules that are perpendicular to the surface promote the creation of a dipole in the substrate to screen the charge as shown in Figure 2.11 (left), the net effect is to increase the overall dipole moment. However, for the case of vibrational modes parallel to the surface the image charges on the surface cancel the dipole moment and thus they are IR inactive, see Figure 2.11 (right).
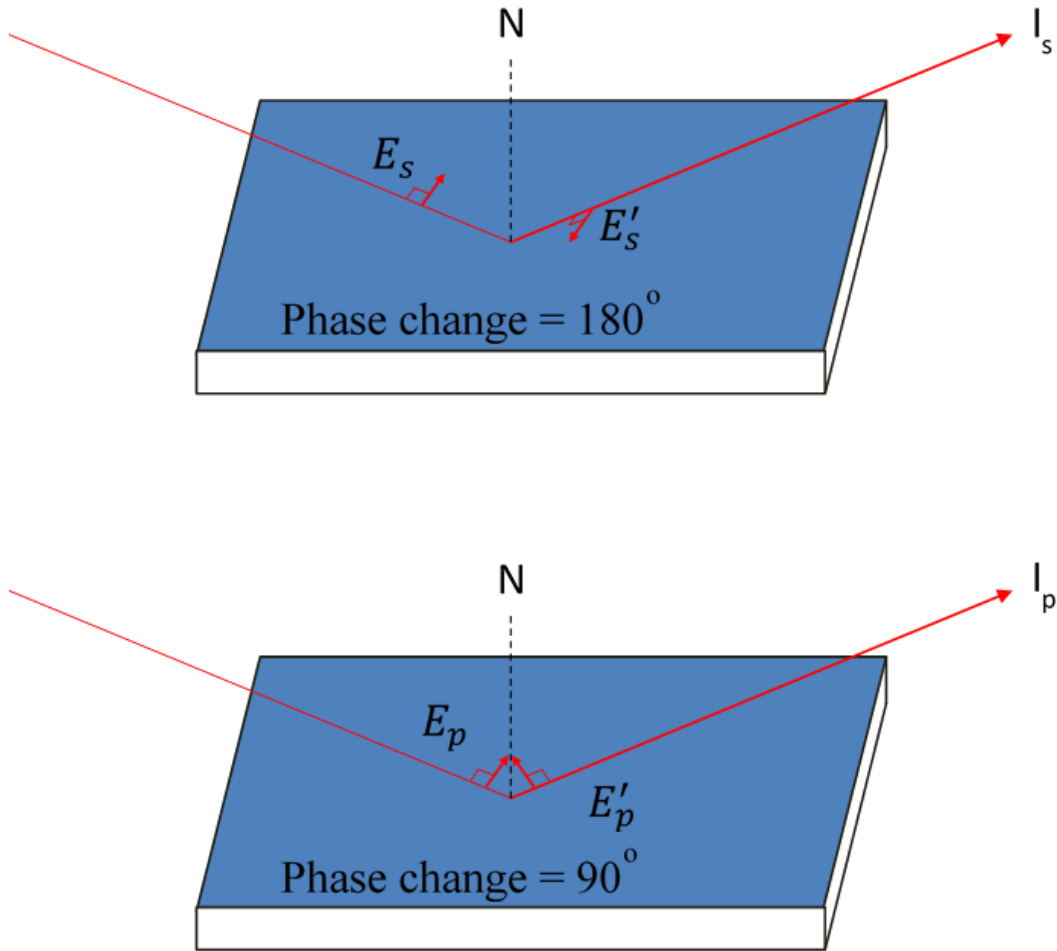
Figure 2.10: Phase change of polarized light Is on top, and Ip bottom, upon reflection from the metal surface
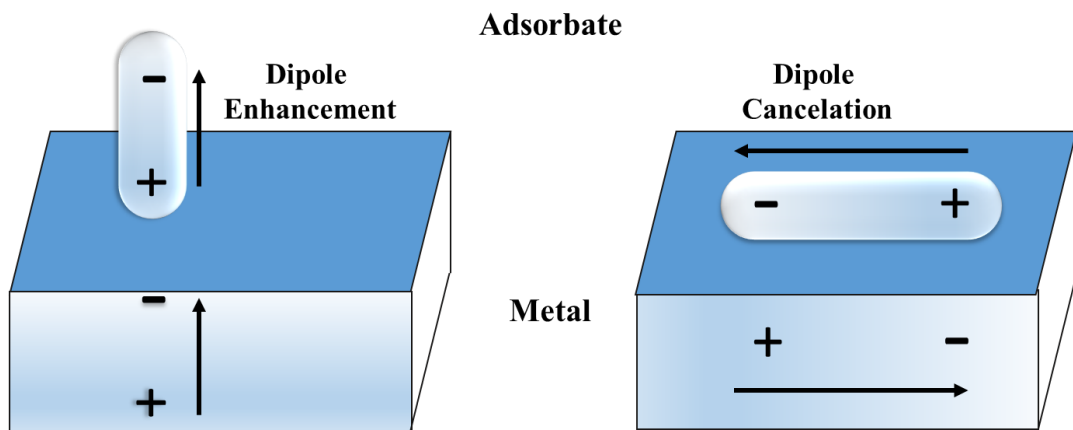
Figure 2.11: Image of Dipole effect.

The differential reflectance spectrum is often obtained as the difference between the reflection spectrum of the clean substrate and the covered substrate relative to the clean substrate, ΔR/R, and it is proportional to the surface coverage. Vibrational frequencies and intensities serve as information for identifying the surface species and elucidating molecular orientation with respect to the surface and adjacent molecules. Optimizing the incident grazing angle of the IR light leads to signal to noise ratios capable of identifying molecular species at sub-monolayer coverages.

2.3.3 X-ray Photoelectron Spectroscopy (XPS)

X-ray Photoelectron Spectroscopy was developed in the mid-1960s by Kai Siegbahn, and the technique was originally known as Electron Spectroscopy for Chemical Analysis (ESCA). In 1981 the Nobel Prize in Physics was given to Siegbahn for this discovery. XPS for surface analysis is performed by irradiating the sample with monochromatic soft x-rays which causes photoemission of electrons from the core and valence energy levels where the binding energy of the initial electron is related to the kinetic energy of the emitted electron.

As the energy of the incident beam ($h\nu$), and work function of the metal (Φ) are known, the binding energies (E_{BE}) after detection of the kinetic energy of the ejected electrons (E_{KE}) can be calculated according to,

$$E_{KE} = h\nu - E_{BE} - \Phi \qquad (2.5)$$

A spectrum of number electrons detected versus their respective kinetic energy is obtained and the peaks are labeled using spectroscopic notation. The binding energy of the electron with respect to vacuum, E_{BE}, serves as a fingerprint of the chemical bonding and structure of the material under

study. Due to the short mean free path of the ejected electrons that come from subsurface regions, this technique is predominantly surface sensitive.
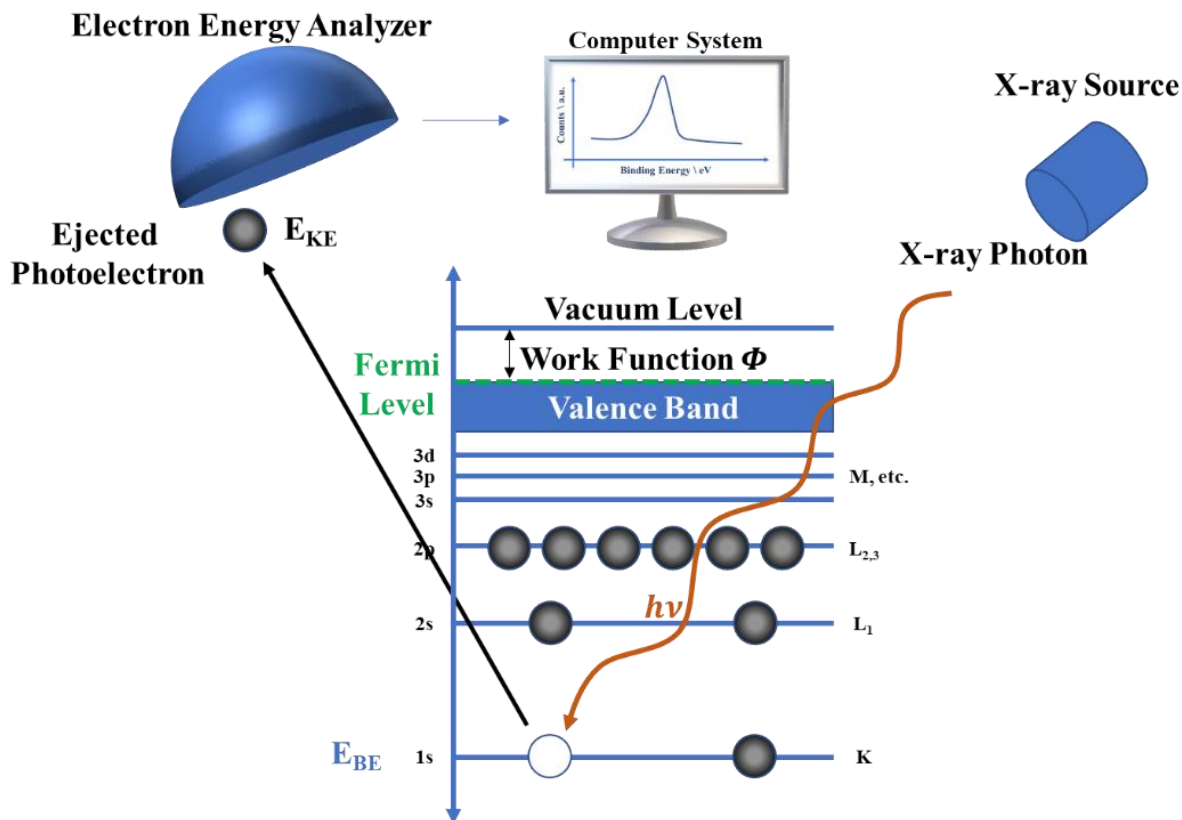
Figure 2.12: XPS schematic diagram for X-ray excitation of a 1s core electron.

It is important to note that the binding energy of a core electron does not only depend on the level from where it originates (providing elemental composition) but also from the chemical environment and the formal oxidation state of the atom due to changes in the nucleus screening by the different electronic configuration. By comparing the shifts with reference values, quantitative information related to the chemical state and bonding can be determined.

Chapter 3: Normal-Stress Induced Mechanochemical Decomposition of Methyl Thiolate on Copper (100)

3.1 Introduction

Mechanochemical reactions are stress-induced processes in which the shape of the Born-Oppenheimer potential energy surface is modified by an external force to reduce the energy barrier between metastable minima, where the transition over the modified energy barrier is thermally assisted and thus depends on temperature. Mechanochemical kinetics are often described by the Bell model,[17] where the rate constant for the reaction in the absence of an external force is given by $k_0 = Aexp\left(-\frac{E_{act}}{k_BT}\right)$, where E_{act} is the activation energy, k_B is the Boltzmann constant and T the absolute temperature. In this model, an external force F modifies the energy profile by a potential given by $-Fx$. To first order, this provides a simple equation for the reaction rate constant $k(F) = k_0 exp\left(\frac{F\Delta x^{\ddagger}}{k_BT}\right)$, where $\Delta x^{\ddagger}$ is referred to as the activation length, defined as a distance from the initial to the transition state. Since experiments generally measure the contact stress σ (force per unit area), the Bell model is often written as $k(\sigma) = k_0 exp\left(\frac{\sigma\Delta V^{\ddagger}}{k_BT}\right)$, where $\Delta V^{\ddagger}$ is an activation volume, that is, the activation length multiplied by the area over which the applied stress acts.

Similar concepts of the way in which energy landscapes are modified by an external force, were first used by Prandtl [2] to model crystal plasticity, and by Eyring to model energy dissipation during fluid shear (its viscosity).[29] It was subsequently used to explain a wide range of stress-induced phenomena [30] such as material fracture,[31] rubber friction,[32] and atomic-scale friction and wear;[33,34] note that mechanically induced processes are ubiquitous in chemistry, physics and materials science.

Exponential stress dependences of mechanochemical reaction rates have been found experimentally,[14,35–40] leading to measured values of the activation volume of ~10 Å^3. However, the activation volume of a mechanochemical reaction cannot generally be predicted *a priori*. This occurs for a number of reasons. Neither the nature of the elementary steps in the reaction pathway nor the direction of the force with respect to the energy landscape are generally known for the systems that have been studied hitherto.[41] This lack of a theoretical framework with which to analyze and ultimately predict the rates of tribo/mechanochemical reactions, has impeded the growth of the field of mechanochemistry and the development of novel lubricants, or the design of new mechanochemical syntheses. As a result, the subfield of mechanochemistry is significantly less well developed than other fields of chemistry.

The experimental issues are addressed by accurately measuring the normal-stress induced decomposition kinetics of methyl thiolate ($CH_3–S_{(ads)}$) overlayers on Cu(100), by an atomic force microscope (AFM) tip in ultrahigh vacuum (UHV) (See Figure 3.1). This reaction has been implicated as a crucial step in the gas-phase lubrication of copper by dimethyl disulphide (DMDS).[42–44]

3.2 Experimental Methods

Experiments were carried out using an RHK Variable Temperature Ultrahigh Vacuum (UHV) 750 atomic force microscope (AFM) operating at a base pressure of ~2×10^{-10} Torr following bakeout. The apparatus also contained an analysis chamber for sample cleaning and was equipped with a Scienta Omicron SPECTALEED combined low-energy electron diffraction (LEED)/Auger system for assessing sample cleanliness and crystalline order. The chamber was also equipped with a Dycor quadrupole mass analyzer for leak checking and background gas analysis. The Cu(100) single crystal was cleaned by Argon ion bombardment (~1 kV, ~2 µA/cm^2) and then by annealing

to ~850 K to remove any surface damage induced by the cleaning procedure. A saturated overlayer of methyl thiolate species was prepared by dosing a clean Cu(100) sample held at ~298 K in UHV by background dosing at a pressure of 1×10^{-8} Torr of dimethyl disulphide (DMDS, Aldrich, 99.0% purity) for 200 s, where the pressure was measured using a nude ionization gauge included in the UHV chamber, (pressures were not corrected for ionization gauge sensitivity).[16] The DMDS was transferred to a glass bottle and attached to the gas-handling system of the vacuum chamber, and finally cleaned by several freeze-pump-thaw cycles. The purity was monitored using mass spectroscopy. Sulphur overlayers were prepared by decomposing a methyl thiolate overlayer on Cu(100) by heating to ~430 K for 300 s.
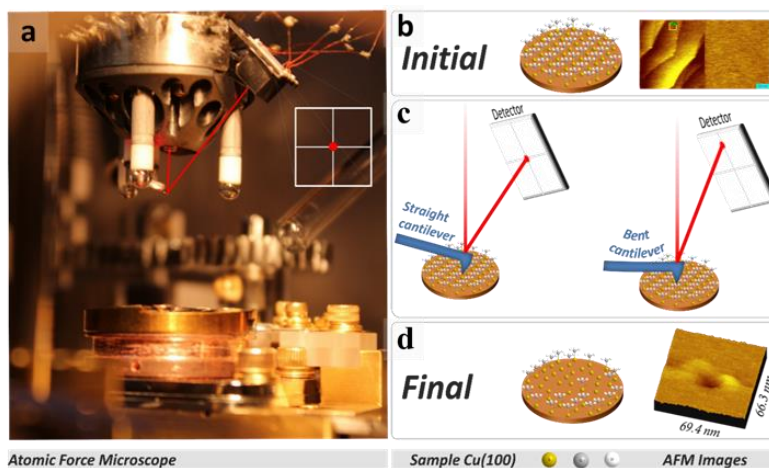
Figure 3.1: (a) Atomic Force Microscope head and sample photography through a UHV viewport, with a laser beam trajectory represented by red lines directed towards the center of the detector (illustrative inset diagram in white lines). (b) Schematic representation of the initial state of the surface and AFM topography image of the flat area of study within a surface terrace. (c) Schematic representation of the AFM tip before (left) and while exerting contact stress (right) on the sample. (d) Illustration and topography image of the surface area after an experiment.

Normal-stress-induced mechanochemical reactions were induced by applying a normal force using a silicon μ-masch (HQ:NSC19/NO AL) AFM tip with a nominal 8 nm radius. A schematic depiction of the mechanochemical experiment is shown in Figure 3.1 (b), (c) and (d). The cantilever force constant was measured from the geometry of the cantilever measured by scanning

electron microscopy (SEM, Figures 3.2 (a) and (b)), as described in reference [25]. SEM was also used to verify the integrity of the AFM tip prior to performing the experiments (Figures 3.2 (c) and (d)).
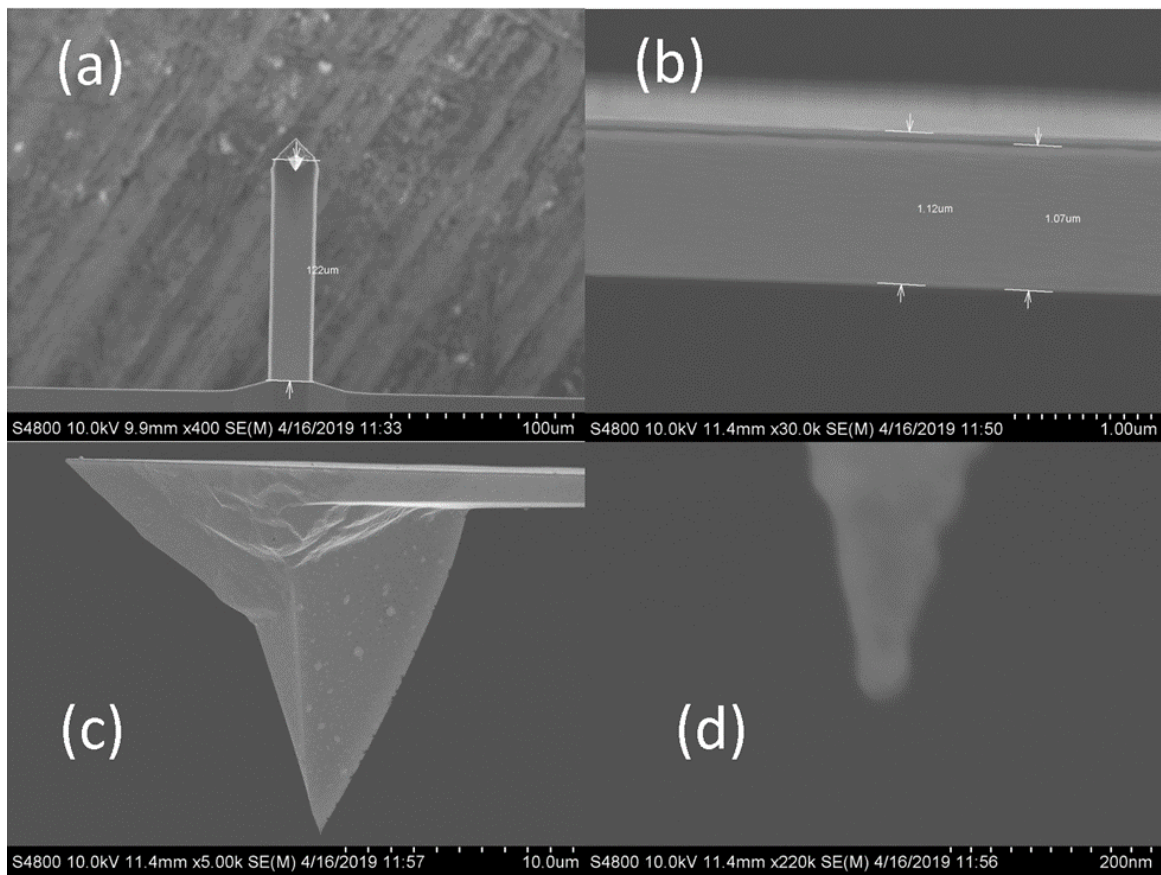
Figure 3.2: Scanning electron microscopy images of the AFM tips. (a) top view of the cantilever, (b) side view of the cantilever, (c) low-magnification view of the silicon tip prior to the experiment, and (d) high-magnification image of the tip prior to experiment. Images were obtained in collaboration with Dr. D.R. Olson.

Since the pressure varies as a function of distance from the center of the contact for the elastic contact of a spherical tip on a planar substrate,[45] the extent of reaction under normal load as a function of time was measured from the depth at the center of the indentation formed on the methyl-thiolate-saturated surface, measured using contact AFM under a non-perturbative load in a scan area of 0.1 μm× 0.1 μm over the pre-indented region. Force-distance curves (Figure 3.3) measured between each indentation experiment verified that the tip shape had not changed. The

tips were found to remain stable over multiple indentation experiments. However, to verify that the nature of the tip did not influence the results, normal-stress-induced reaction rates were measured with two different tips.
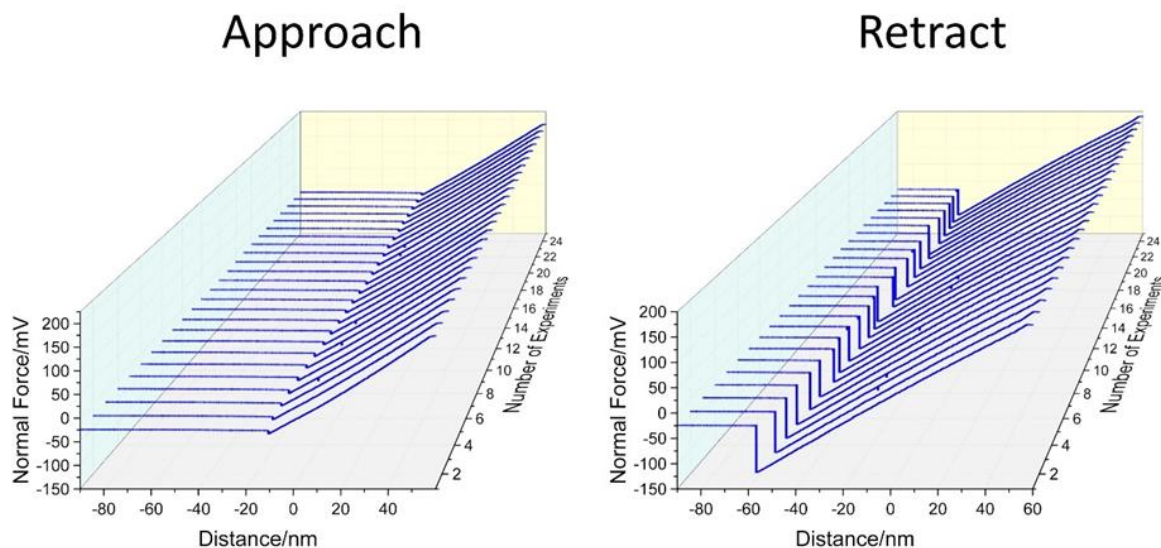
Approach   ## Retract

Figure 3.3: Series of sequential force-distance curves for a saturated methyl thiolate overlayer adsorbed on Cu(100) at 298 K by exposure to DMDS showing the Approach and Retract curves.

3.3 Results and Discussion

Single-asperity compression experiments were carried out on methyl thiolate overlayers formed by dosing DMDS on Cu(100) at room temperature (298 K) in a UHV AFM, with normal loads F_N from 40 to 118 nN, for reaction times up to $\sim 6.3 \times 10^4$ s. The mechanochemical decomposition of a methyl thiolate overlayer creates indentations that are imaged using contact-mode AFM at non-perturbing loads, where it was observed that the maximum depth increases with contact (reaction) time (Fig. 3.4). Because the elastic contact pressure varies with position within the contact,[46] the extent of reaction was measured from the depth at the center of the indentation, where the contact stress is the highest, and the observed shape of the indent is in agreement with this assumption (Fig. 3.5).
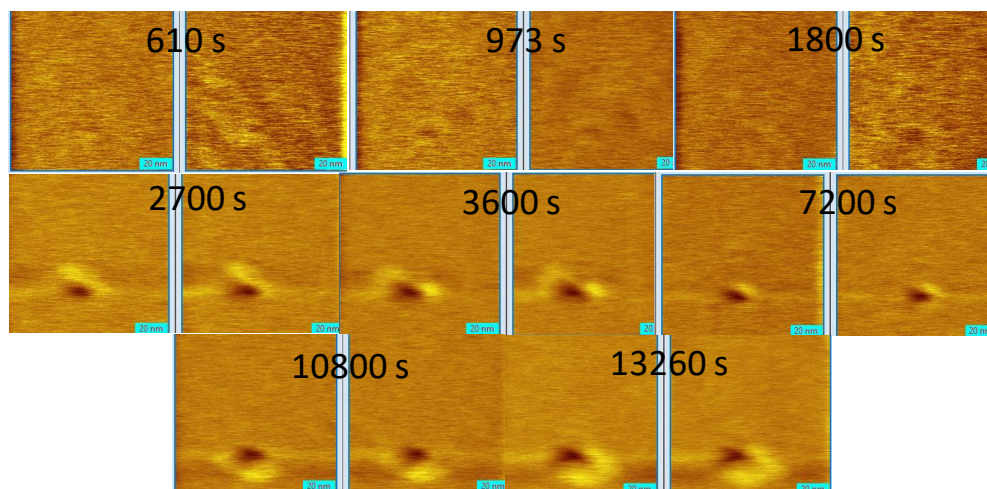
Figure 3.4: Topography images of surface showing the evolution of the surface over time at various contact pressures.

The depth initially increases as a function of time and eventually saturates, indicating the completion of the mechanochemical reaction. The time dependence of the extent of reaction obeys first-order kinetics with respect to methyl thiolate coverage over the whole coverage range (Figs. 3.6).
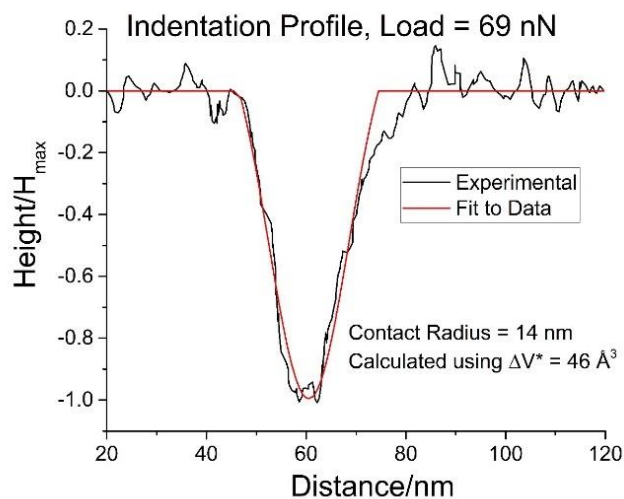
Figure 3.5: Typical indentation profile formed by compressing a methyl-thiolate saturated Cu(100) surface at a load of 69 nN for 9×10^3 s, compared to a fit for an elastic contact using an activation volume of 46 Å^3, by assuming that the indentation depth is proportional to the extent of reaction.

This kinetic order is in agreement with previous measurements of methyl thiolate decomposition rates obtained from the yield of gas-phase products for microscale sliding on copper in UHV.[44,47,48] Fits to the data yield first-order rate constants $k(\sigma_0)$. The contact areas were estimated from the widths of the indentations d after completion of the reactions (Fig. 3.5),[36] and the maximum normal stresses exerted at the center of the contact were calculated from: $\sigma_0 = 6F_N/\pi d^2$.
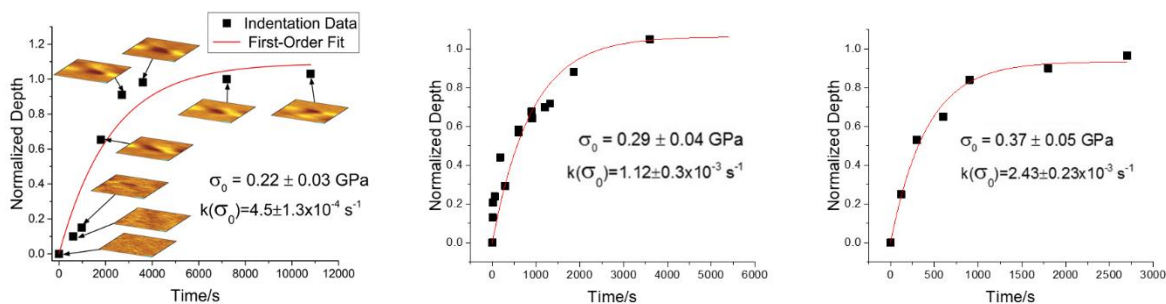
Figure 3.6: Variation in depth as a function of time, and fit assuming first-order reaction kinetics. The contact area, for calculating the maximum contact pressure σ_0, is obtained from the width of indentation.

A linear plot of $\ln(k(\sigma_0))$ versus σ_0 is shown in Fig. 3.7, confirming that the reaction rate does vary exponentially with contact stress,[14,35–39] consistent with the Bell model.[17] Extrapolation to zero stress yields an activation energy of 105.4 ± 0.2 kJ/mol, in agreement with experimental measurements of the activation energy of methyl thiolate decomposition on copper.[16] The slope of the plot in Fig. 3.7 yields an activation volume $\Delta V^{\ddagger} = 46 \pm 1$ Å^3, similar to values previously measured for mechanochemical reactions on surfaces.[14,35–39]
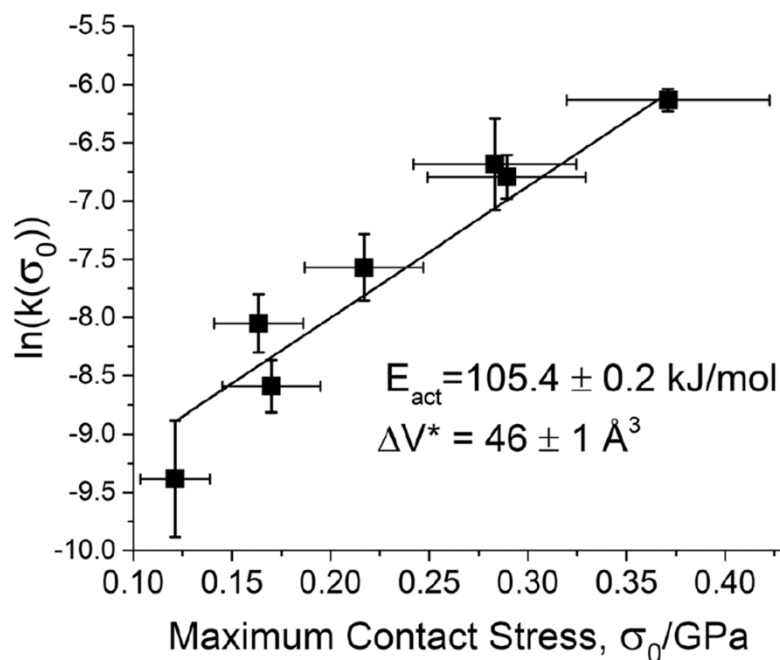
Figure 3.7: Rates of normal-contact-stress induced mechanochemical decomposition of methyl thiolate species on Cu(100), showing a plot of the ***ln* ($k(\sigma_0)$)**, where ***k*** is the rate constant for the mechanochemical decomposition of methyl thiolate overlayer on Cu(100) at 298 K, measured from the maximum depth at the center of the indentation, as a function of the maximum contact stress, σ_0. The linear dependence demonstrates that the mechanochemical decomposition rates obey the Bell model.[17] The intercept yields an activation energy for methyl thiolate decomposition in the absence of a normal stress of 105.4 ± 0.2 kJ/mol when using a pre-exponential factor of 1×10^{14} s^{-1}, in excellent agreement with experimental measurements [47] and theoretical calculations.[46,48]

Dr. Heather Adams and Nicholas Hopper carried out Quasi-static DFT calculations by compressing a clean Cu(100) counterface slab against a methyl-thiolate covered slab, where the energies and configurations were calculated for different values of slab separation.[49] The results reveal an initial slightly attractive interaction as the slabs approach, consistent with the snap into contact as the tip approaches the surface (Fig. 3.3), but the interaction becomes repulsive as the slabs move closer together. The repulsive part of the potential varies parabolically with distance, enabling the normal contact stresses to be calculated. Nudged-elastic band (NEB) calculations of the energy barriers reveal a decrease in activation energy with increasing normal stress (Fig. 3.8 a). Note that the calculated activation energy for zero applied stress is in excellent agreement with the experimental value.[16]

29
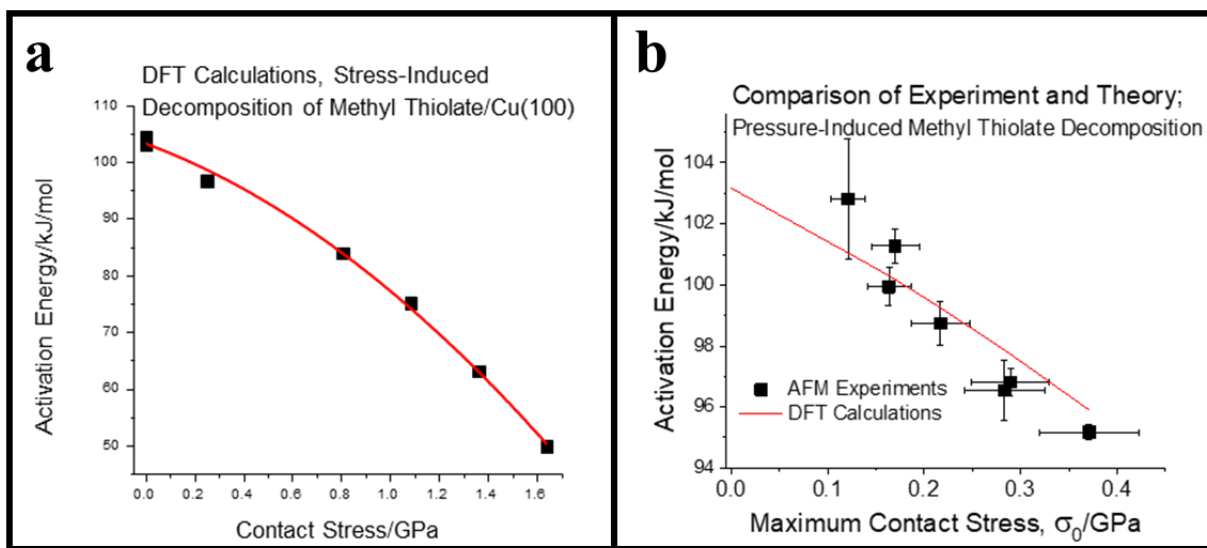
Figure 3.8: (a) Activation energy calculated by DFT as a function of contact stress for the normal-stress-induced mechanochemical decomposition of methyl thiolate species adsorbed on Cu(100).[49] (b) The experimental results are shown plotted directly as reaction activation energy versus maximum contact stress, compared with the DFT results.

The results of the calculations are compared to experiment in Fig. 3.8 (b). Note that the experimentally accessible normal stress range is lower than that used for the quantum calculations, and thus reflects only the initial, almost linear portion of the second-order curve shown in Fig. 3.8 (a).

It is commonly found that the activation energies for elementary reaction steps on metal surfaces scale with the heats of reaction,[50] so that $E_{act} = E_{act}^0 + \alpha E_r$, known as the Evans-Polanyi relation.[51] The stress-dependent activation energy also scales linearly with the heat of reaction (Fig. 3.9), with $\alpha = 0.95 \pm 0.02$, and is similar to values found for bond dissociation reactions on metals.[50]
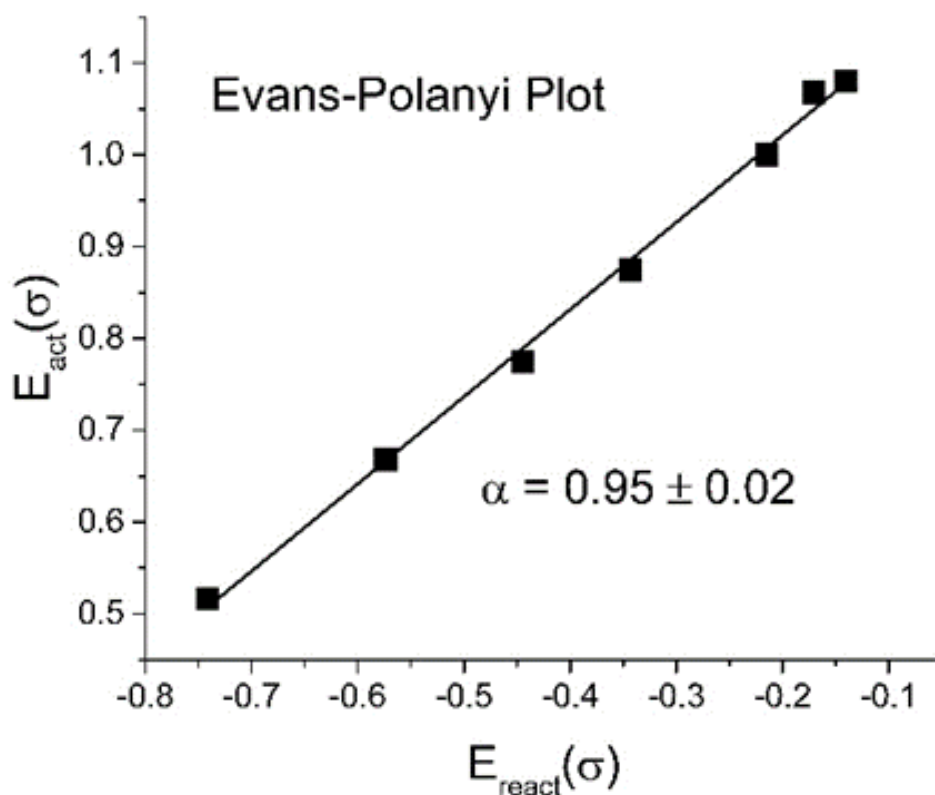
Figure 3.9: Evans-Polanyi plot of the activation energy for methyl thiolate decomposition on Cu(100) as a function of normal stress, that is, $E_{act}(\sigma)$ versus energy of reaction as a function of the normal stress, leading to a slope value α of 0.95 ± 0.02.

3.4 Control Experiments

In order to ensure that the indentation was not due to plastic deformation of the Cu(100) substrate, a sulfur overlayer was formed on Cu(100) to prevent adhesion between the tip and the substrate by heating a methyl thiolate overlayer to 430 K for 300 s. A low-load image showed a flat surface (Figure 3.10 (a)). The center of the scanned region (indicated by a red dot in Figure 3.10 (b)) was then compressed using a load of ~92 nN for 1.2×10^4 s, and showed no indentation when imaged with a load of ~25 nN (Figure 3.10 (c)). This confirms that the indents formed on methyl-thiolate covered copper are due to methyl thiolate decomposition.
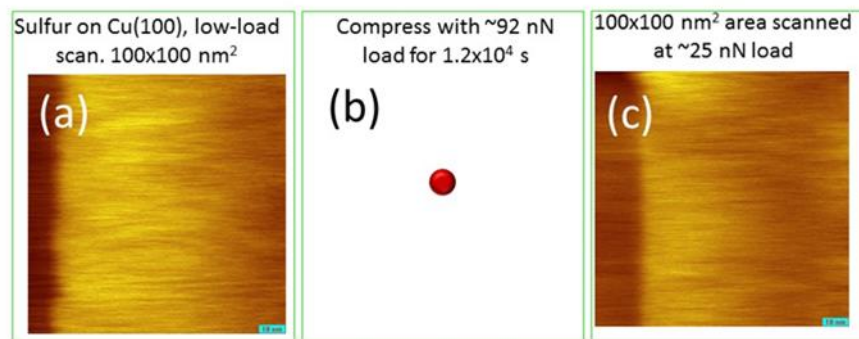
Figure 3.10: 100 nm × 100 nm image of a sulphur-covered Cu(100) surface collected at a low load (a), and then compressed at the center point indicated by a red dot using a load of ~92 nN for 1.2×10^4 s (b). The same region was then imaged at a load of ~25 nN (c) and showed no indentation.

To establish whether the imaged profiles of the indented regions were not perturbed by scanning at low loads, the evolution of the images of the indented surface was monitored by repeatedly collecting images of a methyl-thiolate-covered Cu(100) surface that had been indented at a load of ~52 nN for 9×10^3 s; this removes ~50% of the methyl thiolate layer. Profiles across the indent were analyzed as a function of the number of scans (Figure 3.11) of the AFM tip by fitting the profile to a Gaussian function.
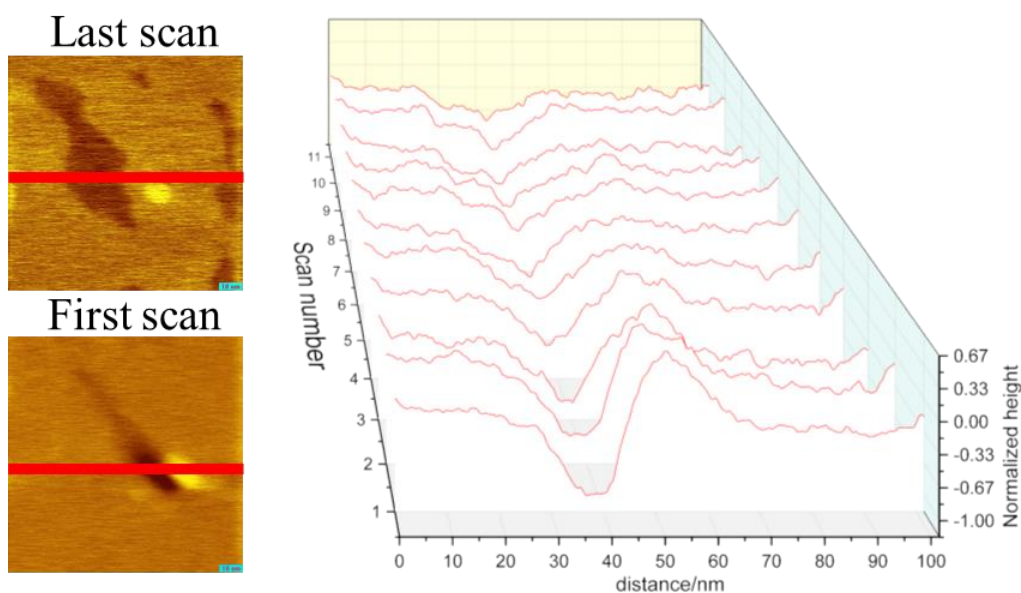
Figure 3.11: Indentation profiles as a function of the number of scans of the AFM tip.

It can be observed that the area under the profile shows no significant variation as a function of the number of scans (Figure 3.12 (a)). However, the width of the indented regions does vary as a function of the number of scans (Figure 3.12 (b)), where a sigmoidal function is shown plotted with the data as a guide to the eye. This reveals that the width of the indented area depends on the number of scans. However, no variation in the width of the indent was found for the first three scans.
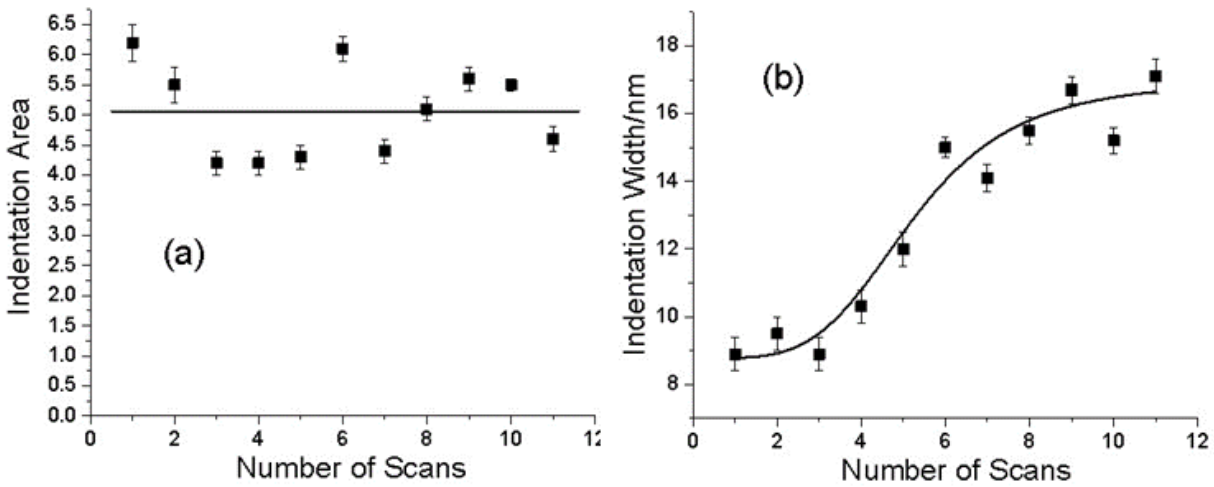
Figure 3.12: Plot of the evolution of a methyl thiolate overlayer on Cu(100) indented at ~52 nN for 9×10^3 s to remove ~50% of the methyl thiolate layer as a function of the number of scans when scanning at low load, displaying (a) the variation in the indented area and (b) the variation in the indented width as a function of the number of scans.

3.5 Indentation Profiles, Reaction Rates and Pressure Distribution

The depth of the indent is proposed to be directly proportional to the extent of the reaction. This assumption is tested by comparing the experimental indentation profile with that calculated using this assumption. The normal stress distribution $\sigma(r)$ for an elastic contact of a sphere against a flat surface is given by $\sigma(r) = \sigma_0 \sqrt{\left(1 - \frac{r^2}{a^2}\right)}$, where σ_0 is the normal contact stress at the center of the contact, and a is contact radius.[45] According to the Bell model, the rate depends exponentially on

33

the stress: $k(\sigma) = k_0 exp\left(\frac{\sigma\Delta V^{\ddagger}}{k_B T}\right)$, where $\Delta V^{\ddagger}$ is the activation volume, which is measured to be

~46 Å³. This will result in mechanochemical reactions occurring more rapidly at the center of the

contact, with the rate decreasing to zero at the edges; the maximum radius of the normal-stress

induced indentation provides a direct measure of the contact radius.[36] Thus, the indentation profile

should reflect both the stress distribution and the rate at which the methyl thiolate decomposes

mechanochemically. If the depth is proportional to the extent of reaction, this yields a depth profile

$d(r)$ given by $d(r) \propto exp\left(\frac{\sigma(r)\Delta V^{\ddagger}}{k_B T}\right)$. To test whether the postulate is valid, experimental depth

profiles were compared to this equation by normalizing the depth to unity and by using $\Delta V^{\ddagger} = 46$

Å³. A typical result is shown in Fig. 3.5, in this case, for an experiment using a load of 69 nN. The

agreement between experiment and theory is in accord with the postulate that the indentation

profiles are mechanochemically induced, and that the indentation depth at the center of the profile

is a measure of the mechanochemical reaction rate. In this case, the normal stress at the center of

the contact is given by $\sigma_0 = \frac{1.5F_N}{\pi a^2}$, where F_N is the normal force exerted by the AFM tip.

3.6 Measurement of Reaction Rates and Activation Energies

Previous experiments to measure the rate of stress-activated decomposition of methyl thiolate

species on copper from the evolution of gas-phase products,[44] show that the reaction is of first

order in methyl thiolate coverage:$-\frac{d\theta_{th}}{dt} = k(\sigma)\theta_{th}$, where θ_{th} is the relative coverage of methyl

thiolate species. Taking the initial relative methyl thiolate coverage to be unity, and integrating the

rate equation gives: $\theta_{th}(t) = (1 - exp(-k(\sigma)t))$, and fits to this equation, carried out using

Origin software, are shown in Figs. 3.6, confirming that methyl thiolate decomposition on Cu(100)

measured by AFM under the influence of a normal stress obeys first-order kinetics over the whole

coverage range. The values of k_0 and $\Delta V^{\ddagger}$ are extracted directly from plots of $\ln(k(\sigma_0))$ versus σ_0 (Fig. 3.7), where the intercept equals $\ln(k_0)$ and the slope is $\Delta V^{\ddagger}/k_B T$, where T is the reaction temperature (298 K). An activation energy is obtained from k_0 by assuming a pre-exponential factor of 1×10^{14} s^{-1}.[47]

3.7 Conclusions

In summary, precise measurements of the mechanochemical reaction kinetics of the normal-stress induced decomposition of a well-defined model system consisting of a methyl thiolate overlayer on a Cu(100) single crystal substrate, reveal that the reaction rate increases exponentially with normal stress, with an activation volume of 46 ± 1 Å^3 and an activation energy in the limit of zero stress that is in good agreement with that for the thermal reaction.

In order to understand the decomposition kinetics of methyl thiolate species on Cu(100), we compared the experimental variation in activation energy as a function of applied stress with modelled quasi-static first principle DFT calculations. The corresponding activation energies results are in excellent agreement with experiment.

Analysis of the quasi-static DFT calculations for this system[49] reveal that the final state is also stabilized by the normal stress, where the stress-dependent activation energy varies linearly with the overall heat of reaction, and thus obeys the Evans-Polanyi relation. Such linear free energy relationships have been very useful in analyzing catalytic reaction pathways [52–55] and are likely to be similarly useful for describing mechanically induced reactions.

Importantly, the ability to predict mechanochemical reaction kinetics using quasi-static DFT calculations will set the stage for studying mechanical activation for stresses that do not necessarily coincide with the lowest-energy pathway, as well as for studying more complex mechanochemical systems. This will aid in further developing robust theories for mechanochemical activation and

for ultimately predicting mechanochemical activity. The next chapter focuses in the study of combined effects of normal and lateral stresses on mechanochemical reaction rates.

Finally, the availability of simple, but precise models for calculating the variation in reaction activation energy with applied stress will allow the velocity and temperature dependences of mechanochemical reaction rates to be predicted using a similar approach to that in the Prandtl-Tomlinson model for frictional energy dissipation.[2,30,33,40]

Chapter 4: Lateral - Stress Anisotropy of Mechanochemical Reaction Rates

4.1 Introduction

The description of mechanochemical reaction kinetics is provided by the Bell model as outlined in Chapter 3. This model is framed within a description of the Born-Oppenheimer potential energy surface (BO-PES), $U(\underline{r})$, which provides the basis for the Bell theory and models the energy of chemical systems as a function of the positions of the atoms, $\underline{r}$, by solving the Schrödinger equation for the electronic energy of the system using fixed nuclear positions, and thus makes the Born-Oppenheimer approximation. Local minima in the potential energy surface correspond to stable configurations of the system, and the energy differences between these metastable states correspond to their reaction enthalpies. Reaction occurs by the system transiting an energy barrier with a height E_{act}, known as the activation energy, defined with respect to the reactant state, to move to the final (product) state. The barrier occurs at a saddle point in the potential energy surface, known as the transition state, and the configuration at this point in the potential energy surface is known as the activated complex. The rate of the reaction is then given by the vibrational frequency of the normal mode on the activated complex that leads to a particular product. The reaction rate constant k is given by:

$$k = \kappa \frac{k_B T}{h} \left(\frac{Z^{\ddagger}}{Z_{react}} \right) exp \left(-\frac{E_{act}}{k_B T} \right) \qquad (4.1)$$

where Z represents the partition function for the reactant and transition states for one mole of material under standard conditions, but where the partition function for the transition state excludes the contribution from the normal mode that leads to product formation.[56] The parameter κ is known as the transmission coefficient, and indicates the probability of each vibration in the normal mode of the transition state leading to product formation. However, values of κ can be calculated for various forms of the potential energy profile using Kramer's rate theory,[57,58] which implicitly assumes that the system is in thermal equilibrium, so that the population of the activated complex relative to the reactant is given by a Boltzmann distribution. Thus, the reaction rate constant depends on the value of E_{act} and the partition functions of the reactant and activated complex.

The central assumption that underpins mechanochemical rate theories is that the potential due to the imposed mechanical force modifies the PES to change the energies and positions of the reactant and transition states, modifying the energy barriers and thereby altering the rate of reaction. When the rate is increased relative to the rest state, this results in the occurrence of mechanochemical reactions. If the applied force is F, then the PES is modified to give,

$$U(\underline{r}, \underline{F}) = U(\underline{r}) - \int \underline{F} \cdot d\underline{r} \qquad (4.2)$$

In the simplest analysis of the model, the force F is assumed to be constant and act along the x direction, so that $\int \underline{F} \cdot d\underline{r} = Fx$. This leads to a first-order equation for the force-dependent activation as $E_{act}(F) = E_{act} - F\Delta x^{\ddagger}$, where $\Delta x^{\ddagger}$ corresponds to the distance from the initial to the transition state. This corresponds to the Bell model, and the results of Chapter 3 indicate that the equation should be modified to include second-order effects of the force in the positions of the

initial and transition states that lead to a F^2 dependence, known as the extended-Bell model, which was verified in Chapter 3.[59] This analysis assumes that the applied force is aligned with a component of the reaction coordinate, and the experimental conditions selected in the work described in Chapter 3 ensured that this was the case. However, this condition will not always be fulfilled for lateral forces acting on adsorbed methyl thiolate species on copper, where evidently the force will generally not be aligned along the reaction coordinate. In order to analyze this model, several researchers have analyzed the force-dependent trajectories as a function of the direction of the force.[60–63] In order to explore this issue for the lateral-force dependent rate of methyl thiolate decomposition on Cu(100), we used a model two-dimensional PES with a fixed energy barrier but with a strongly varying energy landscape. These results are then used to analyze experimental data for the decomposition of methyl thiolate species on copper caused by lateral sliding measured in a UHV atomic force microscope.

4.2 Influence of Lateral Force in Mechanochemical Reaction Rates

To understand the influence of lateral force on the mechanochemical reaction rate, theoretical calculations have been carried out. This work has been done in the context of a collaboration with Dr. Germaine Djuidje Kenmoe and consists of a specific adaptation of the model described in ref. [41]. In order to model methyl thiolate decomposition, a two-dimensional potential was used. This is a modified Remoissenet-Peyrard (R-P) potential [64] that has suitable properties and is given by,

$$V(x.y) = \frac{E_{act}(1 + r^2)(1 - \cos(\pi x/a)\cos(\pi y/a))}{(1 + r^2 + 2r\cos(\pi x/a)\cos(\pi y/a))} \qquad (4.3)$$

where a is the periodicity of the lattice and r is a parameter such that $|r| < 1$ that influences the shape of the potential. When $r = 1$, this yields a two-dimensional sine function.

The function has a periodic global minimum at $x = y = 0$, so that $\cos(\pi x/a) = \cos(\pi y/a) = 1$, which, when substituted into Eqn. 4.3, gives,

$$V(0,0) = E_{min} = 0 \tag{4.4}$$

A saddle point occurs at $\frac{x}{a} = \frac{y}{a} = \frac{1}{2}$. This yields: $\cos(\pi x/a) = \cos(\pi y/a) = 0$, and substituting into Eqn. 3 gives,

$$v(1,1) = E_{saddle} = E_{act} \tag{4.5}$$

so that Eqn. 4.3 is adjusted so that E_{act} corresponds to an activation energy. Note, however, that this model function is an approximation because the transition state will not necessarily occur at $\frac{x}{a} = \frac{y}{a} = \frac{1}{2}$. Thus, the reaction coordinate as the system evolves from the reactant to the product follows $x = y$, and $\Delta x^{\ddagger} = \frac{a}{\sqrt{2}}$. A representation of the PES is shown in Figure 4.1.
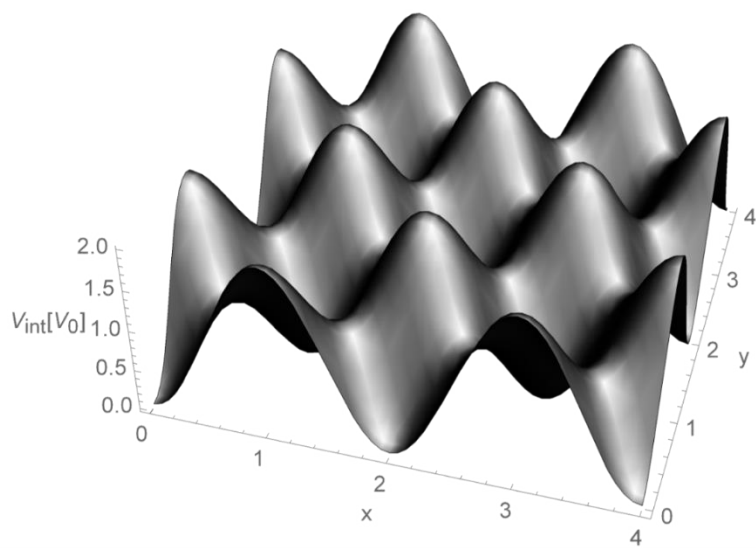
Figure 4.1: Modified R-P potential for the potential energy surface utilized.

The maximum in the potential occurs at $\frac{x}{a} = 0, \frac{y}{a} = 1$, and gives $\cos(\pi x / a) = 1, \cos(\pi y / a) = -1$

and yields,

$$E_{max} = 2E_{act} \frac{1 + r^2}{(1 - r)^2} \tag{4.6}$$

so that the relative height of the potential on either side of the saddle point depends on the value

of r. Thus, as $r \to 1$, the height of the barrier increases. However, the effect of r in the energy

barrier depends on the direction we travel through the potential energy surface, being the change

maximum when we travel across a maximum $(x + y = 1)$, and neglegible through the saddle point

$(x = y)$, as shown in Figure 4.2. It can be anticipated that, as the height of the potential maximum

increases, the reaction will be funneled through the lowest-energy pathway and will follow a

sinusoidal dependence.

The value of r for any particular value of E_{max}/E_{act} can be calculated from:

41

$$r = \frac{\left(\frac{E_{max}}{E_{act}}\right) - 2\sqrt{1 + \left(\frac{E_{max}}{E_{act}}\right)}}{\left(\frac{E_{max}}{E_{act}}\right) - 2} \tag{4.7}$$
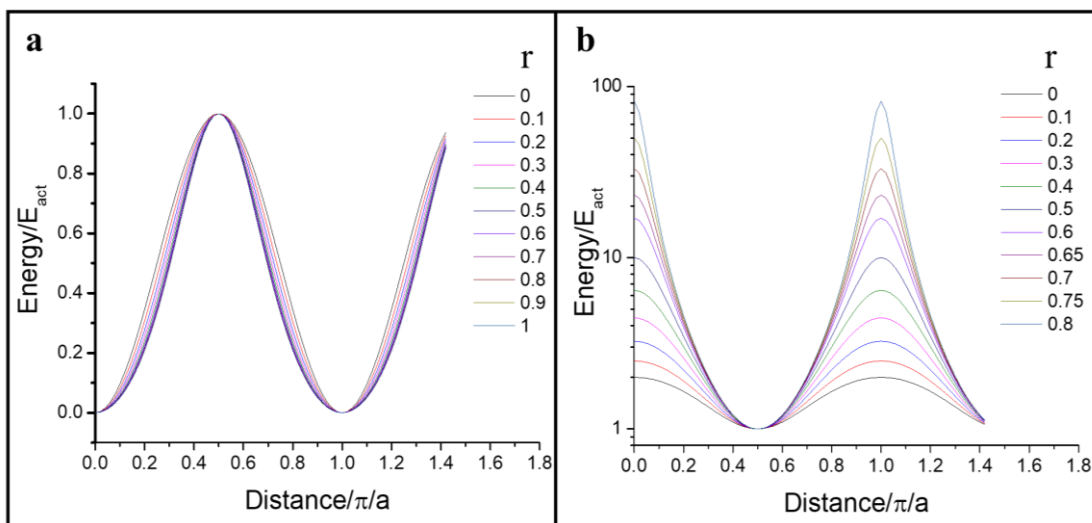
Figure 4.2: (a) Energy profiles along x=y (lowest-energy pathway), and (b) along x+y=1 (across a maximum), though the transition state, as a function of +r.

Considering the potential energy surface (PES) $U(\underline{r})$ from equation 4.3, as a function of the vector $\underline{r}$, where reaction products/intermediates correspond to local minima of the PES, when a force $\underline{F}$ is applied, the locations of those minima are shifted to new mechanical equilibria according to Newton's law, requiring the total force to be zero or $\underline{\nabla}U = \underline{F}$. The solution of this equation is also a minimum of the force-modified potential, $U(\underline{F}, \underline{r}) = V(\underline{r}) + \underline{F} \cdot \underline{r}$. The dependence of a reaction rate k on the applied force F is given by,

$$d\ln k/dF \approx \frac{\Delta x^{\ddagger}}{k_B T} \equiv \frac{x_{TS} - x_R}{k_B T} \tag{4.8}$$

42

When the force F is close to its critical value F_c, when the activation barrier E_{act} vanishes, the transition rate can be approximated by,

$$k(F) = k(0)exp\left[\frac{\Delta V^{\ddagger}(0)}{k_B T}\left(\frac{F_c - F}{F_c}\right)^{3/2}\right]$$ (4.9)

where $\Delta V^{\ddagger}(0)$ is the activation barrier at zero force.[41]

The activation length $\Delta x^{\ddagger}$ vanishes as the system approaches the critical force F_c (catastrophic point) as,

$$\Delta x^{\ddagger}(F) = \Delta x^{\ddagger}(0)\left(\frac{F_c - F}{F_c}\right)^{1/2}$$ (4.10)

where $\Delta x^{\ddagger}(0) = \frac{3\Delta V^{\ddagger}(0)}{2F_c}$.

From this, one can calculate the evolution of the PES as a function of the applied directional force, as shown in Figure 4.3.
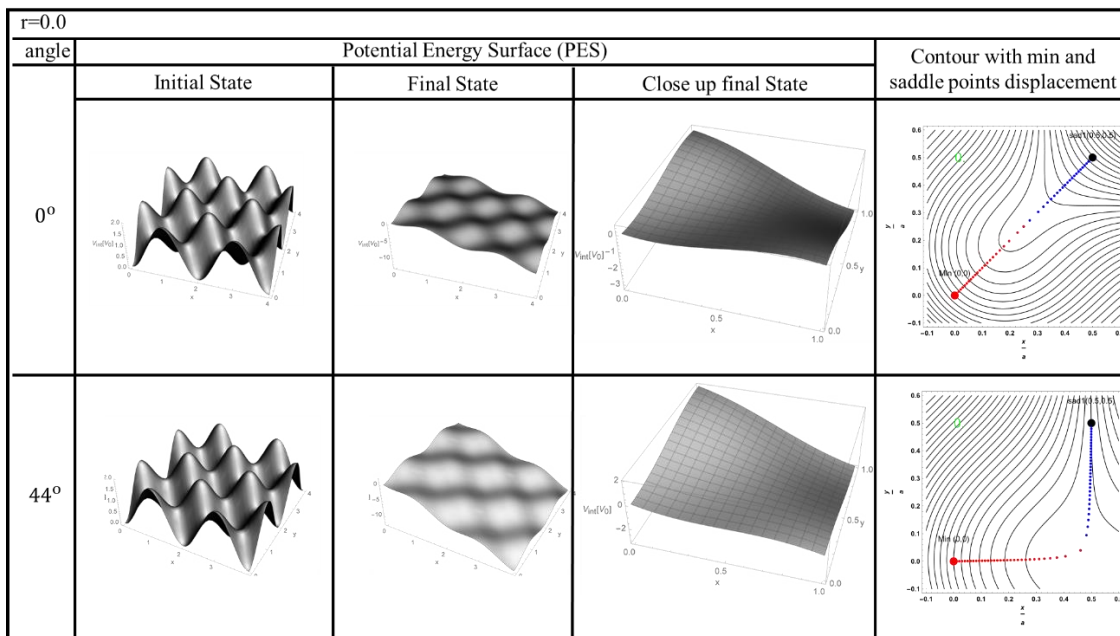
Figure 4.3: Example of results from theoretical calculations showing the PES in absence of force (initial state), at the force in which minimum and saddle points meet (final state), and tracking of displacement of minimum (red dots) and saddle points (blue dots) as a function of applied force from the initial to the final state on top of final state contour plot.
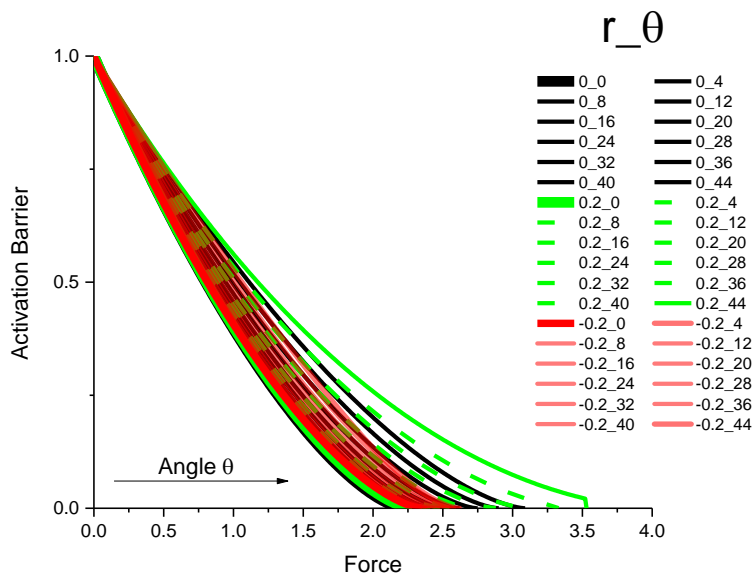
Figure 4.4: Theoretical results of activation barrier as a function of force until the energy barrier vanishes for different values of *r* and azimuthal angle of the applied force.
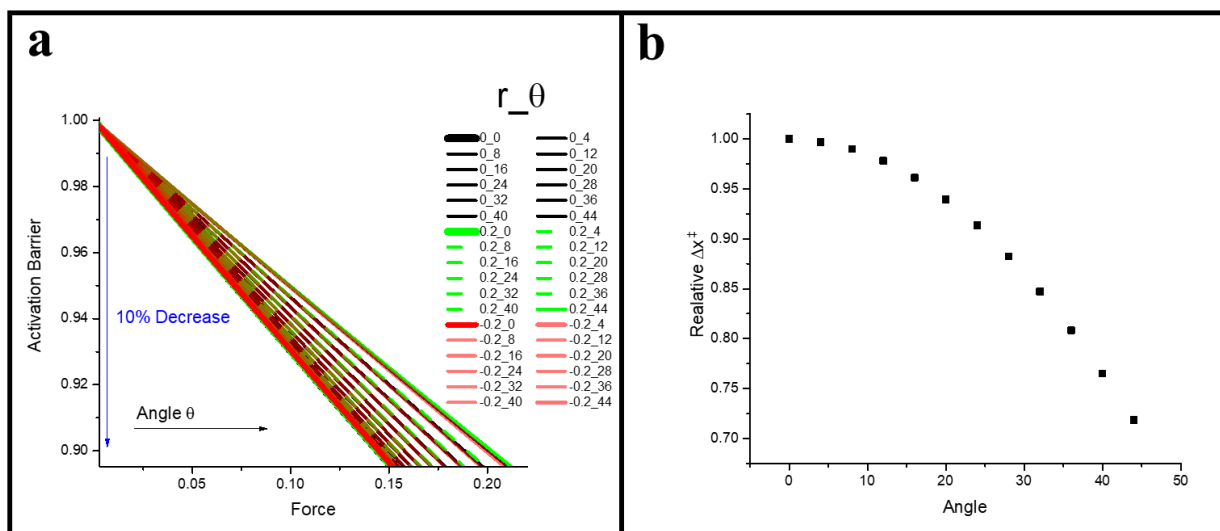
Figure 4.5: (a) Close up view of theoretical results of activation barrier as a function of force until the energy barrier is reduced to ~10% of its initial value, for different values of r and azimuthal angle of the applied force. (b) Relative change in activation length as a function of azimuthal angle of the applied force.

The results are summarized in Fig. 4.4-5, which shows the variation in energy barrier as a function of azimuthal angle for the model R-P potential for various values of r. As can be seen, the angular dependence does not depend on the values of r, but only on the initial- and transition-state energies, and is independent of the path taken between them. This is not surprising and is just an expression of the first-law of thermodynamics, and was used to analyze the influence of external potentials, including hydrostatic pressure, on the rates of chemical reactions by Evans and Polanyi.[51] This enables a general equation for the stress-dependent energy barrier to be derived by expanding the force about the initial and transition states, independent of the reaction pathway between them. This is illustrated in the next section.

4.2.1 Mechano-tribochemical Reaction Rates in Three Dimensions

The goal is to solve Eqn. 4.2 by expanding the PES around the initial and transition states. Because they are both turning points for which $\underline{\nabla}.U(\underline{r})$=0, the linear term in the expansion is zero, and the first non-zero terms is quadratic; this is an expression of Hooke's law. Therefore, the expansion of the PES has terms due to (i) the force-dependent changes in the positions of the initial and transitions states and (ii) the work required to convert the initial-state structure into the activated complex. Both the linear and quadratic terms have been identified in Chapter 3. In addition, as emphasized in that work, the reaction rate is not measured from the force acting directly on the reactant (the mechanophore), but from the applied stress (the force per unit area). This can, of course, be converted into the force acting on the mechanophore if the number of molecules per unit area is known. This can be described by the stress tensor, $\sigma_{ij} = \begin{pmatrix} \sigma_{11} & \sigma_{12} & \sigma_{12} \\ \sigma_{21} & \sigma_{22} & \sigma_{13} \\ \sigma_{31} & \sigma_{32} & \sigma_{33} \end{pmatrix}$. In this case, the diagonal terms indicate normal stresses in the x, y and z directions, and the off-diagonal terms denote shear stresses, so that the stress tensor can also be written as: $\begin{pmatrix} \sigma_x & \tau_{xy} & \tau_{xz} \\ \tau_{yx} & \sigma_y & \tau_{yz} \\ \tau_{zx} & \tau_{zy} & \sigma_z \end{pmatrix}$, which includes symmetry by taking account of the equivalence of x, y and z. This leads to an equation for the change in energy barrier in three dimensions as a function of the stress tensor σ_{ij} as,

$$E_{act}(\sigma) = E_{act} - \left(V_{ij}^t - V_{ij}^i\right)\sigma_{ij} - \frac{1}{2}\left(\Omega_{ijkl}^t - \Omega_{ijkl}^i\right)\sigma_{ij}\sigma_{kj} \qquad (4.11)$$

where $V_{ij}^{t,i} = \frac{\partial U^{t,i}}{\partial \sigma_{ij}}$ and $\Omega_{ijkl}^{t,i} = \frac{\partial^2 U^{t,i}}{\partial \sigma_{ij}\partial \sigma_{kl}}$. The term $V_{ij}^t - V_{ij}^i$ represents the change in volume of the system between the transition and initial states of the reaction and is known as the activation

46

volume, $\Delta V^{\ddagger}$, and the term $\Omega^t_{ijkl} - \Omega^i_{ijkl}$ represents the change in curvature between the initial and

transition states and gives rise to the second-order term in the extended-Bell model.

Clearly, the direction of the applied stress can influence the reactivity. For example, if a force

applied in a particular direction lowers the energy barrier and accelerates the rate of a reaction, a

force directed in the opposite direction will *increase* the barrier and inhibit the reaction. One can

also imagine that an appropriately applied force could change the selectivity of a reaction by

specifically lowering a barrier that is slightly higher than the barrier for the lowest-energy pathway.

The mechanochemical reaction rate could also be influenced by the way in which the force is

applied, for example, for a mechanophore anchored to a surface compared to in a liquid. These

differences are highlighted by widely varying the values of the activation volume measured in a

fluid [14] and on a surface.[35] These issues are discussed in greater detail in the next section.

4.2.2 Coupling of Forces to the Mechanophore in Mechano-tribochemical Reactions

As noted above, the way in which forces are applied to molecules in a fluid and on a surface will

be different. In the pressure-induced reactions discussed above, these are induced by the

hydrostatic pressure $P = \frac{1}{3}(\sigma_x + \sigma_y + \sigma_z)$ and will presumably accelerate reactions that are

initiated by compression of the whole molecule. Cases in which forces are exerted by fluid shear

are more complicated because the stress distribution depends on the geometry and, for example,

the stress is uniform during Couette flow.

We will examine this issue for a mechanophore adsorbed on a surface with applied normal (σ_z) or

shear (τ_{xy}) stresses. The effect of the applied force is to modify the potential energy surface by an

additional term $\int \underline{F} \cdot d\underline{r}$. That is, the external force will act to displace the atoms in the

mechanophore, thereby influencing the energy barrier between the initial and transition state to

modify the reaction rate. The displacement of atoms from their equilibrium positions are well

47

described within a Harmonic approximation, where the Hessian (force-constant matrix) can be diagonalized for the $3N$ vibrations of an N-atom system to form $3N$ normal modes, three of which correspond to molecular translations in the $x, y \; and \; z$ directions and rotations about these axes, and $3N - 6$ internal normal modes. The symmetry of these normal modes (their irreducible representations) depend on the geometry of the molecule and can be obtained using group theory. For a particular symmetry-adapted linear combination of atomic displacements to result in a modification of the potential energy surface, the integral $\int \underline{F} \cdot d\underline{r}$ must be non-zero, and thus belong to the totally symmetric irreducible representation. Although it has been proposed that molecular symmetry is conserved during the trajectory from the initial to the transition state,[65] this has been found not to be true in all cases.[66] However, the structure of the initial state, as it evolves on its journey to the transition state, must interact with the applied stress such that, for the integral above to be none-zero, the symmetry adapted vibrational modes and the applied stress must have the same symmetry. Note that the symmetry rule says nothing about the extent to which the particular vibrational state influences the reaction rate. This idea is illustrated for a diatomic mechanophore adsorbed with its principle axis perpendicular to the surface (along the z direction) on a four-fold site, intended to mimic the adsorption on the four-fold hollow site of the (100) face of a face-centered cubic metal (copper). The terminal "atom" of the mechanophore could be an unreactive species such as a methyl group. This structure models a methyl thiolate mechanophore adsorbed on a Cu(100) surface. It has been previously shown that this undergoes decomposition under shear.[44,47,67]

This structure has C_{4v} symmetry and the irreducible representations for orthogonal displacements of the atoms, $\Gamma = 2A_1 + 2E$, and thus has two singly degenerate and two doubly degenerate symmetry adapted displacements. The lateral translations (T_x, T_y) correspond to diffusion of the

48

molecule along the surface in the x or y directions and has E symmetry, while T_z, with A_1 symmetry, corresponds to desorption of the molecule or compressions against the surface. The frustrated rotations (R_x, R) correspond to tilts in the x or y directions and also has E symmetry. The remaining A_1 displacement corresponds to the bond extension. These results and the stresses that induced these reactions are summarized in Table 1.

Motion	Irreducible Representation	Inducing Stress
Molecular Tilt, (R_x, R_y)	E	σ_{xz}, σ_{yz}
Molecular Diffusion (T_x, T_y)	E	σ_{xz}, σ_{yz}
Desorption/Bond Extension	A_1	$\sigma_x + \sigma_y, \sigma_z$
Bond Compression/Dissociation	A_1	$\sigma_x + \sigma_y, \sigma_z$

Table 1: Symmetry properties of the stress induced decomposition of a pseudo diatomic species adsorbed on a four-fold hollow surface site.

The last column in the Table shows the stresses (taken from the Character Table) that induce the reactions. The work on Chapter 3 that examined the effect of a normal stress (σ_z), shows that reactions initiated by normal modes with A_1 symmetry will be affected. This motion will involve desorption of the molecule or bond extension if σ_z is tensile, or bond compression if the applied force in compressive.

Shear stresses along the x or y directions can lead to either molecular tilt, which couple with the transitions state for dissociation, or translation, that will result in molecular diffusion across the surface and thus lead to no mechanochemical reaction. Note that this lateral motion will also include compression, so that the overall tribochemical reaction rate will be due to both normal and lateral (shear) stresses the effects. The results of these measurements are described below.

4.3 Experimental Methods

The instrumental setup, sample preparation and dosing conditions utilized in this section are as used and described in Chapter 3. Lateral force experiments, in which not only normal stress is exerted but also sliding of the tip on the Cu(100) surface, are described here. A convenient flat area of ~200 nm × 200 nm was chosen by searching within steps of the surface by scanning with non-perturbing forces. An image of this initial state of the surface is shown in Figure 4.6 (a). Then, a small line of 30 nm in length is rubbed under a well-defined load for 256 cycles of trace and retrace sliding of the tip at a speed of 90 nm/s; schematics of this step is depicted in Figure 4.6 (b). Finally, a 90 nm × 90 nm area is imaged at non-perturbing loads to observe the effects of the sliding cycles; a representation and topography image of two equivalent line experiments is shown in Figure 4.6 (c).
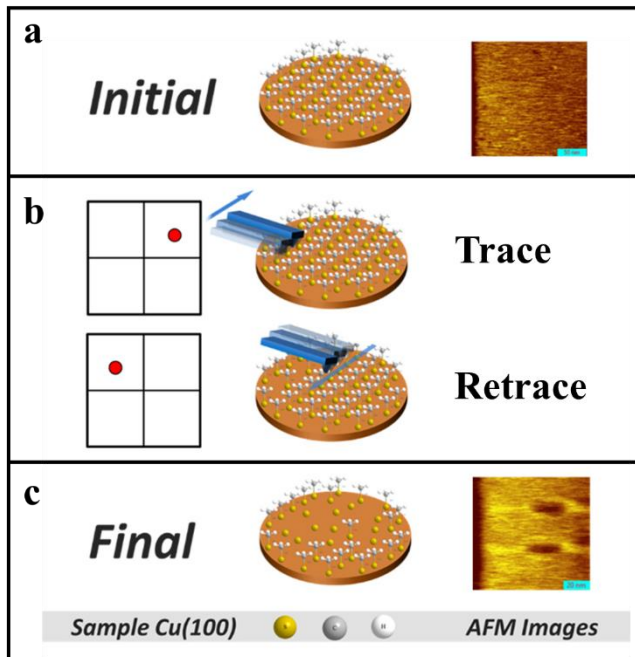
Figure 4.6: Schematic representation of (a) sliding experiment and topography images showing an initial experimental area, (b) schematics of the sliding of the tip on the surface and the reading of the detector for the trace and retrace direction and (c) final two rubbed equivalent lines of 30 nm in length each.

Next, the angle of the sliding direction is varied while all other conditions were kept constant. Note that the lateral force could not be measured in this experiment because the tilt of the AFM cantilever could not be measured at all angles. Here, the variation in depth of the groove, as described in Chapter 3, is considered to be a measure of extent of reaction for the mechanochemically induced process. In this particular section, the anisotropy of lateral-force-induced mechanochemistry is studied as a function of angle for reaction of the methyl thiolate mechanophore on Cu(100). The experimental angles were measured relative to the [110] directions of the copper single crystal surface, where the lattice direction was calibrated by using the low-energy electron diffraction (LEED) pattern of the clean Cu(100) surface. The crystal directions were obtained by orienting the sample using the normal axis, shown as y in Figure 4.7(a), using the LEED pattern, then the scanning direction x is transformed to the crystal direction from Figure 4.7(b), and the experimental angles corrected by defining $0°$ to be along the [110] crystal direction as illustrated on Figure 4.7(c).
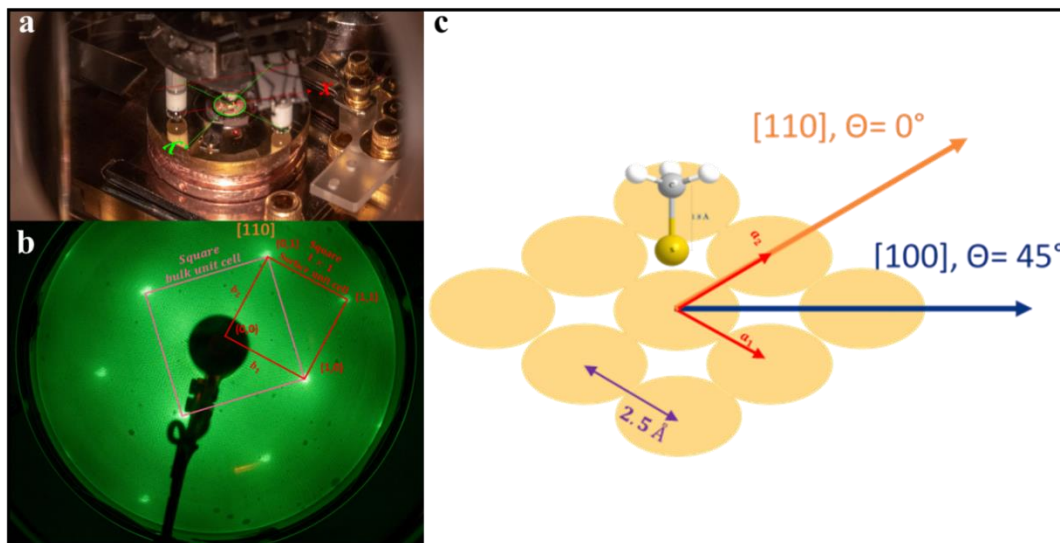
Figure 4.7: (a) Photograph of the sample with the tip after approach used for calibrating the relative angles with respect to the [110] crystal direction obtained from in-situ LEED diffraction pattern shown in (b), and (c) schematic diagram of the Cu(100) surface, where the crystal directions and the lattice constant are depicted, and the methyl thiolate molecule is adsorbed at a four-fold site.

4.4 Results and Discussion

4.4.1 Angular Dependence of Lateral Force on Mechanochemical Process

An entire set of topography images is shown in Figure 4.8, from which the maximum depth is extracted as a function of angle for each of the 30-nm-long linear sliding experiments.
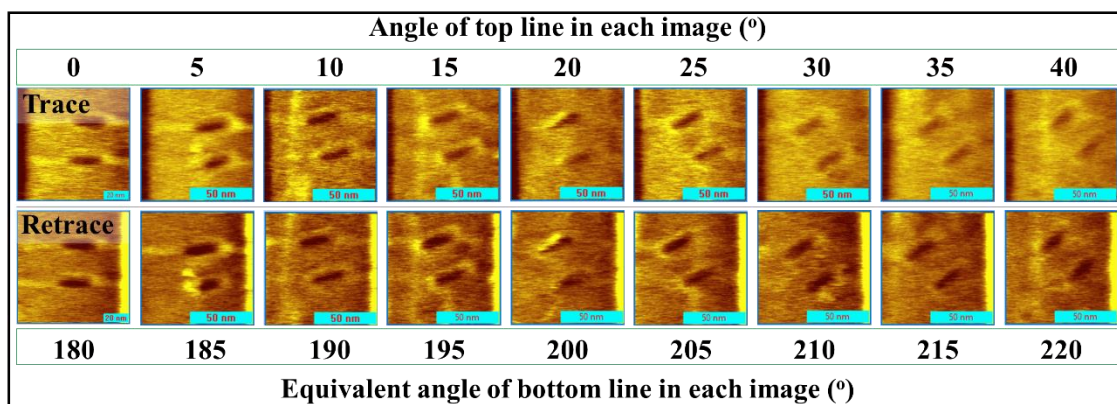
Figure 4.8: Experimental topography images of a 30 nm line sliding as a function of angle experiment under 20 nN normal load, at a scan speed of 90 nm/s for 256 scans back and forth.

The normalized maximum depth of the indentation as a function of angle for a sliding experiment with a normal force of 40 nN is shown in Figure 4.9. It is observed that, under this applied normal load, the groove reaches its maximum depth for all sliding angles, indicating that the reaction is complete. This is confirmed by carrying out these experiments at higher normal stresses and finding no further increase in depth. This maximum depth is equal to that found for normal-stress experiments (see Chapter 3) when the reaction was complete. A repeat set of data collected under identical conditions, but for a different range of angles, is shown in Figure 4.10 with identical results, suggesting that the experiments are reproducible.
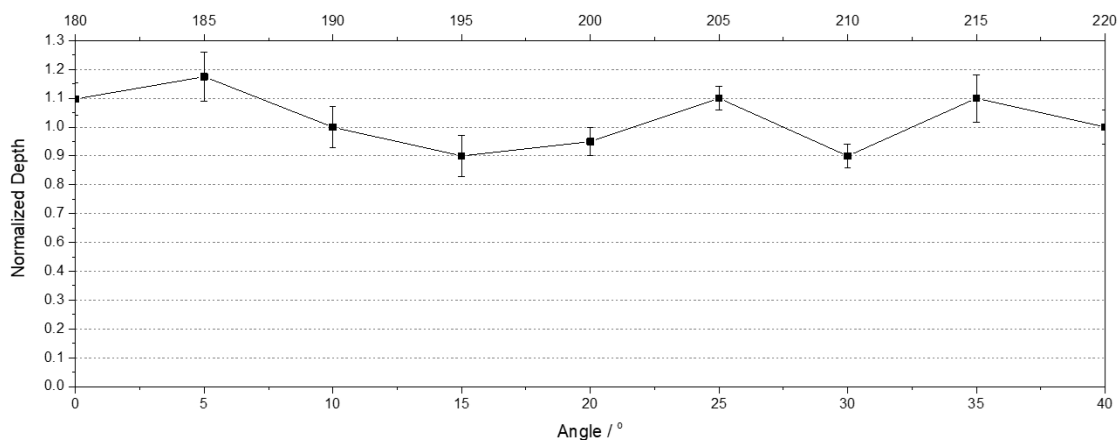
Figure 4.9: Line normalized depth as a function of angle in a range from 0° to 40º and 180° to 220º in steps of 5º. Data were collected after 256 sliding cycles under 40 nN normal load over lines of 30 nm in length at a sliding speed of 90 nm/s.
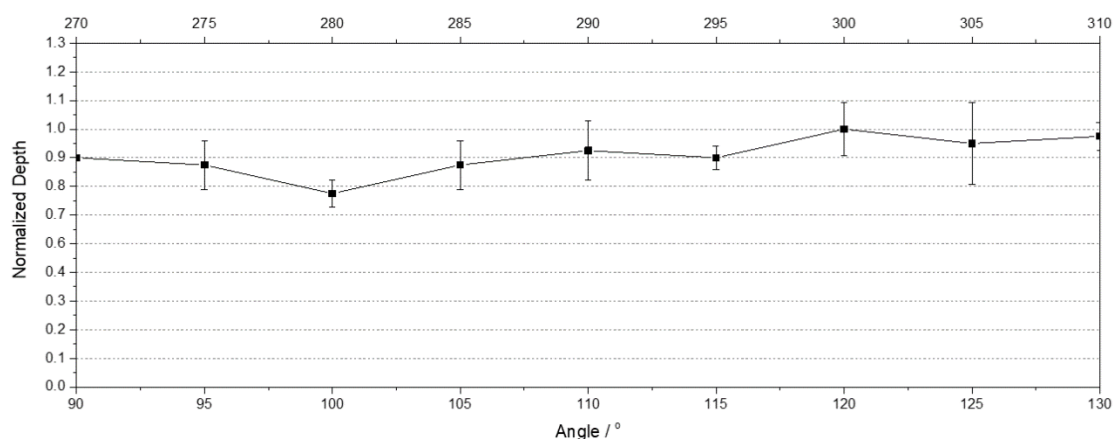
Figure 4.10: Line normalized depth as a function of angle in a range from 90° to 130º and 270° to 310º in steps of 5º. Data were collected after 256 sliding cycles under 40 nN normal load over lines of 30 nm in length at a sliding speed of 90 nm/s.

The load was decreased to 20 nN, and these lower loads yielded the results observed in Figure 4.11, where the reaction did not proceed to completion and some anisotropy was observed, giving a maximum value of the extent of reaction along an angle coincident with the [110] direction of the Cu(100) single crystal surface. Note that this is the direction of the lowest-energy decomposition pathway for methyl thiolate species on copper.
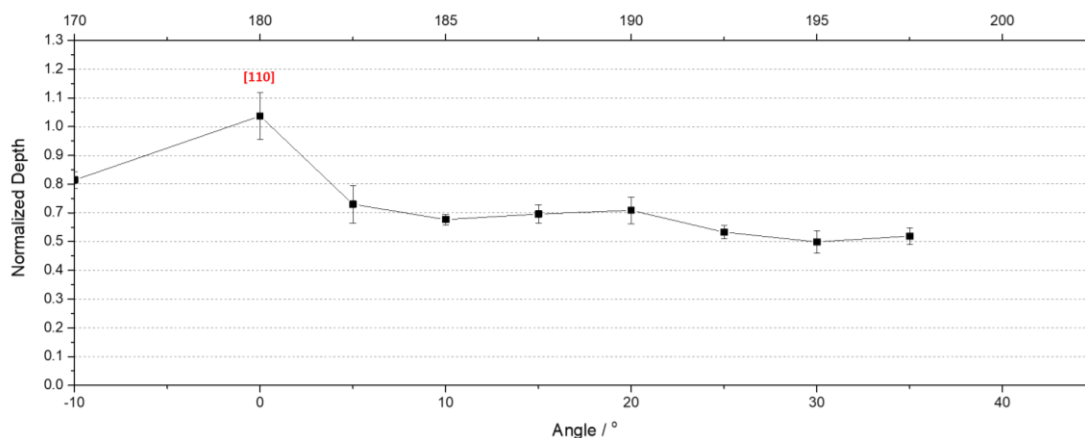
Figure 4.11: Normalized depth as a function of angle in a range of 45° for equivalent (-10°) - 35° and 170° - 215° angular ranges (the angles are normalized to 0° being aligned with [110] surface direction). Data were collected after 256 sliding cycles under a load of 20 nN with a scan amplitude of 30 nm, at a sliding speed of 90 nm/s.

In order to investigate whether the reaction data are compatible with the methyl thiolate decomposing on the copper surface, we extend the simple model for reaction by compression (Chapter 3) to one which includes the effect of lateral sliding. We assume that the contact area for the sliding experiment is identical to that measured for just the normal load, where the contact area and pressures can be measured from the size of the indent. This allows the maximum contact pressure to be calculated as 0.12 ± 0.02 GPa for the normal load of 40 nN, and 0.065 ± 0.008 GPa for a load of 20 nN. Note that these contact stresses are much lower than those needed to initiate methyl thiolate decomposition under normal stress alone. In that case, the extent of reaction was gauged from the loss of methyl thiolate species at the center of the contact, and the reaction time was simply the time that tip was in contact with the surface. In the case of sliding, reaction is initiated as the tip starts to slide over a molecule on the surface. The contact pressure then increases to a maximum value (given above) in the center of the contact, and then decreases once again as the tip contact moves to the edge of the contact region. In this case, ideally, the reaction rate should be integrated over this stress distribution. However, because the model is relatively simple and

54

does not include the effects of coupling the normal and lateral stresses, we will calculate the rate

by simply using the average contact pressure, which for the 40 nN load is 0.08 ± 0.01 GPa and for

the 20 nN load is 0.043 ± 0.005 GPa.

The total dwell (reaction) time at this load t_d is given by $t_d = \frac{2N_S w}{v}$, where N_S is the number of

scans and the factor 2 takes account of the fact that the tip moves in both directions, w is the width

of the contact and v is the sliding velocity (90 nm/s). Previous work has shown that the width of

the contact is 24.6 nm, and gives a time per pass of 0.273 s for a total dwell time of 140 s. As noted

above, we assume that the lateral and normal forces act independently, and to first order (that is,

within the approximation of the Bell model), the activation energy is given by,

$$E_{act}(\sigma_N, \sigma_L) = E_{act}^0 - \Delta V_N^{\ddagger}\sigma_N - \Delta V_L^{\ddagger}(\theta)\sigma_L \qquad (4.12)$$

where σ_N and σ_L are the normal and lateral stresses, and $\Delta V_N^{\ddagger}$ and $\Delta V_L^{\ddagger}$ are the activation volumes

for normal and lateral sliding, where the angular dependence of the lateral activation volume has

been explicitly included. It will be assumed that the activation volume for normal stress is identical

to that measured previously (Chapter 3, 46.4 Å^3), and that it does not depend on the scanning

direction.

Because it is not possible to measure the lateral force, only the applied normal force, for different

scan angles, it is assumed that the lateral force is identical for all scan angles and dictated by the

friction coefficient μ, so that the equation for the activation energy becomes,

$$E_{act}(\sigma_N) = E_{act}^0 - (\Delta V_N^{\ddagger} - \mu\Delta V_L^{\ddagger}(\theta))\sigma_N \qquad (4.13)$$
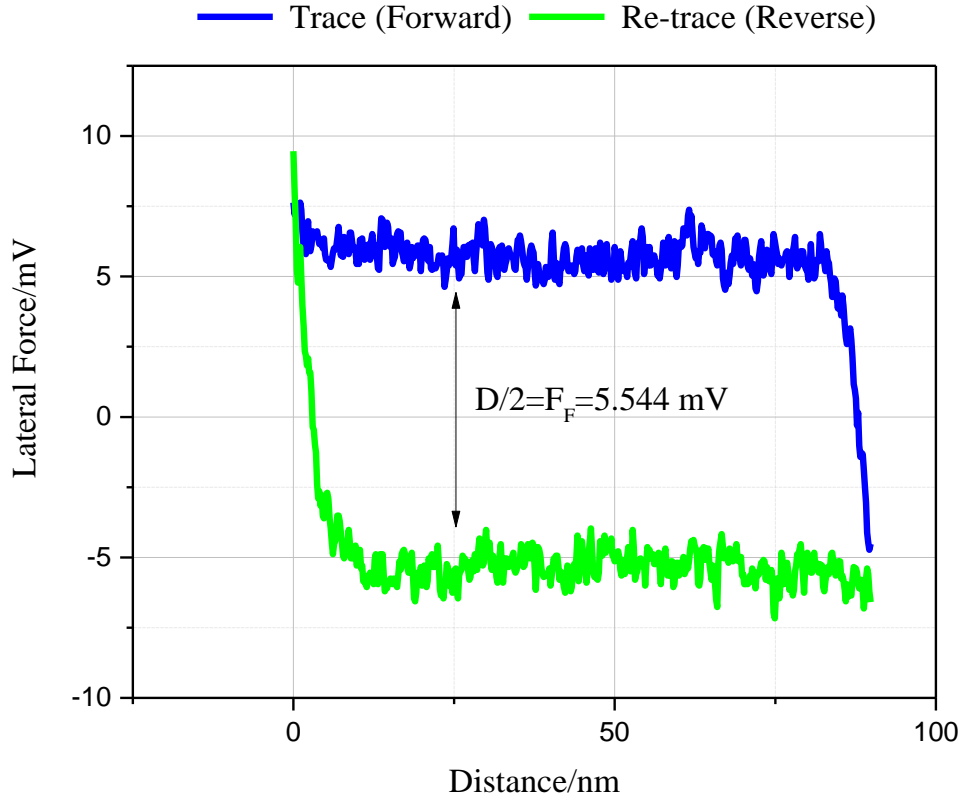
Figure 4.12: A friction loop for forward and reverse sliding under a load of 20 nN.

The friction coefficient is obtained from the friction loop as illustrated in Figure 4.12, where the lateral force is obtained from the deflection between the forward and reverse scans. Using the force constant for torsion of 9 N/m yields $\mu \sim 1$. A similar measurement for an experiment with a 40 nN leads to $\mu \sim 0.8$, so we take and average of 0.9. The activation energy at zero stress for methyl thiolate decomposition has been measured previously, and thus yields an equation for the stress-dependent rate constant,

$$k(\sigma_N, \theta) = k_0 exp\left(\frac{(\Delta V_N^{\ddagger} - \mu \Delta V_L^{\ddagger}(\theta))\sigma_N}{k_B T}\right) \tag{4.14}$$

where k_B is the Boltzmann constant and T is the absolute temperature (298 K). The extent of

reaction is then calculated by assuming first-order kinetics for an initially saturated overlayer of

methyl thiolate on copper, with the only variable parameter being $\Delta V_L^{\ddagger}$. Note that it is possible that

the normal and lateral degrees of freedom act in concert to accelerate the reactions rate. For

example, for normal compression, the energy barrier is lowered by stabilization of the initial state.

If the methyl thiolate tilts under the influence of a lateral stress, this may cause additional changes

to the initial-state energy that are not captured by the simple linear model. A relatively small

difference in normal load from 20 to 40 nN causes a significant difference in reaction rate (compare

Figs. 4.9 and 4.10 with Fig. 4.11), which should be captured by this simple model.
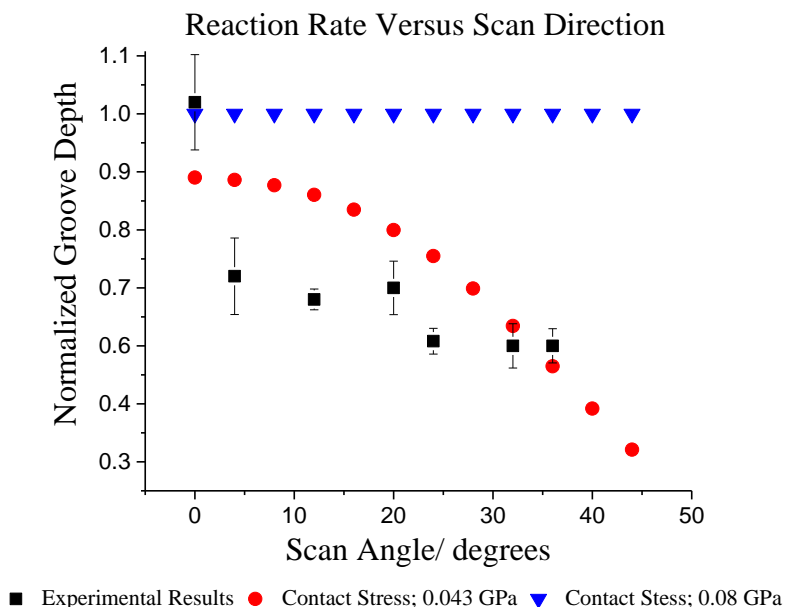
Figure 4.13: Comparison of the experimental variation of the rate of methyl thiolate decomposition as a function of scan angle using a load of 20 nN (■), with the variation predicted by the simple model using a value of the lateral activation volume of 590 Å^3 (●). Shown for comparison is the prediction of the model using this value of activation volume for a normal load of 49 nN (▼).

The results are displayed in Fig 4.13, where the agreement between experiment (■) and theory (●)

is reasonable, and the results indicate that the methyl thiolate species completely decompose using

a tip load of 40 nN, as found experimentally. However, the fit requires an activation volume of

~590 Å^3, which seem unphysically large, and certainly much bigger than the activation volume for normal stress. This may be due to the effects described above, in which the lateral force causes the appearance of a much more complaint initial state. It could also be that the formation of the grooves seen in Fig. 4.9 are not due to methyl thiolate decomposition, but just the lateral motion of the methyl thiolate species out of the rubbed region. Recent calculations of the diffusion barrier for methyl transport from one site to another, show that it proceeds along a similar direction with respect to the surface as the decomposition of methyl thiolates, so that sliding direction of the maximum rate cannot be used to distinguish the two reactions. In addition, the activation barrier for diffusing has been calculated (by Nicholas Hopper) to be ~45 kJ/mol. Assuming a reasonable pre-exponential factor for lateral diffusion,[68] predicts significant mobility of methyl thiolates on copper even in the absence stress. This has been observed from the evolution of the indents formed during compression (see Chapter 3).

4.5 Conclusions

In summary, AFM sliding experiments on a methyl thiolate overlayer on Cu(100) model system have been carried out, and is demonstrated to be a suitable approach to understanding the combined influence of normal and shear stresses. While under the conditions here reported (normal stresses of 0.08 ± 0.01 GPa and 0.043 ± 0.005 GPa, dwell time of 140 s), normal-stress experiments in absence of sliding would produce only a small extent of reaction (on the order of 1-2%), under the influence of a combined normal and shear stress, the reaction proceeds to completion at a normal stress of 0.08 ± 0.01 GPa independent of the sliding direction. Furthermore, at the lower load, anisotropy is evidenced and reveals a maximum extent of reaction when the azimuthal angle of sliding is colinear with the minimum energy pathway for the diffusion of the mechanophore across the surface.

This model system envisions new horizons for studying decomposition and diffusion as mechanochemical activated processes with potential applications in the field of tribology from both experimental and theoretical perspectives.

Chapter 5: Model System for Studying Chemistry in Confined Spaces – Two-Dimensional Silicates

5.1 Introduction

Silicates are by far the most abundant materials in the earth's crust. However, fundamental understanding of the surface properties of silicates down to the atomic scale is limited given the difficulty of studying these non-conductive materials using surface-science methods. Only in the last decade, well-defined model systems for surface-science studies of silicates and aluminosilicates have been developed.[69] The materials discussed in this chapter consist of bilayer (alumino)silicate structures synthesized on a metallic support. Side and top views of the structure are shown in Fig. 5.1. The maximum Al content is given by the stoichiometry $Al_xSi_{1-x}O_2$, where $0 \leq x \leq 0.5$. In addition to allowing surface-science studies of silicates, these bilayer materials also provide a platform for the study of confinement effects, both inside the nanocages in the structure and at the interface with the metal support. The scarcity of model systems for studying chemistry in confined spaces has limited the advancement in this field. While some work studying interfacial confinement has been carried out for traditional 2D materials such as graphene and boron nitride, the silicates described here also allow easier access of small molecules to the interface through the nanopores in the structure.[70] These two-dimensional materials offer an alternative method for selectively applying forces to reactants in addition to the strategy of imposing and external force using a tip against a flat surface discussed in the body of the thesis. As our understanding of the mechanisms that underpin tribo- and mechanochemical reactions develop, such materials with confined spaces could provide an ideal reaction environment for such reactions.
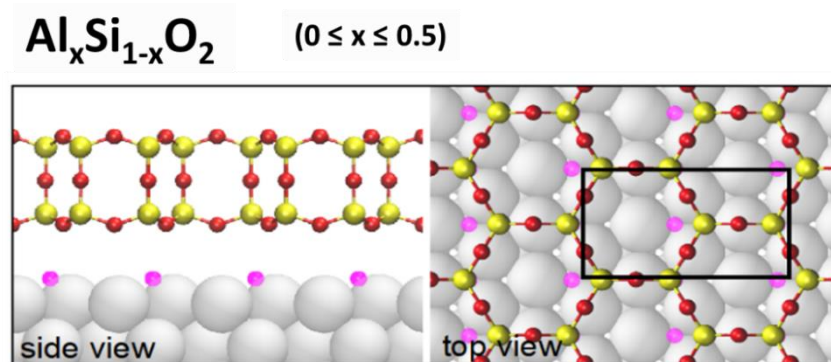
Figure 5.1: Side and top views of bilayer aluminosilicates on a metal support. The yellow circles can be Si or Al. Red circles are O from the silicate framework. Pink circles are O atoms chemisorbed on the metal. Large gray circles are the metal support atoms.

We discuss experimental and theoretical efforts to understand these materials using two-dimensional models, in the context of a collaboration with the Interface Science and Catalysis group at Brookhaven National Laboratory. In the first experiments, we to study the interaction of noble gases with these bilayer silicate materials using ambient pressure X-ray photoelectron spectroscopy at the X1A1 beamline at the National Synchrotron Light Source (NSLS).

The results of these experiments led to postulating this system as a potential candidate for studying the interaction with noble gases in confined spaces. This will be discussed in section 5.3.1. In section 5.3.2, the synthesis of a layered ionic doped silicate called Hexacelsian is described. Hexacelsian consists of a multilayer version of the 2D-bilayer aluminosilicates previously mentioned. Each layer in this structure is anionic, and different layers are separated by cationic species. A delamination protocol to obtain single/few-layer materials on flat supports is discussed in section 5.3.3. It is important to note that the bilayer aluminosilicate structure is also a model system for the most widely used catalyst in the industry, namely zeolites.[71]

Due to low coefficient of thermal expansion, high melting point, and low dielectric constant of mineral aluminosilicates,[72] these analogous thin nonporous materials may be useful for a variety

of applications. Some include traps for atoms or molecules, chemical catalysts, coatings to change surface properties, coatings to protect a surface from corrosion, chemical degradation, material loss, or dendrite formation, and microporous membranes. Scientists have previously used a bottom-up approach to synthesize single-layer nanoporous silica [73] on a metallic surface and shown that they can be used for some of these applications. However, the currently used synthetic method is very time consuming, prohibitively expensive, and produce minimal amounts of material. Part of the work carried out during this thesis has contributed to developing ways to obtain scalable materials for some of the applications mentioned above.

5.2 Experimental Methods

An ultrathin (0.5 nm) aluminosilicate film with a well-defined nano-porous structure grown on Ru(0001) was exposed to different noble gases (Helium, Argon and Xenon) at elevated pressures in an ultrahigh vacuum (UHV) apparatus. The UHV system here used was an Ambient Pressure X-ray Photoelectron Spectroscopy (AP-XPS) apparatus at beamline X1A1 of the National Synchrotron Light Source (NSLS I), at Brookhaven National Laboratory (BNL), New York, USA. Allowing high pressure in the analysis chamber, up to ~1 Torr, this system utilizes differential pumping to protect the Specs Phoibos 150 NAP hemispherical analyzer equipped with a CEM 9 channeltron detector and a 300 μm entrance aperture to the first of three differential pumping stages. The sample was positioned at a small distance of ~300 μm from the aperture to minimize scattering of the emitted photoelectrons by the ambient gas and also to ensure that the local pressure at the surface was not significantly affected by the differential pumping through the aperture. The analyzer was offset by 70° from the incident X-ray beam and 20° from the surface normal of the sample. The aluminosilicate film was prepared on a Ru(0001) substrate with a composition $Al_{0.2}Si_{0.8}O_2$, following the preparation method described in ref.[73]. Briefly, this

includes deposition of 0.8 ML of Si and 0.2 ML of Al on clean Ru(0001) in an O_2 background pressure of 2×10^{-7} Torr, followed by annealing for 10 minutes to 930 °C at an O_2 pressure of 3×10^{-7} Torr, which results in the formation of a crystalline structure. The crystal was mounted on a ceramic button heater to allow the sample to be heated at elevated oxygen pressures using an external voltage supply. The temperature was measured by a type-K thermocouple in contact with the sample.

5.3 Results and Discussion

5.3.1 Trapping of Noble Gases by an Ultrathin Nano-Porous Aluminosilicate Film on Ru(0001)

While it is common to find Argon buried on a surface after Ar+ sputtering of a Ru(0001) sample, the sole exposure of a perfectly clean Ru(0001) sample to gaseous Argon at temperatures higher than 40 K will not retain this gas. In our experiments, however, when the bilayer aluminosilicate framework is present on Ru(0001), room-temperature exposure to elevated pressures (1 mbar) of Ar resulted in it being trapped. The black XPS Ar $2p$ core-level spectrum in Figure 5.3 (a) was the first demonstration of the trapping of Ar by exposure to the gas at 300 K. These experiments were carried out during the last month of operation of NSLS, which was closed in 2014. I was lucky to be part of this historical event and even got to use the last available photons for these experiments. A commemorative t-shirt I was given is shown in the figure below.

Figure 5.2: Shutdown of the National Synchrotron Light Source, commemorative t-shirt.

These experiments were repeated using the new synchrotron at BNL (NSLS-II), which started

operations soon after the closure of NSLS, to obtain higher quality and more detailed data.[74,75]
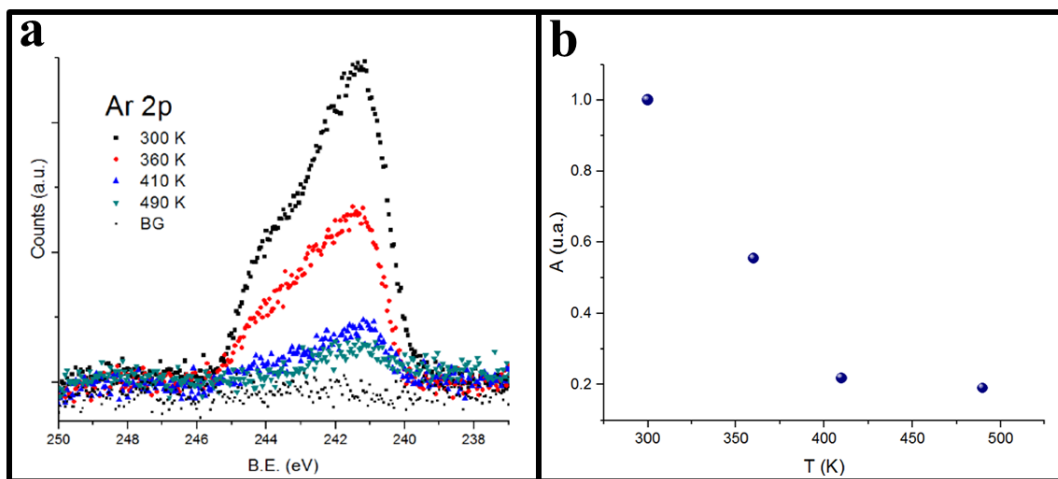
Figure 5.3: (a) Ar 2p spectra as a function of temperature after exposure of an aluminosilicate film on Ru(0001) to 1 mbar of Ar. (b) Plot of the relative amount of Argon versus temperature.

While the presence of Ar was confirmed by XPS, it remained to be determined if the Ar atoms

were trapped within the hexagonal prism nanocages that compose the aluminosilicate framework

64

or at the interface with the Ru(0001) support. The possible trapping locations are shown in Figure 5.4.
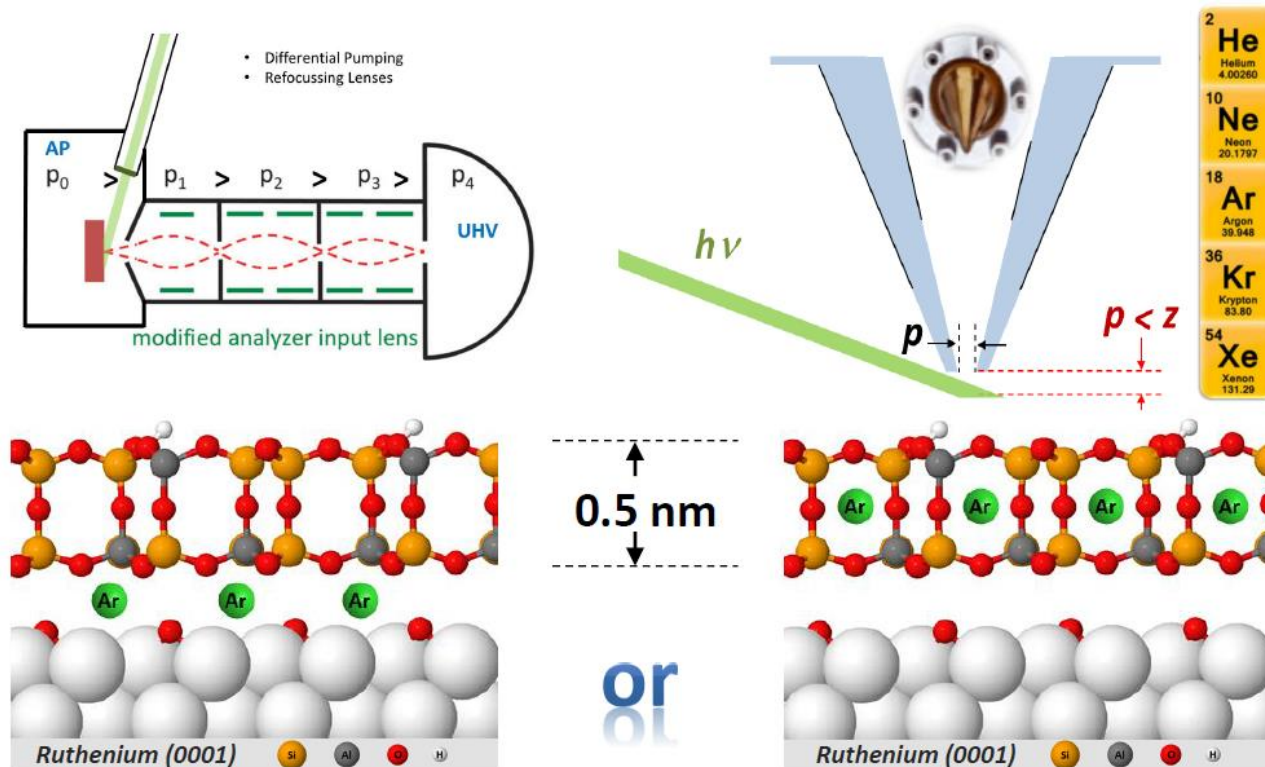
Figure 5.4: Argon is trapped by $Al_{0.2}Si_{0.8}O_2$/Ru(0001) when exposing the structure to 1 mbar of the gas at 300 K. Ar atoms can be trapped at the interface between Ru(0001) and the aluminosilicate framework and/or within the hexagonal prism nano-cages that compose the aluminosilicate structure.

Temperature dependence of the AP-XPS spectra is shown in Figure 5.3 (a). The normalized amount of Argon trapped as a function temperature can be obtained from the relative areas of the AP-XPS Ar $2p$ peaks (plot shown in Figure 5.3 (b)). This plot shows that some Argon remains on the surface even after heating to 490 K and only completely desorbs after annealing to 1100 K.
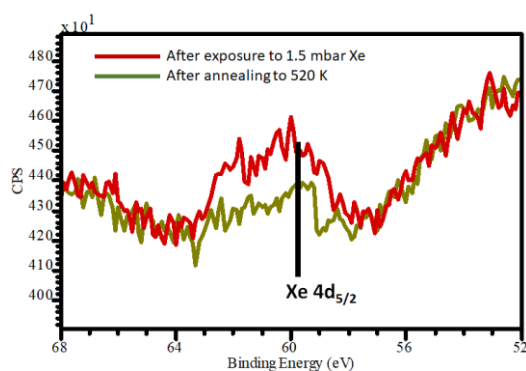
Figure 5.5: Xe 4*d* core level XPS spectrum after exposure to 1.5 Torr Xe at 300 K (red), partial desorption after 520 K annealing is observed (green).

In order to compare the behavior of Ar with other noble gases, experiments were also carried out using He and Xe. Helium, much lighter than Ar, does not remain on the surface upon exposure to elevated pressures. Xenon, on the other hand, does remain on the surface, but the trapped amount seems lower than for Ar. The red spectrum in Figure 5.5 shows a Xe 4*d* core level spectrum after exposure of the aluminosilicate bilayer to 1.5 Torr Xe at 300 K followed by evacuation, demonstrating the trapping of the gas. The green spectrum corresponds to the same sample after annealing to 520 K, which results in partial desorption of the trapped Xe. The spectra were acquired at the X1A1 beamline of NSLS, using a photon energy of 675 eV.

This experiment opened new investigation avenues for the trapping of noble gases and the understanding of confinement effects. Additionally, different applications of these and related materials have stemmed from this research, and a provisional patent application related to this work has been filed (Boscoboinik et al., - Provisional S.N. 62/946,688 - Filed December 11, 2019 - Application Entitled "Oxide Polygonal Prism Nanocages for Trapping of Gases"). More recently, Brookhaven National Laboratory and Forge Nano Inc., were granted an award by the DOE Technology Commercialization Fund to develop and scale up this technology for nuclear energy applications (https://mailchi.mp/4345fd533a86/doe-ott-latest).

5.3.2 Hexacelsian Synthesis

Bilayer aluminosilicate structures were successfully prepared in the past, as described in previous sections. However, the bottom-up approach used for the synthesis of these 2D materials is prohibitively expensive for scaling up production.[73] Therefore, there is an increasing need for developing alternate synthesis protocols with lower costs.
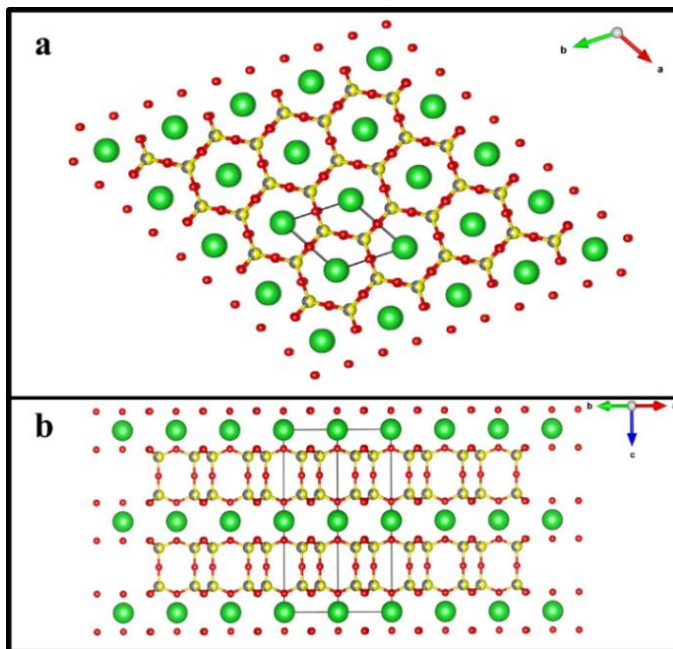
Figure 5.6: Hexacelsian structure, (a) top view and (b) side view of the layered material intercalated by barium atoms (green). Red spheres represent oxygen atoms and yellow/grey are either sodium or aluminum in the aluminosilicate bilayer. (Vesta software)

The synthesis of a bulk layered material called hexacelsian, whose delamination can result in an inexpensive way of obtaining bilayer aluminosilicates, is discussed in this section. A representation of the hexacelsian structure consisting of a multilayer 2D-aluminosilicate, where each layer is separated by barium ions, is shown in Figure 5.6.

The synthesis consists of an ion exchange process in which Sodium in Na-LTA zeolite is exchanged by barium ions from a saturated solution of $Ba(NO_3)_2$ to produce Ba-LTA. The process involves incorporation and continuous mixing of Sigma Aldrich Na-LTA (1 gram for the

experiments here performed) in 20 mL of barium nitrate solution for 12 hours at 70 °C After filtering and washing with deionized water the product, a drying period of 12 hours at 80 °C was performed. Following, a calcination process of 30 hours at 900 °C leads to formation of the hexacelsian phase. The chemical equation for the ion exchange and process diagram are shown in Figure 5.7.

a
$$Na_2 - LTA(s) + Ba^{2+}(aq) \rightarrow Ba - LTA(s) + 2Na^+(aq)$$

b
Zeolite A 1 g +
20 mL $Ba(NO_3)_2$ Saturated Solution

$Ba(NO_3)_2$ solubility 9.29% w/w at 25°C
1 g H_2O_____0.0929 g $Ba(NO_3)_2$
20 g H_2O_____1.858 g $Ba(NO_3)_2$
https://pubchem.ncbi.nlm.nih.gov/compound /barium_nitrate#section=Solubility

Overnight (12 hours) stirred 50 rpm
T = 70°C

Filtrate

Wash: double destiled water
Dried overnight T = 80°C

Product

c
3 hs
5°C/min

15 hs
900°C

3 hs
5°C/min

25°C

25°C

$Ba - LTA$

$Hexacelsian$

Figure 5.7: Hexacelsian synthesis protocol (a) Ion exchange reaction (b) diagram of the ion exchange protocol and (c) calcination procedure.

The characterization of the obtained hexacelsian phase was performed in the context of a collaboration with Universidad de San Luis, Argentina, and Brookhaven National Laboratory in partnership with Dr. Celeste Bernini and Dr. Andres Alberto García Blanco. X-ray powder diffraction (XRD) patterns were obtained for the samples prepared following the previously described protocol. The diffraction patterns obtained reproduce previously reported hexacelsian

diffractograms, as shown in Figure 5.8. Insets with H and * labels correspond to hexacelsian diffraction peaks in the literature.[76,77] There are some unidentified peaks, which could be related to the presence of impurities. For the case of the spectra associated with the product of the synthesis here described, some of these unassigned peaks are absent thus potentially reflecting absence of concomitant structures.
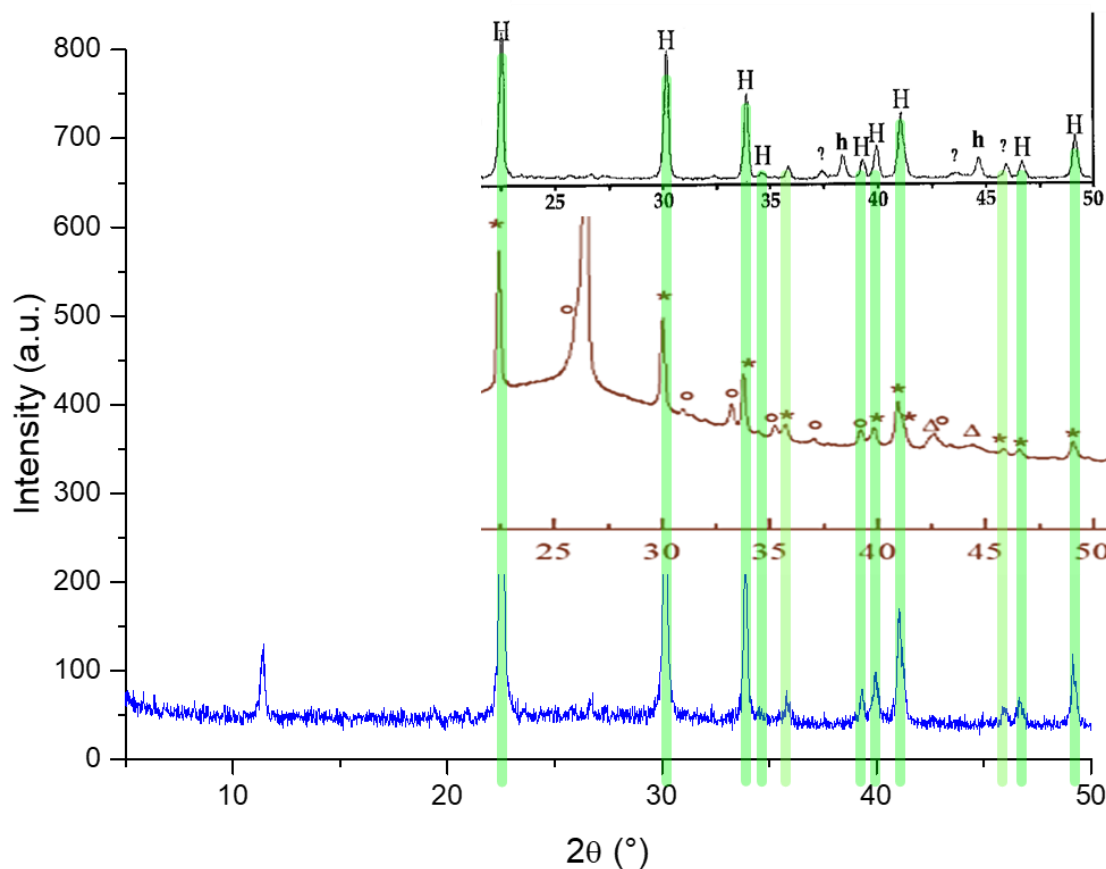
Figure 5.8: X-ray powder diffractogram of obtained hexacelsian (blue) and comparison with literature (black[76] and brown[77] insets). Green lines serve as a guide to the eye for the hexacelsian signals (labeled as H in top inset and * in bottom inset).

5.3.3 Hexacelsian Delamination and Characterization

The hexacelsian layered material, the product of the protocol described in section 5.3.2, was further subject to a delamination process. This consists of performing a 15 min ultrasonic bath treatment

of the powder sample suspended in a water-based solvent. After sonication, the delaminated sample was filtered. The samples utilized in this work have been subject to only one delamination cycle. However, the process can be repeated as many times as desired after the redispersion of the solid sample in the solvent as represented in Figure 5.9.
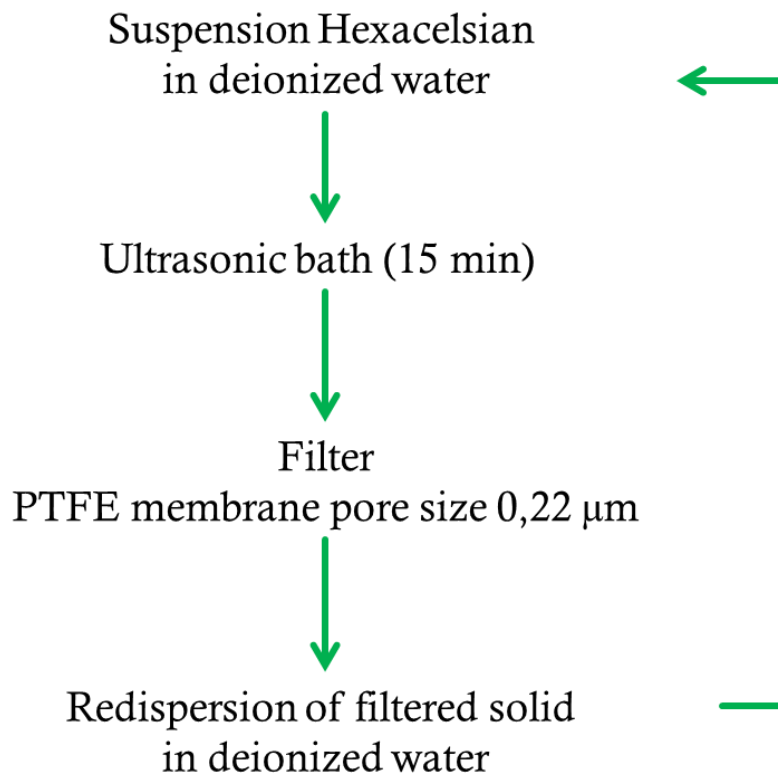
Figure 5.9: Diagram of delamination protocol where the solvent is deionized water.

Fourier-transform infrared spectroscopy (FTIR) spectra before and after the delamination process were obtained and show an increase in definition of the characteristic silica film band [78] centered at 1225 cm^{-1} for all solvents used during delamination protocol (See Figure 5.10). Furthermore, William H. Hoffmann at BNL obtained XRD patterns and XPS spectra for the delaminated materials in agreement with the results discussed here. AFM images of the delamination product

showed proof of delamination efficiency up to single-layer thickness. In these AFM results, partial delamination with a thickness between 3.5 nm and 4.5 nm has been reported, indicating 7-9 bilayer-thick flakes (this unpublished data part of internal BNL reports and therefore not shown here).
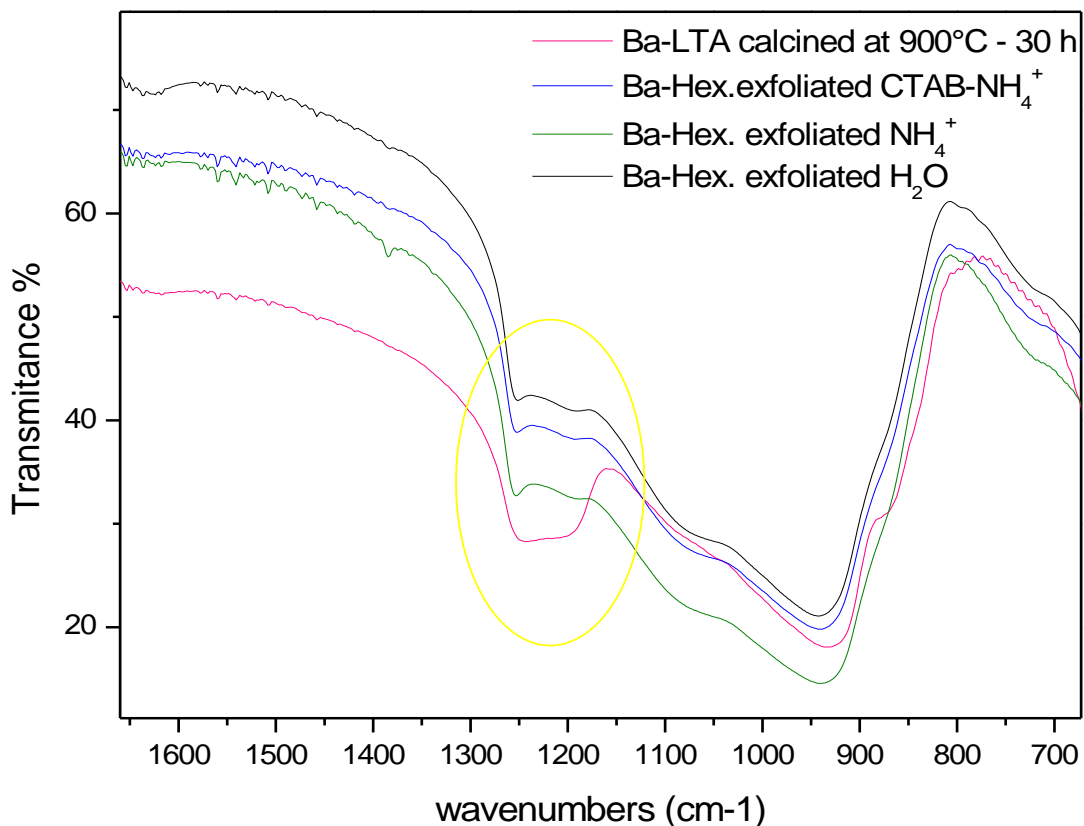
Figure 5.10: FTIR spectra of hexacelsian (Ba-LTA calcined at 900ºC) and exfoliated products under the presence of three different solvents.

No other delaminated ionic nanoporous ultrathin layered silicates have been obtained before from ionic layered materials, with a number of layers between 1 and 20. The cages that form this material can trap gases, resulting in many useful applications.[74,79]

5.4 Conclusions

In summary, proof-of-principle experiments have been carried out to demonstrate that 2D silicates on metallic supports are suitable materials for trapping individual noble gas atoms at non-cryogenic temperatures and could provide a platform for studying mechanochemical reactions.[75] Indeed, experiments, not shown here, but published in collaboration with others, have shown that the interfacial confinement could enable new chemistry.[74] While of great fundamental importance, the materials used for noble gas trapping are not scalable for practical applications. Considering this, an experimental top-down approach protocol for the synthesis of a layered precursor of the 2D-silicates has been presented. First, steps toward delamination were explored, aiming at producing single to few-layer materials. These were characterized using surface science methods. The synthesis protocol here described have the potential to scale the production and reduce the costs considerably of these 2D materials.

This work has opened new avenues of research and potential applications of these materials, including a patent, and a potential pathway for commercialization of these materials for some noble gas trapping applications in nuclear reactors.

Appendix 1: Surface Structural Changes of Furfural on Pd(111) by Means of IRRAS

A1.1 Introduction

In order to produce value-added products from lignocellulosic biomass, the raw material (cellulose, hemicellulose) is typically hydrolyzed to the corresponding carbohydrate monomers, glucose, fructose, and xylose, using acid catalysis.[80–83] Subsequent acidic dehydration leads to the formation of smaller oxygenates such as furfural (FF), 5-hydroxymethylfurfural (HMF), and levulinic acid (LA). These products can be used to produce fuels and polymers or for synthesizing other monomers relevant to the polymer industry.[81,83–88] However, many of the current methods for transforming such feedstocks are often dirty and energy-consuming;[80–82,86–88] for example, FF is upgraded using a toxic copper chromite catalyst,[89,90] at high pressures.

It would thus be advantageous to develop a catalyst for converting furfural to more valuable feedstocks [87,91] and palladium has been identified as a selective catalyst for the hydrogenation of furfural to methyl furan and dimethylfuran.[86,92–95] This has prompted investigations of the chemistry of furfural on Pd(111) single crystal model catalysts.[96] In particular, it has been proposed experimentally [97,98] and theoretically [97] that the adsorbate coverage controls the selectivity, with flat-lying species leading to decarboxylation and the formation of furan and tetrahydrofuran, while tilted conformations result in furfural hydrogenation to furfural alcohol or 2-methyl furan.

However, there have been no infrared spectroscopic investigations of the adsorption of furfural on Pd(111) that would provide direct experimental verification of the orientation of the adsorbates from the surface infrared selection rules.[99] This is addressed in the following by investigating the surface adsorption and structural changes of furfural on a Pd(111) single crystal in ultrahigh

vacuum (UHV) by using Infrared reflection-absorption spectroscopy (IRRAS) as a function of coverage and temperature.

Temperature-programmed desorption (TPD) experiments of furfural on Pd(111) [96] show molecular desorption in a broad state centered at ~355 K extending between ~300 and 450 K. The formation of furan is found at 295 K, where pre-adsorbed deuterium shows the incorporation of two deuterium atoms in the product and some propylene is formed in a broad peak at ~370 K, assigned to a furan ring-opening reaction.

Detailed density functional theory (DFT) calculations reveal different structural orientations of furfural on Pd(111).[100] At lower coverages, the most stable conformation is with the furan ring lying flat on the surface, centered over a hollow site, while more weakly bound tilted species form at higher coverages, in accord with previous work.[96,101,102] More weakly adsorbed species, namely a bent configuration with a furan ring tilted away from the surface and an upright structure, may be stabilized at higher coverages.[103]

A1.2 Experimental Methods

Infrared reflection absorption spectra were collected using a Bruker Equinox spectrometer equipped with a liquid-nitrogen cooled mercury cadmium telluride (MCT) detector. The light path is enclosed in plexiglass boxes and continuously purged with dry, CO_2-free air. The infrared cell consists of a six-way 2 3/4" cube coated with gold to minimize inner wall adsorption of contaminants, with two infrared-transparent KBr windows along the IR beam path. A palladium (111) single crystal was mounted in a coaxial, differentially pumped manipulator which could be resistively heated to 1200 K or cooled to 80 K using liquid nitrogen. The transfer arm allows 360° rotation and displacement of the sample back and forth between the IR cell and a 12-inch-diameter bell jar main chamber (Prep. chamber in Figure A1.1).
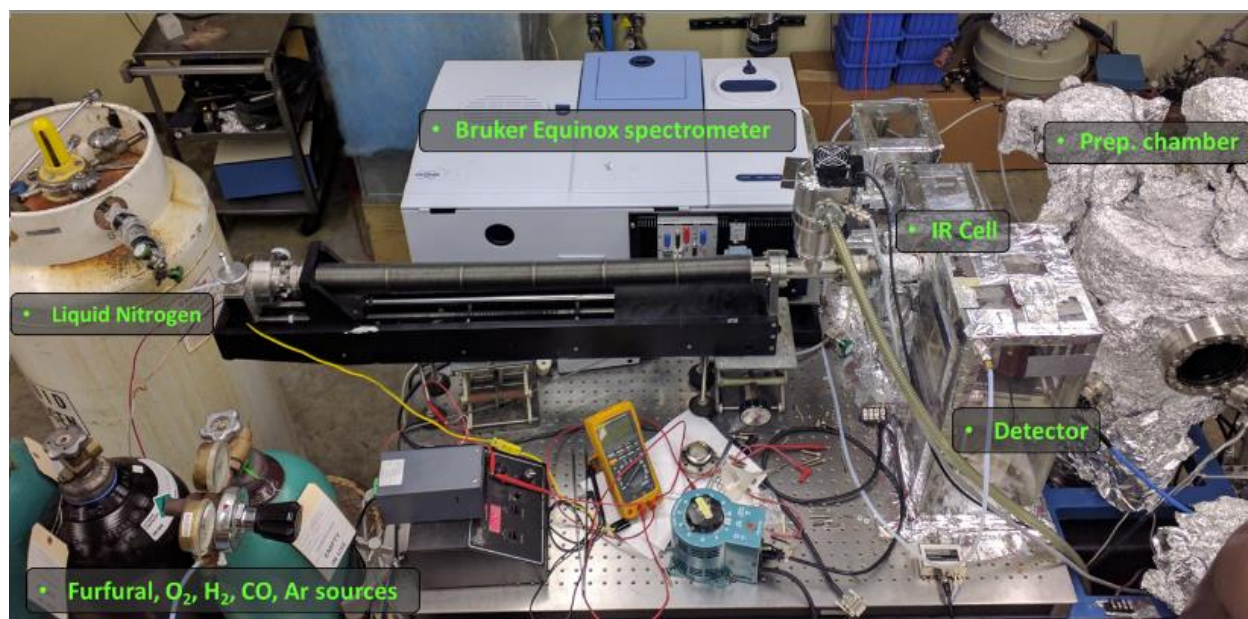
Figure A1.1: Experimental setup utilized for infrared reflection absorption spectroscopy studies of furfural on Pd(111).

The main chamber is pumped by a combination of rotary, turbomolecular and an ion pumps and serves as a sample preparation chamber and is equipped with an ionization gauge for measuring the background pressure, an ion gun for sample cleaning, leak valves for introducing gases for sample preparation and dosing, and a double-pass cylindrical mirror analyzer (CMA) for sample characterization by Auger spectroscopy. Cleaning of the sample is performed following a protocol of Argon bombardment, annealing and heating in oxygen at varying temperatures and a background oxygen concentration as summarized in Figure A1.2. Furfural (Aldrich, > 99.9% purity) was transferred to glass bottles and attached to the gas-handling systems of the vacuum chamber and further purified by several freeze-pump-thaw cycles.
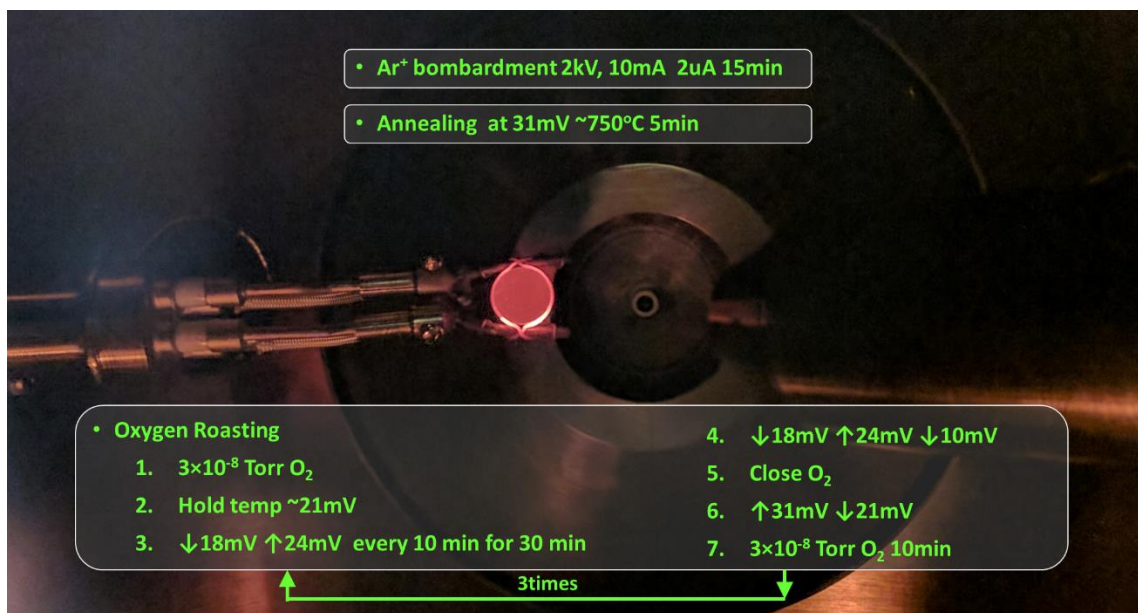
Figure A1.2: Diagram of the cleaning protocol for Pd(111), consisting of three sequential steps, argon bombardment, annealing and oxygen roasting. Photograph of the sample while annealing is shown as background.

A1.3 Results and Discussion

A1.3.1 Furfural Uptake

The surface chemistry of furfural adsorbed directly on clean Pd(111) was studied by initially adsorbing it on clean Pd(111) at ~90 K. The spectral changes during adsorption are displayed in Figure A1.3, where the relative coverage for each dose is indicated and how the coverages were obtained is described below. The spectra show two distinct regimes. The first is for furfural adsorbed at the lowest dose (indicated as a furfural coverage of 0 ML), which shows no intensity in the carbonyl stretching region at ~1707/1677 cm^{-1}, indicating that the C=O bind lies parallel to the surface and is not detected due to the surface infrared selection rules.[104] This has an associated weak peak at ~1610 cm^{-1}, presumably a shifted carbonyl stretching mode weakened by interaction with the surface. The associated aldehyde C–H mode at ~1367 cm^{-1} is still evident, indicating that

76

this vibration has a component perpendicular to the surface, and the presence of peaks at 1571 and

1465 cm^{-1} suggest that the furan ring is not perfectly parallel to the Pd(111) surface in this close-

to flat-lying species.
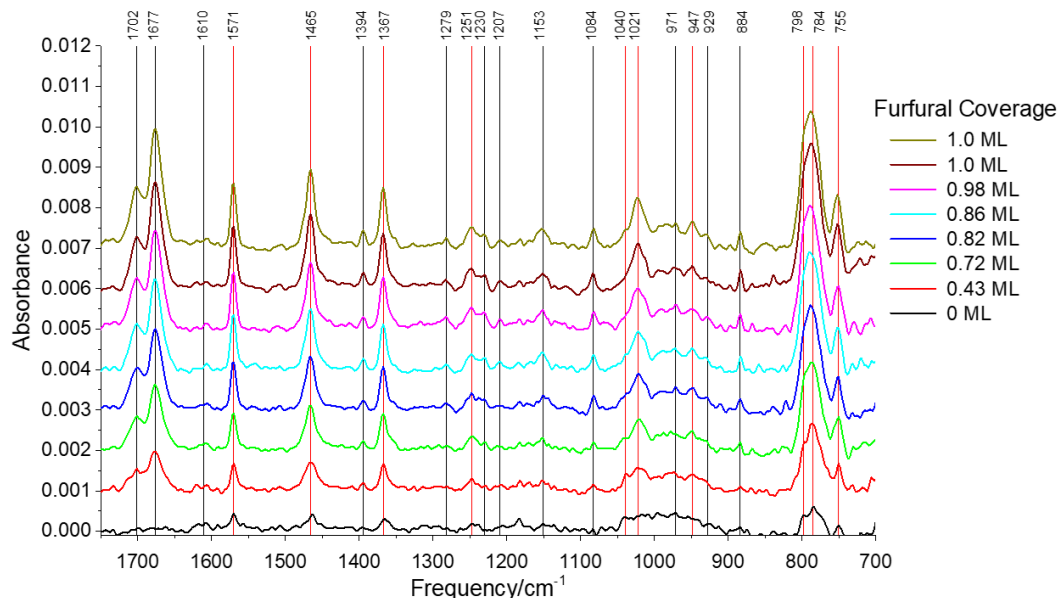
Figure A1.3: Infrared spectra of low coverages of furfural adsorbed on Pd(111) at ~90 K as a function of furfural coverage, where the coverages are indicated in the figure.

Higher furfural exposures produce a drastic change in the infrared spectra and cause the carbonyl

modes to appear suggesting that the furfural adopts a more tilted geometry at higher exposures.

The vibrational frequencies are close to those found for the furfural multilayer (Figure A1.6, Table

A1.1), indicating that furfural adsorbs molecularly on Pd(111) at low temperatures. These

vibrational frequencies are in accord with the group frequencies expected for 2-substituted furans,

which are characterized by peaks at 1605 to 1570 cm^{-1} (1571 cm^{-1} in furfural), 1510 to 1475 cm^{-1}

(1465 cm^{-1} in furfural) and from 1400 to 1380 cm^{-1} (1395 cm^{-1} in furfural).[105–107] In particular, the

carbonyl stretching modes are close to those found in the multilayer (Fig. A1.6), implying that the

aldehyde group is not shifted by interaction with the palladium surface,[108,109] indicating that the

carbonyl groups are remote from the surface.
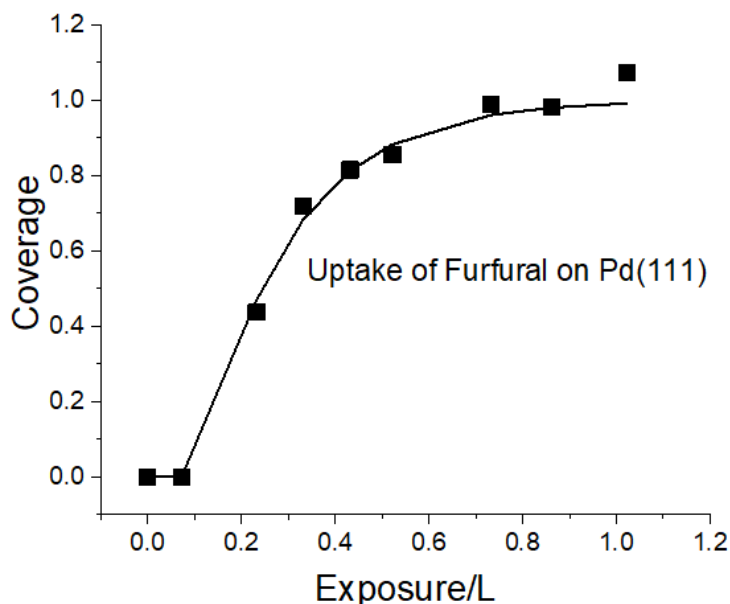
Figure A1.4: Uptake for furfural on Pd(111) at low temperatures from the variation in the integrated intensity of the carbonyl stretching modes as a function of exposure.

Adsorption into the high-coverage regime is characterized in Figure A1.4, where the presence of a tilted furfural adsorption state is gauged from the variation in the intensity of the carbonyl stretching modes as a function of exposure, and the results are used to calibrate the coverages shown in Figure A1.3. Note that, since the flat-lying species exhibit negligible carbonyl stretching intensity, uptake into this state is not included in Figure A1.3. The spectra for the tilted species show modes at 1702 and 1677 cm^{-1} indicating the presence of both the cis and trans conformers of furfural following adsorption at ~90 K.[110–112] Measuring the ratios of the intensities of the 1702 and 1677 cm^{-1} modes as a function of exposure reveals that they are independent of the furfural coverage and using the absorbance values for these modes [112] indicates that ~40% of the furfural exists as the cis conformer and ~60% as the trans conformer.
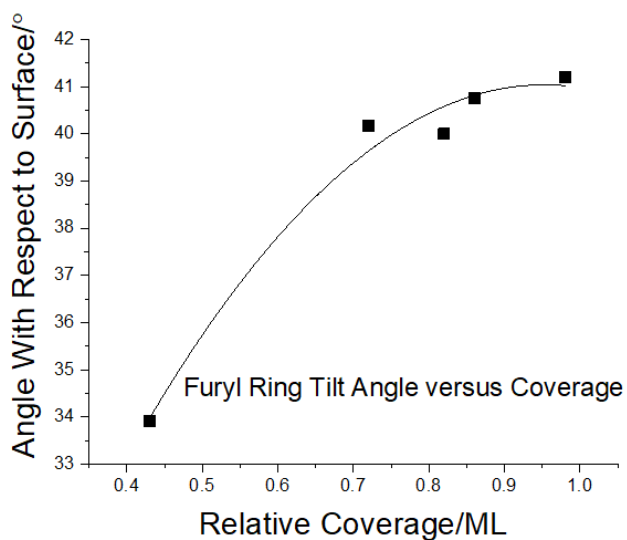
Figure A1.5: Plot of furfural tilt angle with respect to the surface as a function of the relative coverage of furfural adsorbed on Pd(111) at ~90 K.

The variation in tilt angle with coverage is calculated from the variation in the intensity of an A'

(at 1465 cm^{-1}, Table A1.1) and A" (784 cm^{-1}, Table A1.1) modes as a function of coverage, by

calibrating the intensities using the absorbance values in the literature.[112] The results are displayed

in Figure A1.5, which shows that the furfural tilt angle varies from ~35° with respect to the surface

at a relative coverage of ~0.4 ML to ~41° as the coverage approaches saturation. Vlachos and co-

workers have identified two types of tilted species on Pd(111) by DFT,[97] a so-called Tilted-1

species in which the furfural adsorbs via the CHO group to the Pd(111) surface and a Tilted-2

species, which adsorbs via the furan ring. Both have a molecular tilt angle of ~35° with the surface,

in the range of the values measured experimentally (Figure A1.5). Since the spectra of furfural on

Pd(111) at ~90 K show no significant shift in the carbonyl stretching modes, this suggests that it

adsorbs in the Tilted-2 configuration.

79

A1.3.2 High Dose Experiments -Formation of Thick Multilayers

Upon extended exposure of Pd(111) to furfural, multilayer adsorption was observed. Experiments were performed on sample formed by producing a thick furfural multilayer on the crystal at low temperature. The temperature dependence of molecular structural changes is studied by flash annealing the sample to a target temperature and then always allowing it to cool down to ~84 K to proceed to record infrared spectra of the sample. The infrared spectrum of multilayers of furfural adsorbed on Pd(111) and heated to various temperatures is displayed in Figure A1.6 with the vibrational frequencies displayed adjacent to each peak.

Gas-phase Furfural Frequencies/cm^{-1}		Furfural Multilayer on Pd(111)/cm^{-1}		Furfural Monolayer on Pd(111)/cm^{-1}	Symmetry
Cis	Trans	Cis	Trans		
3124	3134	3110	3137	-	A'
2813	2855	2813	2856	-	A'
1692	1675	1703	1677	1702, 1677	A'
1565	1569	1567	1571	1571	A'
1474	*1465*	1475	1465	1465	A'
1394	1394	1394	1394	1394	A'
1367	1367	1367	1367	1367	A'
1278	*1246*	1279	1251	1279, 1251	A'
1222	1208	1230	1207	1207, 1230	A'
1157	1149	1153	1153	1153	A'
1077	1083	1084	1085	1084	A'
1021	1015	1021	1021	1040, 1021	A'
930	*946*	929	947	947, 929	A'
883	883	884	884	884	A'
842	842	842	842	-	A"
768	768	789	789	798, 784	A"
755	747	755	755	755	A'

Table A1.1: Assignment of the infrared spectrum of furfural multilayers and monolayers on Pd(111).

The peaks are assigned by comparison with the gas-phase spectrum for furfural [110,112] and are summarized in Table A1.1 and are in excellent agreement with the gas-phase spectrum, indicating the presence of pure furfural molecular adsorption on the surface. Furfural belongs to the C$_s$ point

group and the symmetry assignments of the vibrational modes are included in Table A1.1. This indicates that the majority of the normal modes are of A' symmetry, with only the 842 and 799 cm^{-1} modes having A" symmetry and are due to out-of-plane ring modes and are highlighted in bold in Figure A1.6. The peaks at 3136 and 2856 cm^{-1} are due to C–H stretching modes where the 2856 cm^{-1} mode is the aldehyde C–H stretch. The peak at ~1367 cm^{-1} is the C–H rocking mode of the aldehyde group. Furfural can exist in two conformers depending on whether the aldehyde carbonyl group is adjacent to (cis) or distal from (trans) the furan ring oxygen. This is manifest by shifts in the frequencies of some vibrational modes, in particular of the carbonyl stretching modes, where the 1677 cm^{-1} mode is due to the trans conformer, while the 1703 cm^{-1} peak is assigned to the cis structure. Other features that show similar cis-trans splits are the 1279/1251, 1230/1207 and 929/947 cm^{-1} doublets due to C–H in-plane bending vibrations, where the first wavenumber is pertinent to the cis conformer and the latter to the trans.

The presence of modes with both A' and A" symmetry indicates that the furfural in the multilayer is randomly oriented on the surface. The multilayer infrared spectrum remains essentially unchanged as the sample is heated to ~125 K, but the relative intensity of the ~789 cm^{-1} peak decreases as the sample is heated to ~150 K indicating that annealing the furfural overlayer causes the furan ring plane to increase its tilt angle with respect to the surface, and is accompanied by an increase in the ~1700 cm^{-1} peaks intensity suggesting that the carbonyl (C=O) group more perpendicular to the surface.
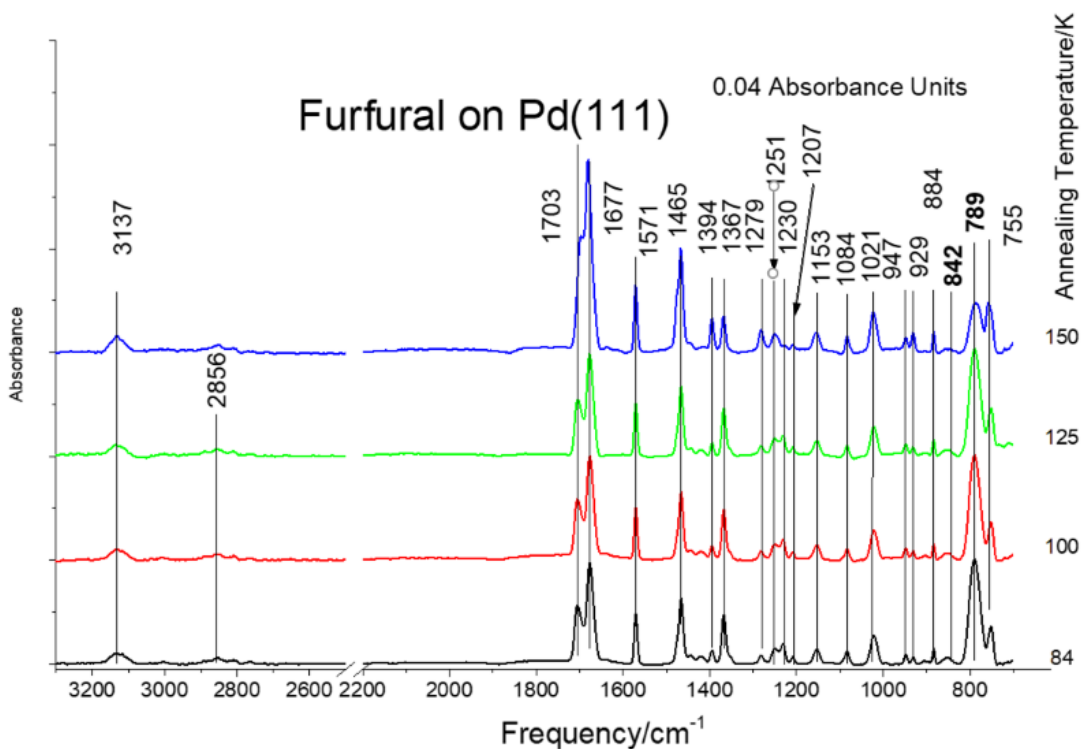
Figure A1.6: Infrared spectra of a furfural multilayer adsorbed on Pd(111) at 84 K and annealed to various temperatures where the annealing temperatures are indicated adjacent o the corresponding spectrum.

Further annealing to 175 K shows the appearance of a very intense peak located at 790 cm^{-1} (See Figure A1.7). Since this is an out-of-plane vibrational mode, its appearance is interpreted as being due to a concerted reordering of the overlayer structure to produce an almost completely flat molecular orientation within a crystalline phase on Pd(111). The appearance of this peak is accompanied by the presence of signals due to the cis conformer of furfural as part of the signature of this highly-ordered structure. Significant sharpening of the broad C–H stretching vibrations at 2813 and 3110 cm^{-1} are also indicative of promotion of cis over trans isomers, as shown by the assignments listed in table A1.1.
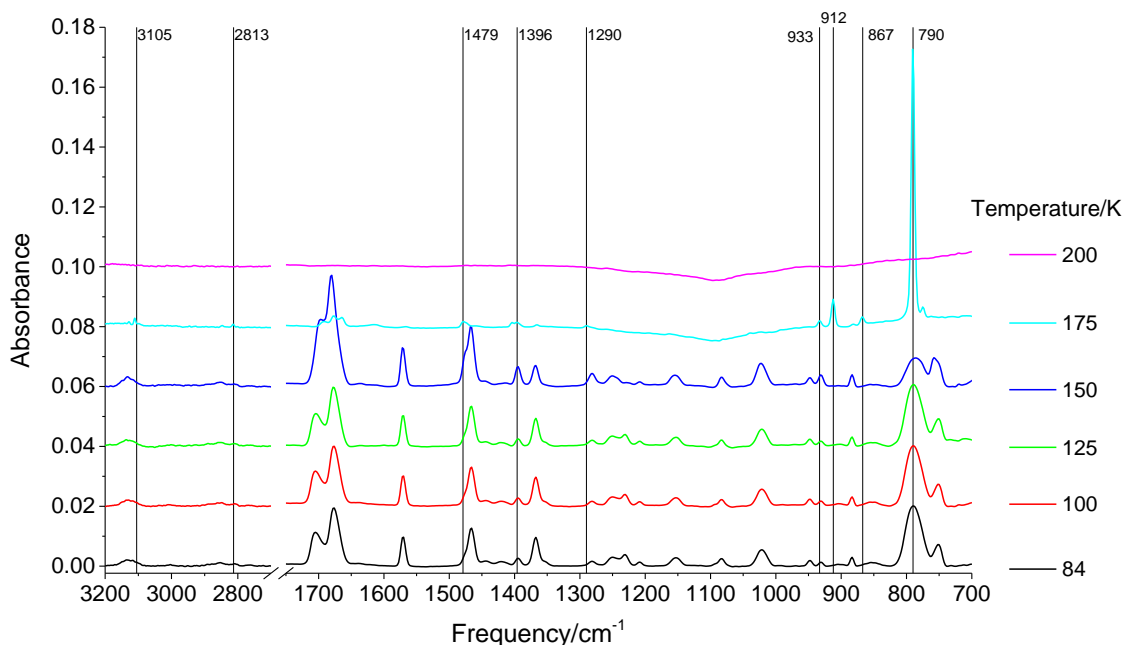
Figure A1.7: Multilayer spectra of furfural adsorbed at 80 K on Pd(111) and then annealed to higher temperatures showing mostly a peak due to flat-lying furfural at 790 cm^{-1} on heating above 175 K. The spectrum also shows peaks that are signatures of the cis conformer of furfural.

To further investigate this phenomenon, a clean Pd(111) sample was exposed to 10L of furfural at 170 K and, as described in previous experiments, cooled to 80 K to collect the IR spectra (See Figure A1.8), sequentially flash heated to higher temperatures (values given in legends), and all IR spectra were obtained after cooling to 80 K. At 170 K, between the transition temperatures previously described (150 K – 175 K in Figure A1.7), a sharpening and increase in relative intensity of the 790 cm^{-1} out-of-plane CH mode is indicative of a structure with a smaller tilt angle of the furfural molecular plane with respect to the surface. The signals corresponding to the high-frequency cis conformer and combined cis/trans ring modes are still observed for which the presence of a tilted geometry is still evidenced. Annealing to 180 K produces a spectrum with a very intense, sharp out-of-plane 790 cm^{-1} mode, the infrared spectra of this species has not hitherto been reported in the literature.
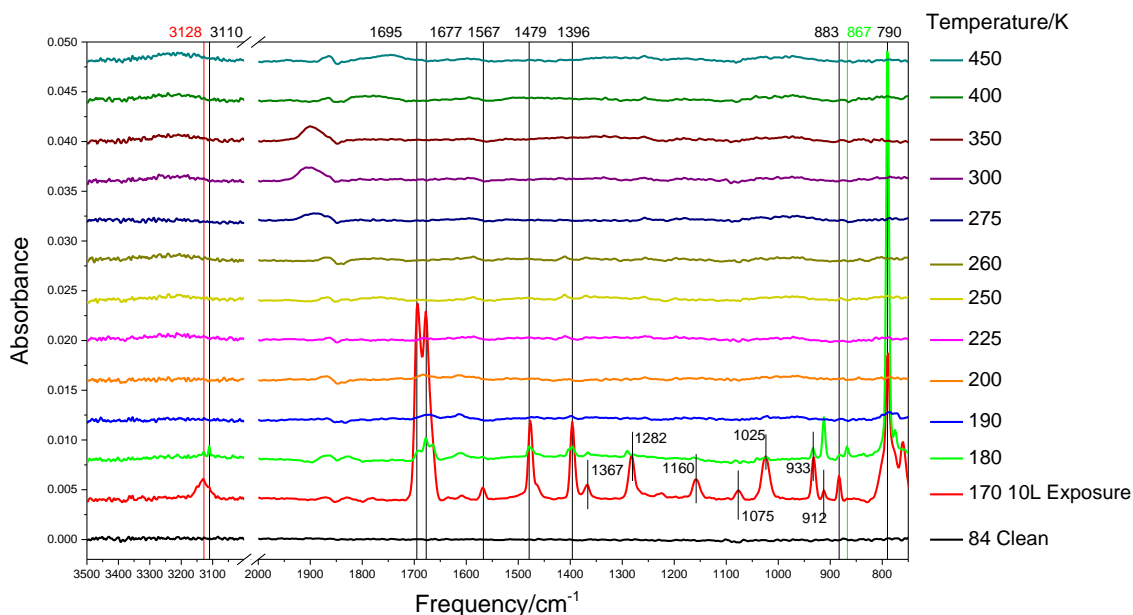
Figure A1.8: Infrared spectra after a 10 L FF exposure on Pd(111) at 170 K to capture the transition from the tilted into a more flat-lying configuration of this phase that contains predominantly cis-furfural. Spectra were always collected at 84 K after flash annealing to a target temperature (specified in the legend) and by allowing the sample to cool to 84 K to collect the spectrum.
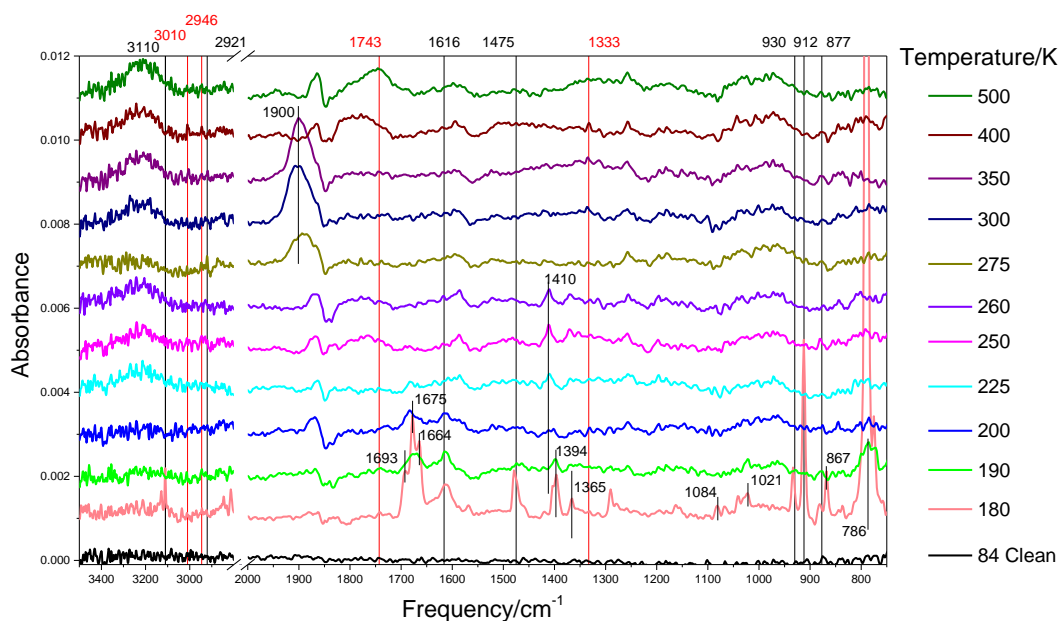
Figure A1.9: Close up of 180 K for signal labeling and close caption of the chemistry occurring at more elevated temperatures.

A more detailed view of the spectra collected after annealing to 180 K and higher temperatures is

shown in Figure A1.9, where the frequencies have been labeled for the peaks of this crystalline

phase. The formation of a crystalline structure by annealing to ~180 K is a result of the molecules achieving enough energy to be able to transition into a more stable phase, possibly stabilized by a hydrogen-bonding network as reported in the work of Seidel et. al. [113] who studied the crystallization of furfural by cycles of heating from 100 K (in a cold nitrogen gas stream) to 5 K below the melting point (~237.17 K) and further recrystallizing at 100K. The furfural was contained inside an open diameter capillary (1 cm long by 0.5 mm diameter) to measure the X-ray diffraction patterns. A diffractogram obtained at 100 K was indicative of the formation of a single-crystal of furfural and the analysis of the diffraction pattern produced a crystal structure displayed in Figure A1.10. The crystal is comprised of weak hydrogen-bonded networks of only the cis conformer [113] and is consistent with the conformational changes observed in the infrared data here reported, corresponding to the IR collected at 84 K after flash annealing to 180 K, highly crystalline structure of the IR spectra shown in Figure A1.9.
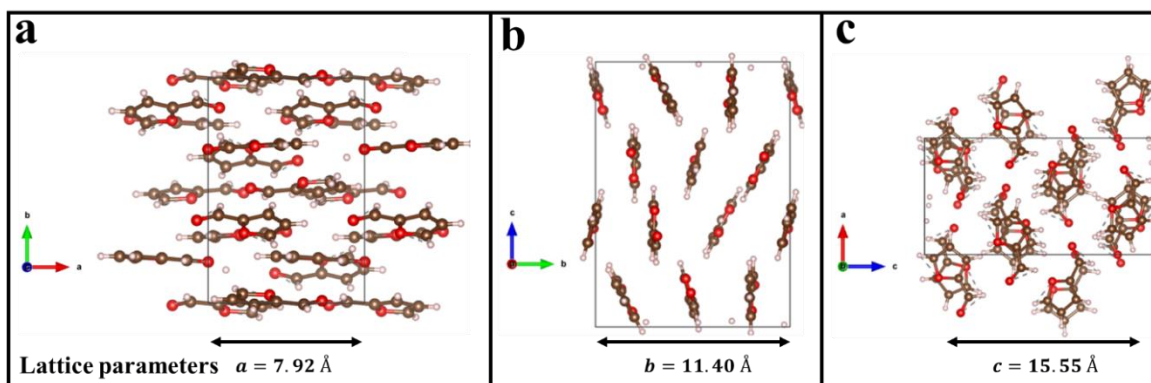
Figure A1.10: Structure obtained from coordinates given in literature[113] for single crystal furfural. (Vesta Software)

As the sample is annealed to much higher temperatures, there is evidence of thermal decomposition of furfural on Pd(111) that will be discussed in greater detail elsewhere. High-frequency modes from the aldehyde (2800-2850 cm^{-1}) and CH$_3$ (3000-3200 cm^{-1}) groups become narrower during this transition (on heating from 170 to 180 K), as shown in Figure A1.11. The sharpening of these

peaks in the lower 2813 and 3110 cm^{-1} wavenumbers is also indicative cis conformer being promoted from our assignments listed in Table A1.1. Further annealing causes those signals to disappear, due to decarbonylation, furan production and ring-opening processes which will be analyzed in detail elsewhere.
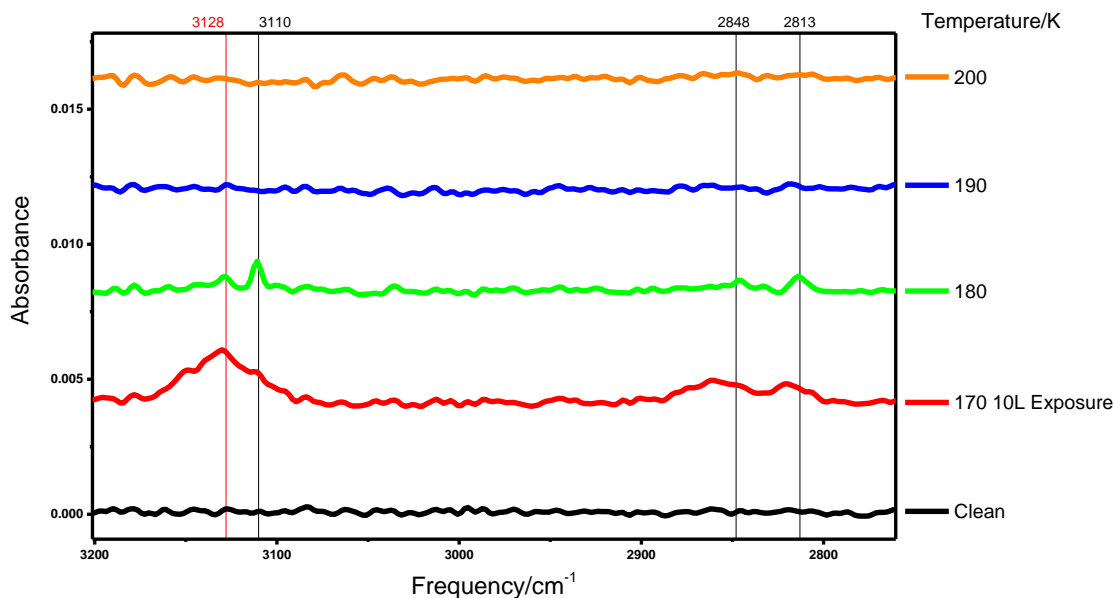
Figure A1.11: Detailed view of the high-frequency region of the spectra for furfural on Pd(111) where the annealing temperatures are indicated on the figure. Broad features sharpen in the region of cis conformer signals at 3110 and 2813 cm^{-1} at 180 K.

A1.3.3 Experiments on Intermediate Furfural Doses – Formation of Thin Multilayers

The spectral changes found during adsorption at 80 K were displayed in Figure A1.3. The final dose (with a 1 L exposure) in Fig. A1.3, here indicated as an intermediate dose, is used to study the temperature evolution of the infrared spectra by annealing briefly to a particular temperature, and then allowing the sample to cool at ~90 K, at which temperature the infrared spectra were

collected. The results are displayed in Figure A1.12, where the annealing temperatures are indicated.
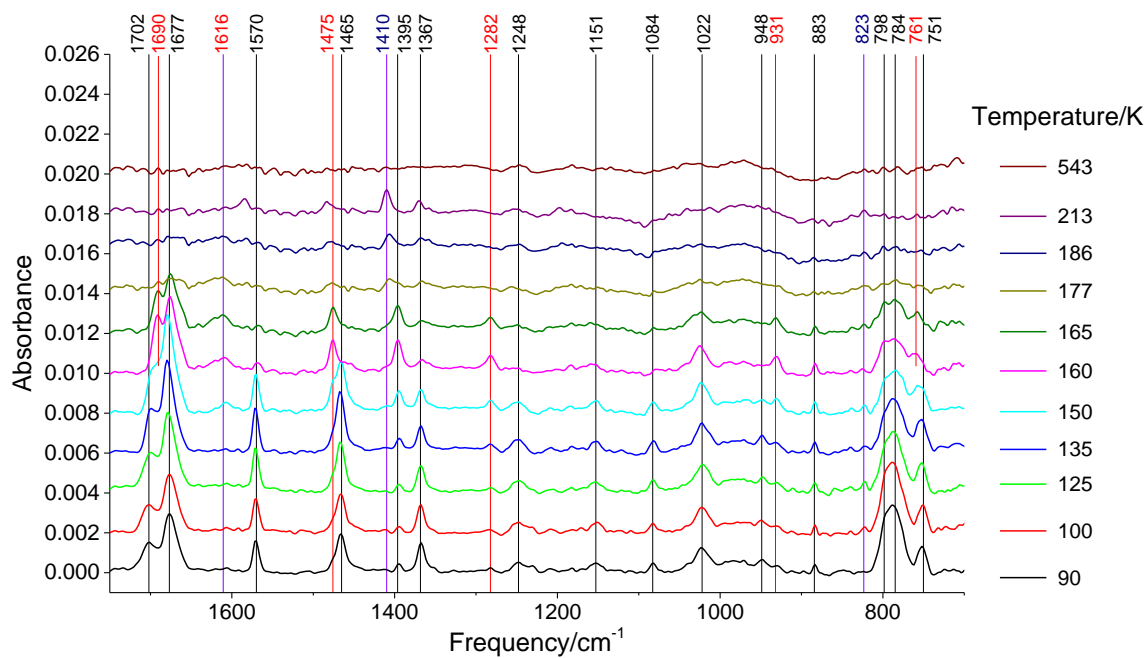
Figure A1.12: Infrared spectra of furfural (using a 1 L exposure from Fig. A1.3) adsorbed on Pd(111) at ~90 K as a function of annealing temperature, where the annealing temperatures are indicated on the figure.

The general behavior of the surface-chemistry of furfural on Pd(111) is evident from the data shown in Fig. A1.12, and shows that furfural is tilted with respect to the surface following adsorption at ~90 K, with the aldehyde group remote from the surface (the Tilted 2 species of Vlachos).[97] When annealing, the tilt angle of the upright species increases up to a temperature of 150 K, similar to the molecular reorientation observed in the case of the thick multilayer (A1.6). Further annealing produces a decrease in intensity of the in-plane ring signals, which translates into a decrease of tilt angle, as well as a small amount of desorption. This restructuring is summarized in the infrared spectra displayed in Figure A1.13, where the overlaid infrared spectra collected at three key temperatures, 90, 150 and 165 K (as green, blue and red shaded curves

respectively) show how signals of the cis conformation increase with increasing temperature, while the opposite trend is observed for the case of the trans conformation.
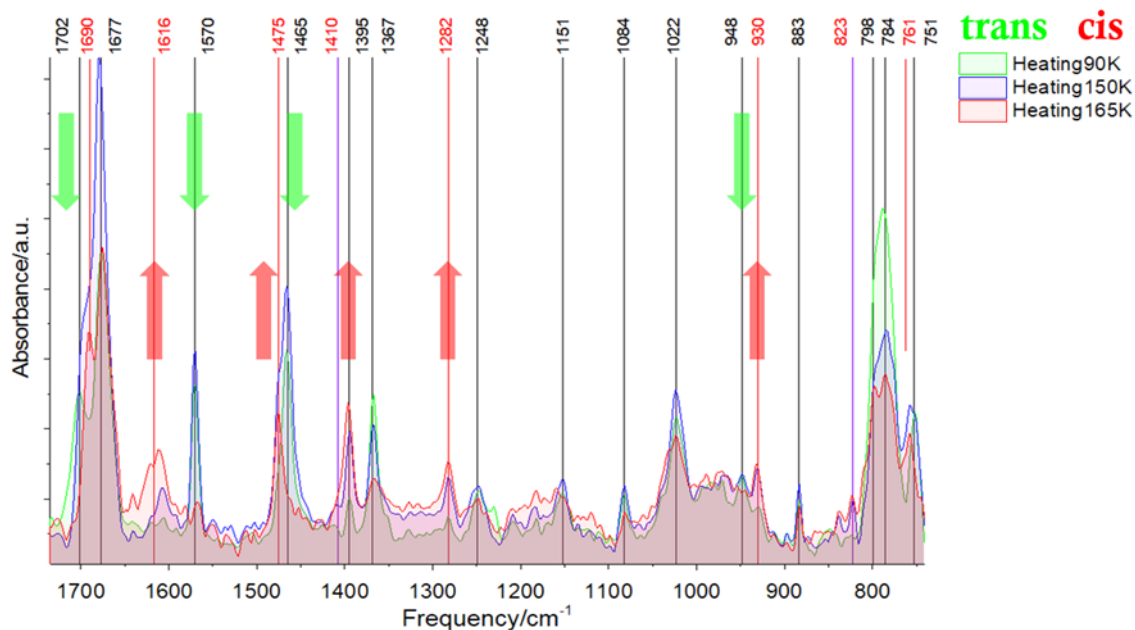
Figure A1.13: Infrared spectra collected at three key temperatures, adapted from Fig. A1.11, which are overlapped to illustrate the trans to cis transition after annealing.

A1.4 Conclusions

Molecular furfural undergoes several structural and conformational transformations on Pd(111) depending on the temperature and surface coverage, or whether it is present as a molecular overlayer or a condensed multilayer. The carbonyl stretching modes for the tilted form of furfural on Pd(111) at low temperature are close to those found for a condensed layer of furfural (Fig. A1.6), indicating that the aldehyde group of the tilted form of furfural is remote from the surface upon adsorption. Heating the overlayer formed at ~90 K initially causes it to become more perpendicular to the surface (Figures A1.5 and A1.6). These conformational changes suggest that furfural crystallizes into a phase favoring the cis conformer (Figures A1.7 and A1.8) but further heating to higher temperatures (to ~180 K) causes the infrared signal of the tilted form of furfural

to decrease significantly in intensity, presumably due to the relief of compression caused by furfural desorption. This produces flat-lying furfural as evidenced by the appearance of the intense out of plane mode observed at 790 cm^{-1} and a ~1610 cm^{-1} peak (Fig. A1.9), identical to those initially found at low furfural coverages during the uptake of furfural on Pd(111) at 90 K (Fig. A1.3). The flat-lying species react to eventually form carbon monoxide as evidenced by the intense peaks around 1800 cm^{-1} (Fig. A1.8).[114] This confirms that the flat-lying form of furfural provides the precursor to the decarbonylation of furfural to yield furan, propylene and carbon monoxide [96,97] that is proposed to control the overall catalytic selectivity.[97] This can be tuned by artificially varying the furfural tilt angle by using a strongly bound coadsorbate.[115–118] However the relation between the structural changes in the study of the chemistry is beyond the scope of this work and will discussed detail somewhere else.

Finally, these surface science infrared spectroscopy results provide novel evidence of phase transitions involving important restructuring of furfural and suggest that Pd(111) is sufficiently reactive that could be an alternative used to study the catalytic conversion of furfural to more valuable feedstocks.

Appendix 2: Monte Carlo Simulations of Self-Assembled Organometallic One-dimensional Wires

A2.1 Introduction

Understanding how single molecules self-organize into conductive architectures at the sub-nanometer scale is crucial for the development of new technologies using the long-overdue "bottom-up" approach for molecular electronics. Within the next few years, limitations of the size of objects that can be manipulated (or etched) in a reliable and industrially viable manner, for the fabrication of integrated electronic circuits, will be reached and completely new ways of approaching their fabrication will be required.[119] This was anticipated by Feynman's famous lecture "There is Plenty of Room at the Bottom",[120] when he proposed the idea of constructing electronic circuits by assembling collections of atoms to form functional structures; a so-called "bottom-up", rather than the traditional "top-down", approach. This notion became more concrete with Aviram and Ratner's suggestions for possible molecular architectures that were proposed to act as diodes.[121] Subsequently, a large amount of work has been carried out to measure the electron-transport properties of individual molecules, for example using break junctions or scanning-probe microscopy tips,[122,123] providing a better understanding of the charge-transport behavior at the single molecule level.

Naturally, the next step is the fabrication of such nanoarchitectures. Strategies involving self-assembled monolayers have shown very promising results, such as in the case of Self-Assembled Monolayer Field-Effect Transistors (SAMFETs).[124] However, the more spatially efficient controlled formation of conductive nanoarchitectures within a single monolayer is a much more challenging problem. While scanning probe techniques such as scanning tunneling microscopy

(STM) have shown elegantly how the manipulation of individual atoms and molecules is in principle possible, these methods are mostly of academic interest,[125,126] and their translation into industrially relevant processes for mass production of nanoelectronic devices is questionable and unlikely to be capable of efficiently assembling the large number of devices required to fabricate realistic circuits.

An alternative method is explored here, inspired mostly by complex nanoarchitectures found in nature. This consists of creating devices at the nanoscale by allowing the building blocks to self-organize into the desired structures by tuning the environmental conditions [127] on an already pre-patterned substrate. Establishing how such a targeted self-assembly can be achieved to form a specific, desired structure is not trivial and requires a detailed understanding of the self-assembly process and, in turn, of the interactions between all the species involved. The nature of these interactions has been explored in innumerable studies of the self-assembly and self-organization processes.[128–130]

In terms of conductive self-assembled structures, it has been shown that bifunctional molecules with ligands that bind strongly to gold, such as isocyanides and thiols, can spontaneously oligomerize on gold surfaces [131] and are also capable of forming conductive bridges between gold nanoelectrodes on an insulating mica substrate.[132] The structure of organometallic wires made from 1,4-phenylenediisocyanide (PDI) and Au adatoms consisting of (-Au-PDI-)$_n$ chains was previously imaged by STM down to the atomic scale, where it could be seen that the distance between individual monomeric (Au-PDI-) units is 1.1 nm.[131,133] This type of self-assembly chemistry offers the possibility of interconnecting between gold nanoelectrodes. Furthermore, based on an analysis of the self-assembly mechanism,[134] it was suggested that dipolar analogs of

these molecules could be aligned by the imposition of an external electric field between nanoelectrodes.

An interesting twist in the approach proposed here to the self-assembly of circuits is to make use of current top-down nanofabrication techniques, which allow the preparation of features with sizes in the order of 10 nm, to produce judiciously tuned nanoelectrodes. These will act as guiding and anchoring points for the directed self-organization of interconnections between them, leading to fabricating devices with complex electronic and structural functions.

Based on the linear self-assembly mechanism discussed above, a simplified model was explored using Monte Carlo simulations and the lattice-gas model in order to examine the outcome structures as a function of various parameters that influence the evolution of the nanoarchitecture. These parameters are, *(a)* the interaction energy "*w*" between the entities involved in the process, *(b)* the coverage θ of monomeric units, i.e.: the "building blocks", *(c)* distance "*m*" between nucleation sites, *(d)* temperature and *(e)* time elapsed from the deposition of the precursor molecules on the surface. Understanding the influence of these parameters in the resulting structure will aid the future design of nano-architectures produced by directed self-assembly. Note that we have chosen to use the stochastic approach provided by Monte Carlo simulations to address the self-assembly, to mimic the way nature carries out this process.

While the original approach was useful and provided very valuable insights into the self-assembly, increasing the complexity of the systems to mimic more realistic ones resulted in prohibitely expensive computational times. In this appendix, improvements to the way the calculations are performed are described. These improvements include: (1) parallel runs of individual conditions and averaging of the resulting outputs, (2) adaptation to run on computer clusters and specifically on the Open Science Grid platform (OSG),[135,136] which is supported by the National Science

Foundation award 1148698, and the U.S. Department of Energy's Office of Science, (3) generation of periodic backups at checkpointing for resubmission in the case a calculation is unexpectedly interrupted, (4) proposing automation of protocols by using adequate scripts and Directed Acyclic Graph manager (DAGman).[137] This will ultimately serve to decrease the computational limitation of the original calculations, enabling expansion of our model to more complicated (realistic) systems and potentially add a third dimension to simulate 3D systems such as solids, liquids, gases and interfaces.

In the following sections more realistic scenarios by adding system parameters not originally considered will be discussed, including: (1) nearest neighbor diffusion, (2) introduction of monomers as a function of computational time (variable dosing conditions), (3) improved percolation analysis, (4) chain-length distribution statistics, (5) controlled distribution and size of ideal nanoparticle arrays, (6) input of architectures from images of real systems. All these modifications contribute to providing a more realistic picture of the experimental systems. This is particularly useful for the experimental case in which a top-down approach is first used to synthesize an array of nanoparticles and a bottom-up approach is later used to link the nanoparticles. This improved simulation scheme was used to study self-assembly strategies for designing molecular electronic circuits.[138] The application of the new simulation scheme was an important collaboration project which was part of the graduate research work by Dr. Dustin Olson. In that work, Dr. Olson considered different types of adsorbed species in the model and run the calculations, generating output statistics that allowed important conclusions on the mechanism and growth kinetics. These simulation results were in good agreement with experimental data from actual devices we designed and built using state of the art in top-down nanolithography JEOL JBX6300 electron beam writer at the Center for Functional Nanomaterials (CFN), Brookhaven

National Laboratory under proposal number 34136, in collaboration with Dr. Aaron Stain and Jorge A. Boscoboinik.[139] The versatility of the model encouraged the creation of a plan for providing public access to an organized repository of the code. The open-access repositories will promote further improvements and consolidation of teams that will benefit from the power of this resource in which the limitation experienced at the moment is the lack of human resources to analyze the amount of data that can be generated over time, which could easily surpass a single person's capability of data manipulation and analysis. The teams could be focusing in different facets of the scaling of the project such as (a) design of projects, (b) management of data, (c) interpretation, (d) incorporation of machine learning, (e) implementing user friendly graphic interfaces, (f) scaling, etc. To give a sense of the power of the scaling in the improved simulation scheme, using resources such as OSG, the reproduction of years of initial calculations have taken approximately three days in spite of increased sampling (improved statistics), and added complexity in the calculation.

A2.2 Monte Carlo Simulations Model

The model proposed here is inspired by the experimental system of the formation of $(PDI-Au)_n$ oligomers on Au(111). However, it is applicable to directed self-assembly in general, allowing fundamental studies of a variety of experimental systems. To aid in describing this general model in a simple and clear way, restrictions have been imposed on the model that, to some extent, differ from the experimental system. Nevertheless, as it will be shown from the results, many of the features arising from the simulation do indeed mimic those seen experimentally.
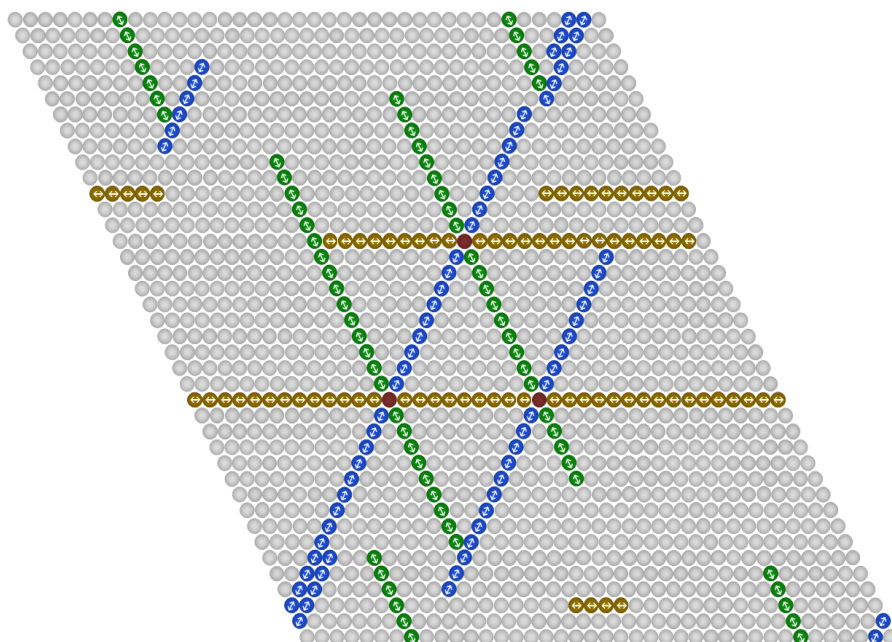
Figure A2.1: Schematic diagram of a 40 × 40 triangular lattice with periodic boundary conditions for a coverage θ ≈ 0.12 of monomeric units. The blue, green and yellow circles represent monomeric units aligned along the three lattice directions, as shown by the arrows. The gray circles are the empty sites in the lattice, and the red circles represent the fixed particles taking the role of nucleation sites.

We use a lattice gas model, where the surface is represented by an array of N = L × L sites in a triangular lattice arrangement (see Figure A2.1), analogous to the arrangement of surface atoms on Au(111), where L is the linear size of the array. Periodic boundary conditions are imposed to represent an infinitely large system. Each site can be occupied by a monomeric unit of the molecular wire, where the monomeric unit is also given a value of an alignment parameter corresponding to one of the three surface directions, analogous to the (Au-PDI) monomeric unit. Note here the first difference between the simplified model and the experimental system. In the model, each monomeric unit occupies a single site in the triangular lattice while in the experimental case, each (Au-PDI) unit extends linearly, thus occupying four unit cells on the Au(111) surface.[131] The preferred lattice direction of the monomers in the model is described by attractive interaction energies in one of the three lattice directions, as given by the alignment parameter. The direction

95

of the interaction energy is shown by a double arrow in the representation of the monomeric units in Figure A2.1. As previously reported,[140] under certain circumstances, this linear interaction can induce the self-alignment of the monomers into chains on the surface, similar to the experiment case, when the interaction energies are similar to those in the experimental system. It was seen for the (Au-PDI) system that low-coordination sites, such as step edges, dislocations, kinks or island edges on the surface can act as nucleation sites from which the molecular wires grow. It was also already suggested in the first experimental report of this system that this fact could be exploited by patterning the surface with defects (low-coordination sites) to act as nodal points for the self-assembly of nano-architectures.[131] There is already direct experimental evidence of this,[139] and a conductivity study of a mica surface covered by gold nanoparticles shows that the latter are in electrical contact upon adsorption of PDI, as a result of the formation of (Au-PDI)$_n$ wires linking them.[132] We further elaborate here on this idea by arbitrarily postulating an initial structure of the particles fixed in place on the triangular lattice. These particles play the role of nucleation sites for the growth of wires, and interact with the mobile monomeric units in any of the three lattice directions, analogous to what was observed for gold islands on the Au(111) surface. Figure A2.2 shows an example of an experimental result, imaged by STM, in which gold islands connected by molecular wires are seen in the image.
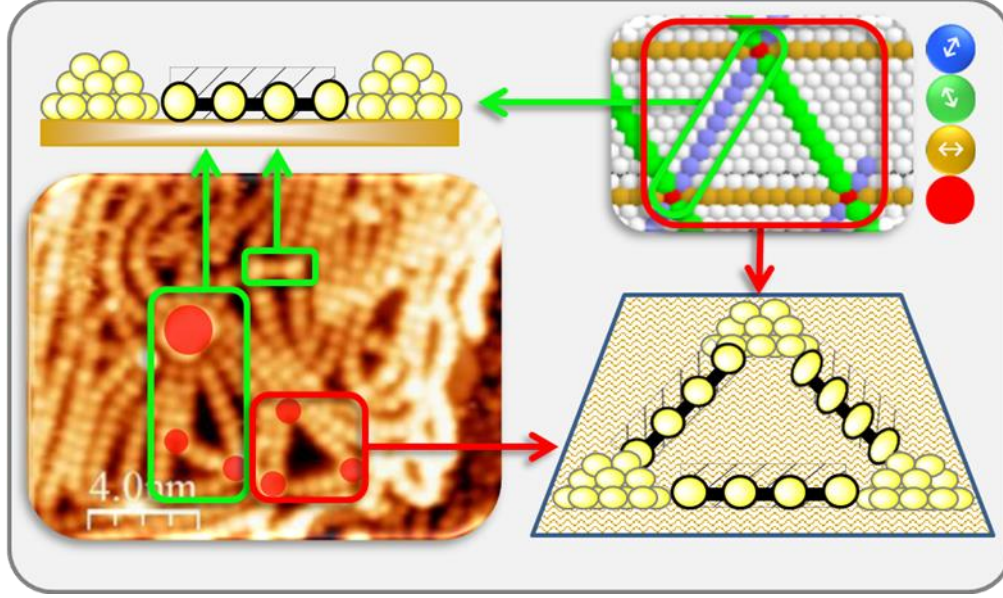
Figure A2.2: STM image of (Au-PDI) wires on Au(111). Nodal points where the (Au-PDI)n wires originate from are emphasized by red circles. Imaging conditions: It = 206 pA, Vb = -2 V. At the top right corner a schematic representation of the simulated system is shown where the blue, green and brown circles represent directional monomeric units aligned along the three lattice directions, as shown by the double arrows. The white circles are the empty sites in the lattice and the red circles represent the fixed particles taking the role of nucleation sites.

In the following, fixed, low-coordination growth nucleation sites will be referred to as "nodes" or "nodal points" or "nucleating sites". As reported,[140] the nodes have a remarkable influence on the resulting self-assembled structures. In our model, the interaction of nodal points with Au-PDI monomers is considered to be attractive and to occur only in the direction of the axis determined by an alignment parameter of the monomer, (see Figure A2.1-2). Then, the adsorbed phase, in the canonical ensemble (at a given coverage), is characterized by the following Hamiltonian:

$$H = -w \sum_{\langle i,j \rangle} \text{int}\{|\vec{r}_{ij} \cdot \vec{s}_j||\vec{r}_{ji} \cdot \vec{s}_i|(1-c_i)(1-c_j)\} - w \sum_{\langle i,j \rangle} [\text{int}\{|\vec{r}_{ij} \cdot \vec{s}_j|(1-c_j)c_i\} + \text{int}\{|\vec{r}_{ji} \cdot \vec{s}_i|(1-c_i)c_j\}] \quad (A2.1)$$

Here, the sums are over pairs $\langle i, j \rangle$ of nearest-neighbor (NN) sites; the occupation of one site by the Au-PDI monomer is described by the vector $\vec{s}_i = \{0, \vec{x}_k\}$, which takes the value "0" if the site is empty, and $\vec{x}_k$ it is it occupied, giving as well the orientation of the monomer in one of the "k"

directions of the lattice; $\vec{r}_{ij}$ is the vector connecting site "i" with site "j"; the node occupation variable is given by, $c_i = 0, 1$, where c_i takes the value "0" when the site does not have a nodal point; w represents the lateral interaction between two adsorbed monomers located in two NN sites or the lateral interaction between a monomer and a NN node. In this model the interaction between nodes is not considered. A study with a more general model including this and other interaction terms is in progress. Thus, the first term on the right-hand side of eq.(1) represents the contribution to the Hamiltonian corresponding to particles located at sites i and j, which are nearest neighbors; sites may or may not be occupied by monomers which have orientations given by $\vec{s}_i$ and $\vec{s}_j$; monomers contribute with energy w, if and only if both are oriented in the direction of the vector connecting the two sites $\vec{r}_{ij}$ or $\vec{r}_{ji}$; the final contribution is 0 or 1, due to the function "int", which take the integer part of this factor. Finally, the factor $(1 - c_i)(1 - c_j)$ avoids the presence of nodal points at both "i" and "j" sites.

The second term represents the contribution to the Hamiltonian due to a monomer located at site j (i) and a nodal point located at site i (j). Note that, in the absence of nodes the model is the well-known rigid-rod model, which has been extensively studied by others. For more details on the self-assembled rigid rod model, see ref.[141] and references therein.

Monte Carlo Method

The thermodynamic properties of the present model have been investigated by means of a standard-importance-sampling Monte Carlo method in the canonical ensemble. As mentioned above, the simulation lattice is a triangular array of $N = L \times L$ sites with conventional periodic boundary conditions. Thermodynamic equilibrium is obtained by following the Kawasaki dynamic.[142] As an initial configuration, a fixed number of nodes can be located at random or in a

regular array (in what follows, only regular arrays can be considered); then, a fixed number of adsorbed monomer units is distributed on the empty surface sites, to reach a predefined coverage θ, defined as the ratio between the number of adsorbed monomers and the total number of surface sites N). The location and orientation of the monomers are taken at random. Then the system is allowed to reorganize itself based on the following rules. First, one of two possible events, migration or rotation, is chosen at random. For a migration event, an occupied site and an empty site are selected randomly, establishing its coordinates; they are not necessarily NN sites. Then, the difference between the energies of the final and initial states, $\Delta E = E_f - E_i$, is calculated; a random number ξ uniformly distributed in the interval $(0 \leq \xi \leq 1)$ is chosen, and compared with a probability $P = \min [1, \exp (- \beta \Delta E)]$ where is $\beta = 1 / k_B T$ (k_B is the Boltzmann constant); an exchange between the occupation of the sites is carried out if $P > \xi$, i.e.: if the probability P is larger than the random number ξ.

For monomer rotation, the rotational state of the selected monomer is changed following the same procedure described above. A final rotation state is considered, and the energy of the monomer is calculated. Finally, the energy change between the initial and final rotated states is computed. The new rotated state is accepted after considering the comparison between a random number and the probability as described above.

A Monte Carlo step (MCs) is defined as $N = L \times L$ attempts to change the state of occupation and rotation of a surface site. Typically, the equilibrium state is reached after 1×10^5 MCs, as will be shown later. In order to simplify the comparison of interaction energies, we will assume a temperature of 298 K. However, it should be noted that, given the $\Delta E/k_B T$ term in the probability equation, when discussing changes in energy, this would be equivalent to inverse changes in temperature. Note that a dimensionless parameter could have been used instead to make the model

more general. In fact, this dimensionless parameter can still be obtained by multiplying the stated energies throughout the manuscript by $k_B * 298$ K if a more general term is needed.

A2.2.1 Nearest-Neighbor Diffusion

The self-assembly process in the model previously introduced has no restrictions on the position which a monomer can move, namely, monomers can go to any empty site on the surface in a single step, even "jumping" over occupied sites. This is equivalent to a case in which monomers can desorb and immediately re-adsorb at other empty site. From now on this regime will be referred to as "random diffusion". These published results lead to equilibrium conditions that are thermodynamically stable, but they provide no insights into the kinetics of the phenomena, which does occur through on-surface diffusion for the experimental case study that originally inspired these simulations. We will consider next the mobile monomers that can only diffuse to nearest-neighbor sites, since this could be a more realistic scenario. In addition to providing information on the kinetics of the process, the restriction to nearest-neighbor diffusion can also give useful information about kinetically trapped states that are not considered by the random diffusion model. At this point, we will add the nearest-neighbor diffusion while keeping all other parameters equal to those described in the previous section, whose results are included in more detail in a prior publication.[140] We start by defining a lattice of 40×40 sites. To analyze the nano-scale self-assembly of molecular wires directed by nodal points, an "elementary circuit unit" (ECU) is defined as a geometrical shape given by a regular arrangement of nodal points located at the vertices of such shape, i.e. for a triangular lattice, it can be a triangle or a square or rectangle for a square lattice, etc. That is an arbitrary definition, but it is necessary in order to derive the equilibrium properties of the system determined by the location of the nodal points. For example, a triangle in which the nodes are ten lattice units apart will be designated ECU_{10}. Figure A2.1

100

shows an example of a 40×40 triangular lattice with ECU_{10} and monomers on the surface aligned along three different directions denoted by different colors and arrows. The gray circles represent empty sites and the red circles are the fixed particles that act as nucleation sites.

Note that each full simulation includes a large number of simulated experiments, from whose totality statistics are extracted. The assembly probability PA is defined as the number of simulated experiments that result in the formation of an ECU, divided by the total number of simulated experiments for a given coverage. Here the coverage θ is defined as the total number of monomers plus nodal points divided by the total number of lattice sites.

At this point, we emphasize the importance of large-scale, parallel computing platforms such as the open science grid (OSG) can greatly improve the efficiency of the calculation. After testing nearest-neighbor diffusion models, a number of systems with conditions similar to those published previously [140] were successfully executed using the OSG resources. Figure A2.3 shows example results of nearest-neighbor diffusion, where the assembly probability PA of an ECU_4 is plotted as a function of time (in MC steps) for various coverages using a lattice with dimension $L = 40$. It can be seen in this plot that the system has already reached equilibrium after 10^5 MCSs.
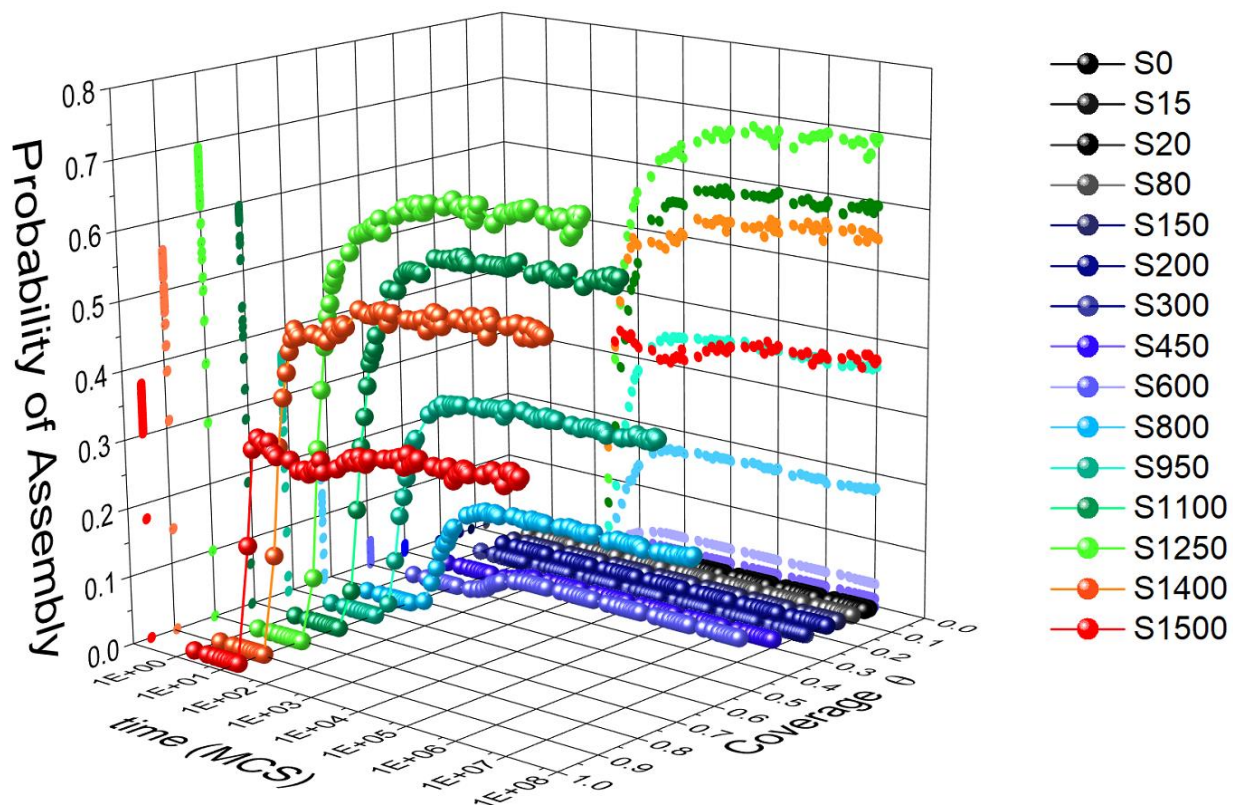
Figure A2.3: Probability of assembly for an elementary circuit unit with nodal points 4 sites apart from each other at the center of a system of size L × L = 40 × 40 sites as a function of computational time (MCS), interaction energy $w = 124$ kJ/mol for various initial monomer coverages (θ) averaged over 1×10^7 results of independent parallel runs. This calculation was run on using Open Science Grid resources. In the legend, the coverages are listed as the number of monomers in excess of those required to form the elementary circuit unit.

The use of large-scale, parallel computing resources such as the OSG is essential to run these calculations and it would not be possible to implement a project like this one in a timely fashion with any other resource. To illustrate the importance of parallelization, the analogous published calculations [140] (with simulations running sequentially rather than in parallel) would have taken at least one year. In section A2.2.5, we present an ongoing protocol to automate the submission and data collection (processing and transfer) for use in future projects. These results show that nearest-neighbor diffusion significantly decreases the probability of assembly when compared to the case of random diffusion (illustrated here for interaction energies of $w = 124$ kJ/mol). When only nearest-neighbor diffusion is allowed, the system is often unable to access the thermodynamically

most stable state energy and becomes trapped in a local minima. This can occur, for example, when reaching this thermodynamically stable state requires monomers to jump over occupied states (possible for the random diffusion case, but not with only nearest-neighbor diffusion). This also results in a lower probability of assembly of the elementary circuit units. However, if w is reduced (either by a decrease in interaction energy or an increase in temperature), the system does reach states of organized longer-range structures. This, in turn, increases the probability of assembling elementary circuit units with nodal points up to 20 monomers apart. An example is shown in Figure A2.4, which shows a snapshot a calculation with $w = 6$ kJ/mol and L = 40.
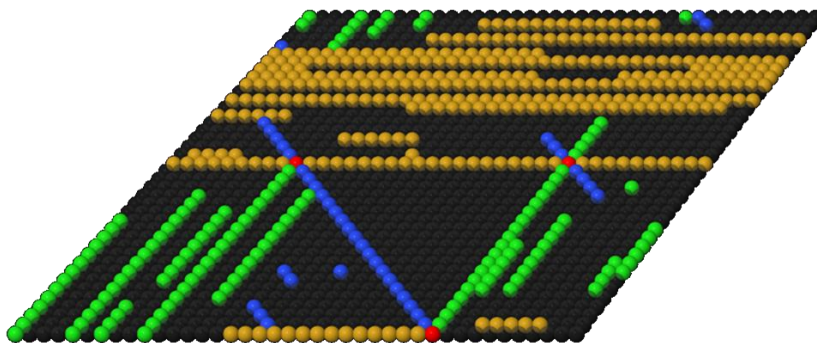
Figure A2.4: Snapshot of an assembled elementary circuit unit with nodal points 20 sites apart from each other at the center of a system of size L × L = 40 × 40 sites. The state was achieved at an interaction energy "w" = 6 kJ/mol. The probability of forming this structure was virtually zero for any other w values analyzed, which means that we might have, for nearest neighbor diffusion, different ideal conditions with regards to protocols for designing molecular architectures than the case of random diffusion.

Some basic guiding principles have been obtained for modeling the self-assembly of an ECU. These are applicable to case of nearest-neighbors diffusion and are:

i) when the exact number of monomeric units to form the ECU is present, the probability of actually assembling the ECU is virtually zero,

ii) there is an optimum range of coverages where the probability of assembling the ECU is maximum, and

iii) the circuit probability of assembly decreases at high coverages, most likely due to "crowding" effects.

The assembly of a "circuit", defined as a network of ECUs, was previously discussed to introduce the proposed methodology for a simple case that make use of the already defined ECU without involving more complex architectures found in a conventional electronic circuit. The circuits were referred to as controlled electrical connections between two sides of a surface, representing two electrodes, for instance, making use of the self-assembly of molecular wires guided by an arrangement of nucleation sites (nodal points) on the surface. Results of these simulated networks of elementary circuit units are shown as the probability of assembly as a function of computational time and coverage in Figure A2.5 for a nodal distance of 5 monomers (calculation run using OSG resources). As previously mentioned, a more detailed analysis of these results is beyond the scope of this work and will be discussed elsewhere.

Despite its simplicity, it is of great interest to analyze this process so we can define the fundamental concepts that will aid the design of complex self-assemblies in the future. For example, in work by Kestell and coworkers, it was shown that $(Au\text{-}PDI)_n$ chains, which connect islands of gold atoms on a mica substrate, are good electrical conductors.[132] Furthermore, it was also shown that the $(Au\text{-}PDI)_n$ junctions could be switched off when they interact with certain molecules, such as CO. This has important implications for different applications, since the interconnecting of molecules can be considered as molecular "switches" that respond to chemical changes in the environment, such as the presence of a specific gas.[143] These features are of particular interest from the practical point of view, as these switches could be used as very sensitive gas detectors.
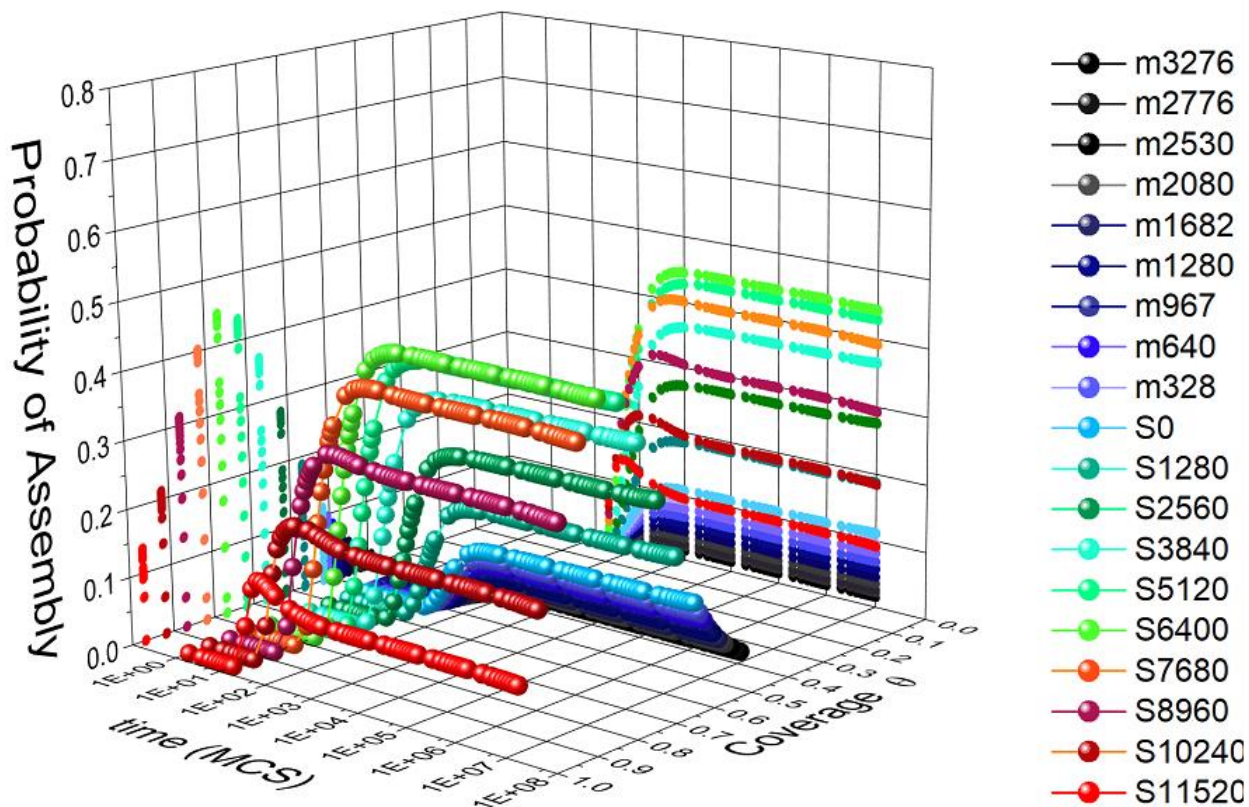
Figure A2.5: Probability of circuit assembly as a function of computational time and coverage. Simulation of the formation of the network of triangles with a nodal distance of 5 monomers, system size L × L = 160 × 160, w = 124 kJ/mol.

A2.2.2 Introduction of Monomers Over Time (Dosage)

An alternative strategy for the assembly of nano architectures, such as the elementary circuit units (ECUs) described before, is through the progressive dosing of the monomeric units. That is, the introduction of monomeric units happens progressively, allowing surface diffusion while the coverage is increasing. The Monte Carlo simulations allow the way this occur to be mimicked. In contrast with previous simulations, in this case, the lattice is initiated with only fixed nucleating sites. For the case of an ECU, three nucleating sites are present at the vertices of an equilateral triangle. In the case described here, a triangular lattice of size 60 × 60 with periodic boundary

105

conditions is utilized. First, we define the coverage of monomeric units to be introduced and the rate at which this changes. After each monomeric unit is added to the system, the previously adsorbed monomers are allowed to diffuse, rotate, or to remain unchanged. It is necessary to stress that the time is measured in Monte Carlo steps (MCS), where 1 MCS is defined as a number of event attempts equal to the number of sites on the lattice. Similar to previous calculations, the results are statistically averaged over independent simulated experiments (samples) carried out under the same conditions. This allows us to obtain the probability of assembly of a particular architecture. If each nucleation site is separated by, for instance, ten lattice units (ECU_{10}), then at least 27 monomeric units are needed to form the full architecture. Generally, many more monomeric units than the minimum are required to achieve a significant probability of circuit assembly. The results from the simulations give the optimum coverage needed to maximize the probability of assembling the target nano-architecture as a function of dosing rate, the interaction between monomers and temperature, among other user-defined variables.

In Figures A2.6 (a) and (b), the probability of assembly of the triangular ECU_{10} is shown as a function of time (MCS). This is displayed for two monomer dosing rates, namely at 1 MCS (a) and 100 MCS (b) intervals. The simulation was performed with an attractive interaction of 5 k_BT between monomers, and 20 k_BT between monomers and nucleation sites. For convenience, a dosage unit (DU) is defined as the number of introduced monomers equal to the length of a side of the ECU. It is observed that the time to form the ECU depends strongly on the dosage interval (rate). Other probabilities, such as the assembly of individual sides (complete or partial) of the ECU are also calculated, leading to the possibility of calculating a percentage of assembly of the ECU, as shown in Figure A2.7 for the case of ECU_{10}. More detailed studies are planned by using the more advanced computational resources as described in section A2.2.5.
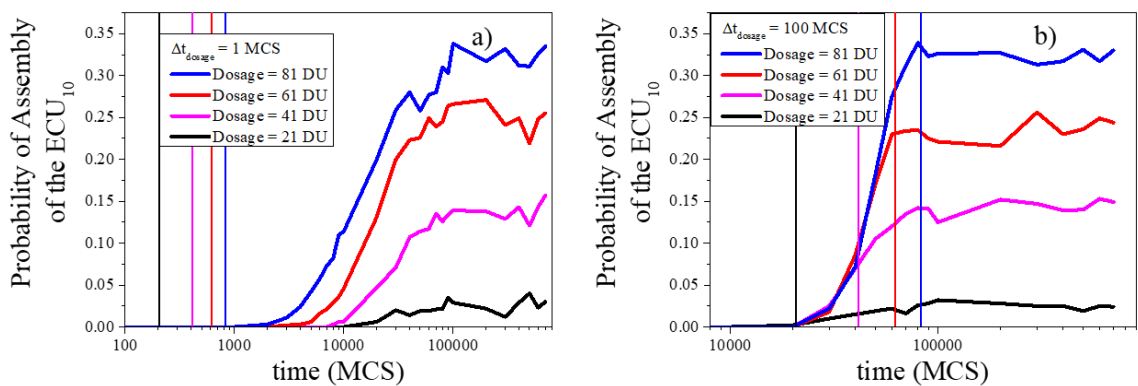
Figure A2.6: Probability of assembly of an entire triangular circuit with nodes being 10 sites apart, at different dosages for a system of $L \times L = 60 \times 60$ averaged results over 1000 samples vs time (in MCS). The dosage time interval is (a) 1 MCS; (b) 100 MCS; with the same color, vertical line denotes when the dosage finish.
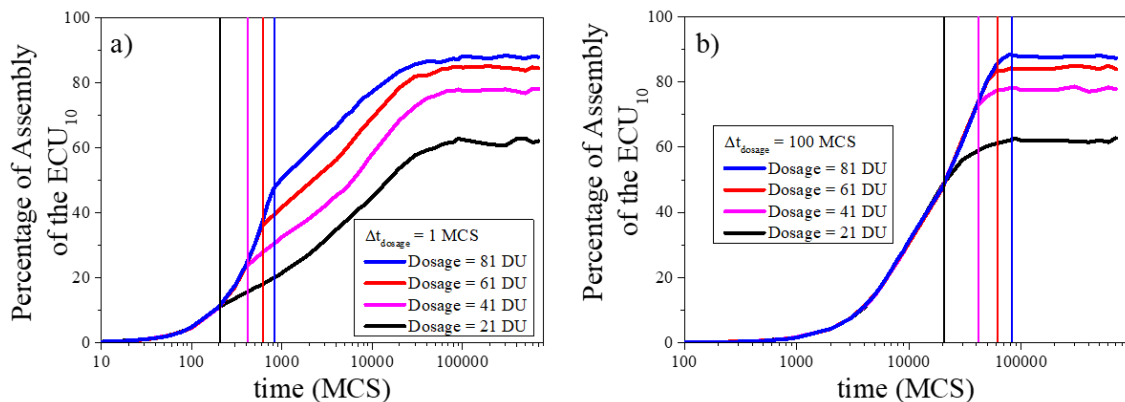
Figure A2.7: Formation percentage of an entire triangular circuit with nodes being 10 sites apart, at different dosages for a system of $L \times L = 60 \times 60$ averaged results over 1000 samples vs time (in MCS). The dosage time interval is (a) 1 MCS; (b) 100 MCS; with the same color, vertical line denotes when the dosage finish.

A2.2.3 Chain Length Distribution

Previous sections clearly show that an excess of monomers significantly above the minimum number required to make an ECU is needed to have a high probability of assembly of the ECU. This is because the monomers can initially nucleate to form structures along different directions, which are not necessarily those that lead to the formation of the desire architecture so that the

107

system must "correct" itself, as previously reported.[140] The approach described here of using Monte Carlo simulations allows the study of any type of surface architecture, from ideal, arbitrarily defined systems to more complex ones generated from digitized images of experimental systems (as will be shown later). This allows the effect of different experimental conditions to be simulated, including the random introduction of mobile monomers at an initial time, or sequentially in time intervals to mimic monomer deposition flux, or other different dosing conditions. The mobile monomers can diffuse or, if they are directional, they can rotate, taking into account the lateral interaction they are subject to. In this manner, it is of importance to analyze the chain length statistics of the system, and how the growth conditions impact its distribution. The Monte Carlo simulations allow the statistical tracking of the evolution of the system, as shown in Figures A2.8 and A2.9. There, the chain length distribution is plotted as a function of computational time. In this simulated experiment, the system evolves, decreasing the number of individual monomers, and increasing chain length as the self-assembly progresses. This information can be utilized to determine the dynamics of chain formation and analyze the equilibrium conditions, including the average length of chains, and potentially promote bridging between contacts or nanoparticles. The latter has been successfully implemented in recent work.[138,139] The data of Figure A2.8 were obtained in a 60×60 triangular lattice, but larger systems will benefit from better computational power.

The versatility of the Monte Carlo simulations allows the analysis of the introduction of nucleation sites at random locations on the lattice, and the study of the impact of the spatial distribution of nucleation sites on the chain length distribution. As in the case of dosage, this analysis requires significant computational resources due to the large number of variables and parameters involved even in this relatively simple model.
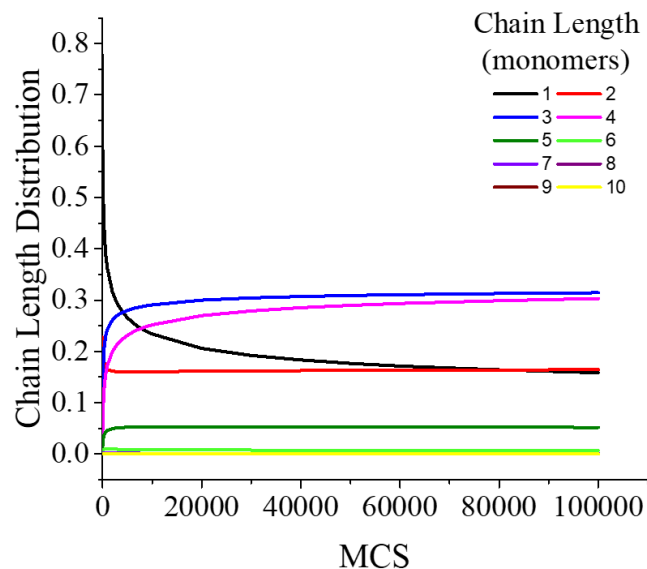
Figure A2.8: Chain length distribution plot as a function of computational time, allowing statistical tracking of the evolution of the system after the random introduction of individual monomers. At the conditions used here, the system evolves to promote self-assembly, decreasing the number of isolated monomers and increasing the size of the chains with time. This improvement can be utilized to see at equilibrium condition what is the average length of chains existing in the system, and potentially promoting bridging between contacts (or nanoparticles).
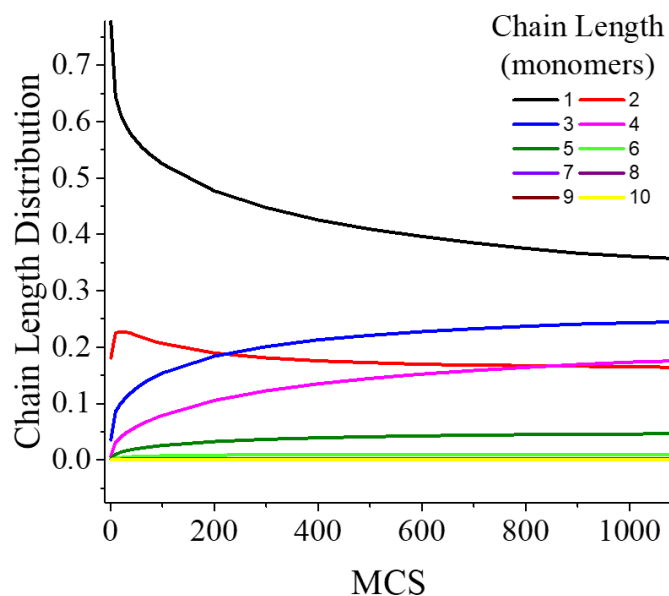
Figure A2.9: Close up view of the first 1000 MCS of Fig. A2.8. The chain length distribution is used here to study the dynamics of the chain growth.

A2.2.4 Information from Real Systems

In collaboration with Dr. Dustin Olson, we prepared devices consisting of gold contacts separated by a few nanometers using electron-beam nanolithography at the Center for Functional Nanomaterials (CFN) at Brookhaven National Laboratory (under CFN proposal number 34136, with assistance from Staff Scientist Aaron Stein and in collaboration Anibal Boscoboinik). These experiments were aimed at studying electronic transport by bridging molecular wires between the gold contacts. After fabrication of the devices, Monte Carlo calculations were carried out in collaboration with Dr. Dustin Olson to reproduce the experimental current-versus-voltage (I/ V) curves. Scanning electron microscopy (SEM) images were provided to identify the distribution of nucleation sites, see Fig. A2.10 (a). By selecting an area of the device, Fig. A2.10 (b), in which the nanoparticle distribution can be captured, the image was transformed into a pixel map (each pixel was rescaled to be equivalent to the size of a monomer site in the calculation). By having this proportionality, an image processing software was used to differentiate the contrast of the areas with nanoparticles, as shown in Fig. A2.10 (c). Finally, the pixel coordinates of the nucleating sites were exported and incorporated in the calculations, Fig. A2.10 (d). A snapshot of a test calculation running in a digitized system is shown in Figure A2.11.
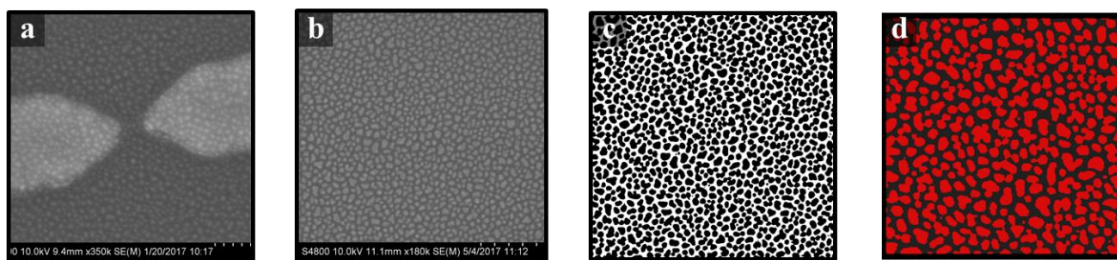
Figure A2.10: Image analysis of real systems for creating a library of particles to input in the calculation. (a) and (b) Scanning electron microscopy images of experimental gold nanoparticle distribution courtesy of Dr. Dustin Olson. (c) image analysis for extracting pixel coordinates of nucleating sites. (d) digitized system.
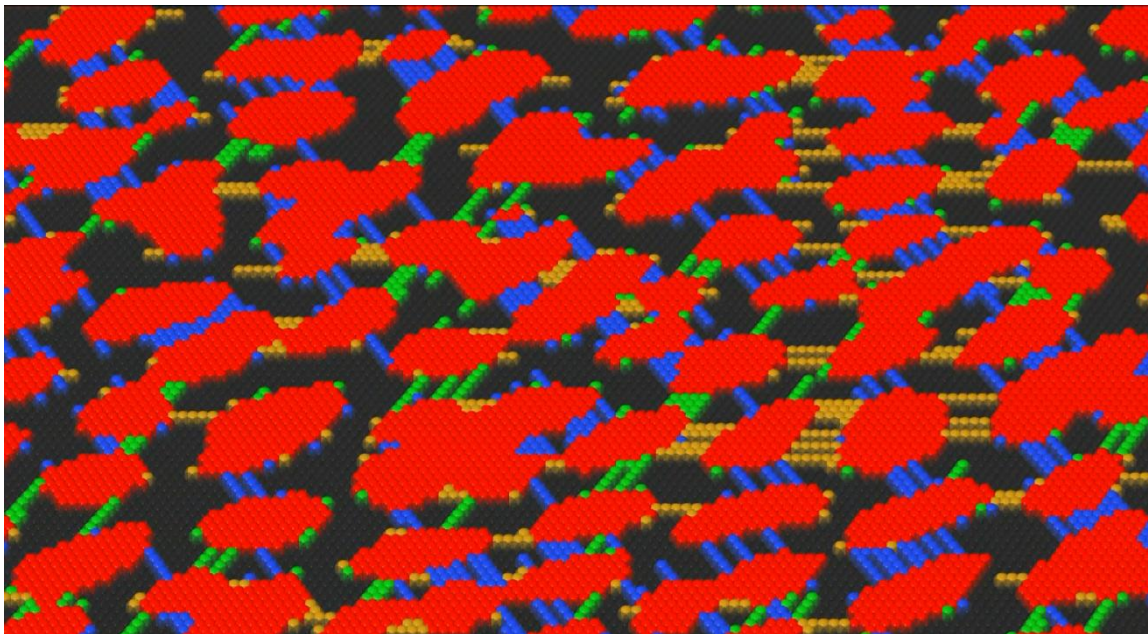
Figure A2.11: Example of a snapshot of a calculation running on a digitized experimental system. Blue, gold and green particles represent directional mobile monomers and red particles are digitized nucleating gold nanoparticles, empty sites are shown in black.

In order to reproduce the experimental IV curves, an improved percolation algorithm was developed. The algorithm consists of a directional search of connected particles (monomers or nucleation sites), rastering from one side of the lattice to the opposite, as depicted in Figure A2.12 top. All connected particles were then computed in a separate matrix in which the coordinates are defined (blue particles in Figure A2.12), and all other particles that do not form part of the percolation paths are also identified from connected and empty sites (red particles). Finally, the percolation matrix can be exported as a function of computational time to get an image representation of the percolation process. Statistics are also obtained for the connected sites percolating from one side to the opposite of the lattice. By tracking the number of connected sites over computational time, a simulated IV curve can be obtained. This percolation algorithm has been already utilized to analyze bridging between particles in a recently published paper.[138]
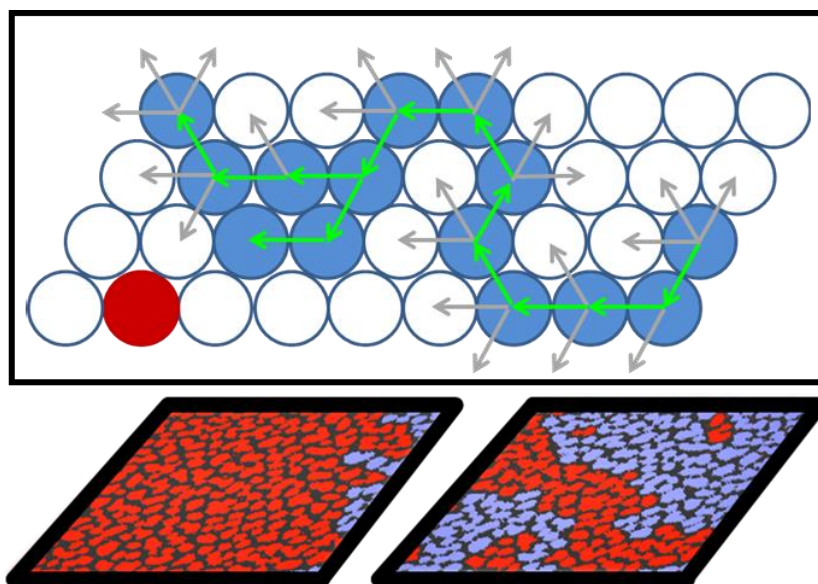
Figure A2.12: Top, a schematic diagram of the percolation algorithm search. Bottom, two Snapshots at two different times of a system to show a graphic representation of results from the improved percolation algorithm. Here, connected (blue) and non-connected structures (red) are showing the percolation from left to right in a system with top and bottom periodic boundary conditions.

A further improvement is the possibility of being able to control the size of hexagonal nanoparticles to form an ideal distribution, as shown in Figure A2.13 top, were a schematic representation is depicted of hexagonal nanoparticles increasing in size from top to bottom. It has been shown that the presence of nucleation sites contributes to the system reaching thermodynamic equilibrium significantly faster.[140] Figure A2.13 bottom shows that the size of the nucleating islands (nanoparticles) also has a substantial impact on the structure of final self-assembled nanoarchitectures. The study of these ideal distributions of hexagonal nanoparticles has been utilized to confirm that (PDI-Au)$_n$ oligomeric chains are capable of bridging gaps up to ~9 nm,[138] and it has been experimentally proven that oligomers can bridge ~5 nm gaps,[139] which is not very different from the predicted value of ~22 nm previously reported [140] using optimal conditions under thermodynamic equilibrium and single-particle nucleating island.
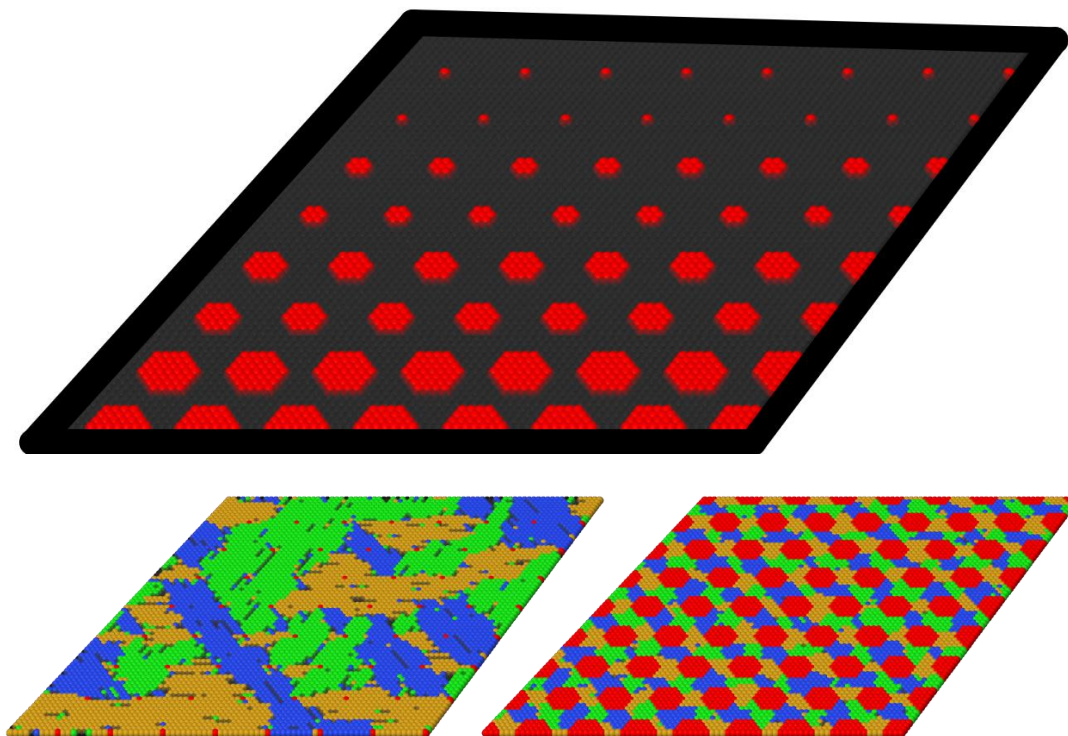
Figure A2.13: Ideal nanoparticle distribution with controlled sizes for studying, for instance, impact in guiding power of self-assembled nanoarchitectures. Top, representation of different hexagonal nanoparticle sizes from single particle to 7 lattice units maximum width. Bottom, impact on guiding power of hexagonal nanoparticle size for a system of 80 × 80 sites with 64 nanoparticles, occupying a single site (left) and seven lattice units max width (right). Interaction energy, w = 124 kJ/mol.

A2.2.5 Scaling Using OSG resources

In order to use the previously developed Monte Carlo code in the OSG platform, it was adapted to run on the Linux operating systems. The performance was also improved with respect to the original Windows version. Figure A2.14 shows that the execution time was halved for equivalent test conditions, using similar hardware. Linux data points are shown in white and Windows results in green for a system with a lattice size of 80×80 with 2000 more monomers than the minimum amount needed to produce a network of ECUs with a nodal distance of 5 monomers (the y axis in this figure is probability of assembly of the entire architecture). The same calculation that took 14 minutes to run on Windows, took only 7 minutes to run on Linux. Snapshots of the system under

examination, taken at the termination point, are shown as the background of the curves. An additional improvement to the code was that the random number generator was substituted to use parameters relative to the execution node in which it will run, which allows the calculations to be executed in parallel, ensuring variability of the needed random numbers. A significant update to the code involves the creation of backup files for checkpointing. This allows long calculations to be run exceeding the run-time limitations of the cluster, and resume the calculations in case of other unexpected interruptions. An example of these updates is shown in Figure A2.15. Here, a calculation creates a backup at 30000 MCS. It is then stopped and re-submitted from that point. Despite the intrinsic statistical variability of being a single average, the calculation continues to operate, demonstrating successful checkpointing. Current work is being carried out to build a management protocol to automate the creation, submission, execution, data retrieval, etc.
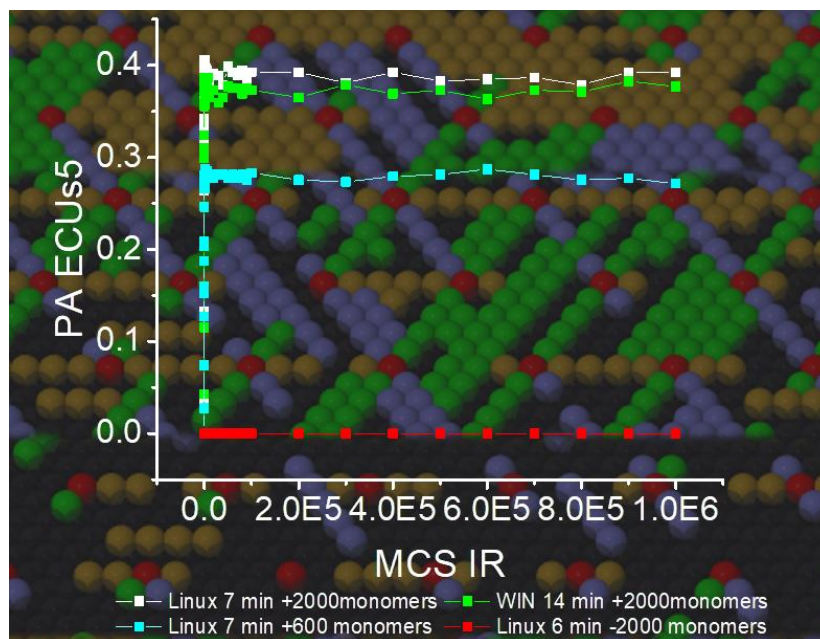
Figure A2.14: Comparison of the same calculation run Windows and Linux Operative System (OS). The time needed for different coverage conditions is shown. For the case in which the coverage is such that there coverage of 2000 monomer above those required to from the network of ECU_5 (80 × 80 sites system dimensions), the same program takes 7 minutes to run on Linux and 14 minutes on Windows. Snapshots of the systems after included as background for illustrating the three different coverages in monomers referenced to the minimum number to needed to form the network of ECU_5 (+2000, +600, -2000). The case of -2000 reflects a total number of monomers below that needed to form the network of ECUs.

114
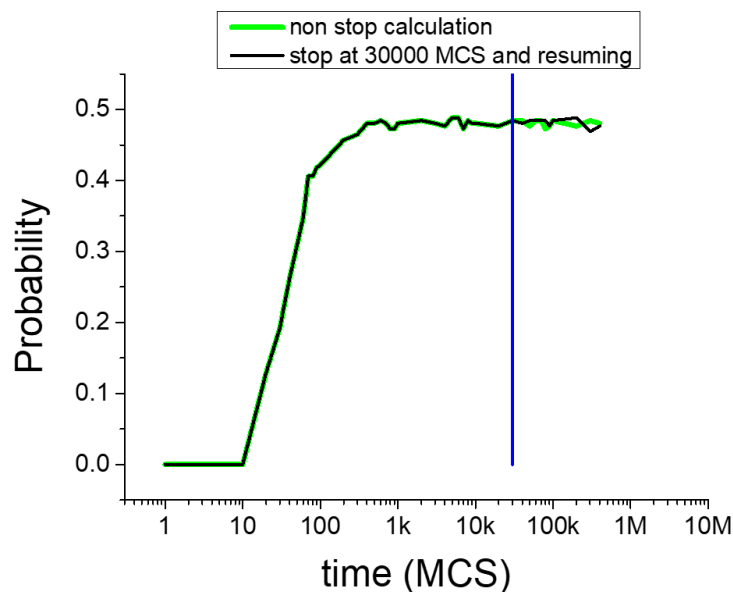
Figure A2.15: Checkpointing test for scaling at OSG. The calculation backup was saved at 30 kMCS (blue line) and successfully executed when resubmitted (black). Differences with original nonstop calculation (green) are related to the seed on the random number generated, and it is statistically correct to observe this slight variation. Calculation conditions for this test were: System size $L \times L = 80 \times 80$ sites and 3328 monomers to form the circuit of array elementary circuit units. Node separation 5 sites.

The Open Science Grid (OSG) planned workflow is described in Figure A2.16. Here, the use of Directed Acyclic Graph manager (DAGman) [137] is proposed to manage the modular organization of the workflow. The objective is to automatically submit jobs in a particular order and automating the calculation setup and data processing. In this way, a single generic master file (denoted as "*.cpp" in the diagram) is then subject to a sequence of scripts. The first produces a tree of properly organized calculations with parameters listed in a "parameter file". A second script acting on these calculations manages the submission from the "submit node" to the "execution node", where the calculations run. A backup file is periodically generated, and partial results are transferred back to control the evolution of the calculation. Each time a calculation is successfully terminated, the final result is retrieved and averaged with the previous ones. This is repeated until all calculations have terminated. The final results are now ready for analysis. The DAGman works by modifying the master calculation to submit, in parallel, as many averages as desired. This automation will

significantly reduce the workload and assist with data processing. To manage parallel analogous workflows while testing other architectures (for example, distributions of nucleating sites), SPLICE [137] can be used. A splice could be used to designate different architectures, which will then be managed by following the DAG management protocol described previously. The latter is extremely powerful and by having, for instance, different distribution of nucleating particles defined in the different parameter files, as many conditions as desired could be studied. The revised code can now work in Linux, run on OSG, do parallel execution, run scripts for automated job submission averaging results, and do checkpointing. We are now ready to generate the management protocols using DAGman and SPLICE DAGman. The final step will be the release of the final code in a repository from where it will be possible to set the conditions and introduce the nodal coordinates. In the longer term, we envision the possibility of the user describing a "target self-assembled nano-architecture" and then running the code to obtain the optimum conditions needed to experimentally achieve such nano-architecture. A further improvement is not to only limit the simulations to surfaces, but to also expand the code to predict the self-assembly of three-dimensional nano-architectures.
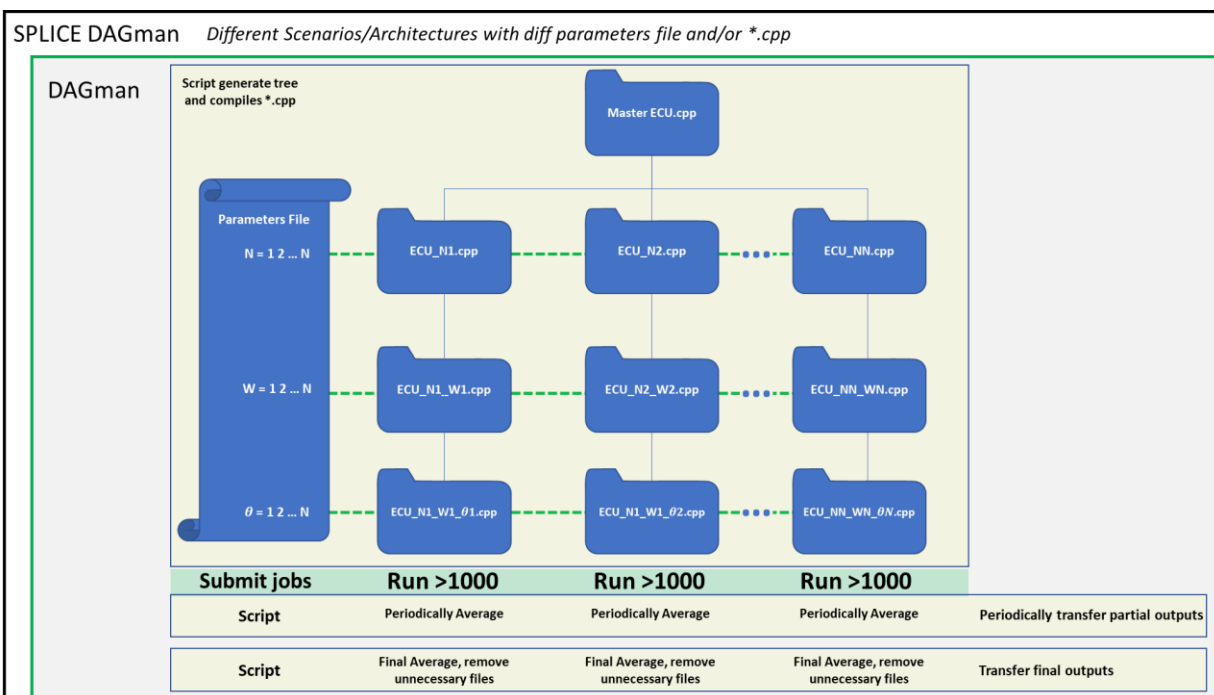
Figure A2.16: General representation of workflow diagram for executing self-assembly calculations at the OSG. Directed Acyclic Graph Manager (DAGman) is used to manage and automate the regular protocol used in this calculations, generate a tree of calculations for each model "*.cpp" to create and organize a variety of parameters/arguments to be tested "tree of calculations" compile them, submit them, report regularly partial results and perform checkpointing to resume calculations if necessary. Finally, report final results and clean unnecessary files.

A2.4 Applications and Future Studies

Current applications of the Monte Carlo simulations described here are the study of the optimum conditions for designing molecular self-assembled architectures [138,140] and perhaps analyzing the reasons for the failure of already designed devices. Hence, a straightforward adaptation of this model makes it versatile to think that there is no limitation to modify it to also work for repulsively interacting particles in two dimensions. However, once the protocol described in Figure A2.14 becomes fully operational, we expect to include a third dimension to contemplate systems such as solids, liquids, gases and interfaces. Finally, by creating open-source repositories with free access, it should be possible to decentralize the power of these calculations and allow the scientific community to contribute to the generalization of applicability of these calculations.

A2.5 Conclusions

The self-assembly of molecular wires, guided by the presence of nucleation units fixed on the surface, was simulated using Monte Carlo methods in the framework of the lattice-gas model. This work is inspired by and compared to experimental data for the self-assembly of Au-PDI units on a Au(111) substrate into long $(Au\text{-}PDI)_n$ oligomeric metal-organic wires. The experimental observation that nanowires are anchored to low-coordination sites (such as surface dislocations, elbows of the herring-bone reconstruction, and edges of gold islands) is represented in the simulations by postulating fixed nucleation units on a triangular lattice at arbitrary locations, and by defining attractive interactions between the mobile monomeric units. In order to facilitate the quantitative measurement of the self-assembly process, three nucleation sites at a distance m unit cells apart were located on the surface to form an equilateral triangle (which is called an "elementary circuit unit" (ECU_m)). A successful ECU is formed when wires self-assemble to connect these three nucleation sites. The probability of formation of the ECU_m was then explored as a function of various parameters including the coverage of monomeric units, the distance m between nucleation sites, the number of Monte Carlo steps, and the interaction energies.

Advances in the simulation methods and scripts were also discussed that enabled the scaling and substantial expansion of the applicability of the model. A workflow scheme for the implementation of these advances is described. These calculations have important implications for the future design of guided, self-assembled molecular-electronic structures, since it allows the optimum values for a variety of design factors to be determined. These factors include the range of coverages of monomeric units that need to be deposited on the surface to ensure electrical continuity and temperature at which the self-assembly process should occur. Finally, the dissemination of the

project and the creation of an open access to the source code is proposed as the final goal in this

road map.

Concluding remarks

While forces are present all around (and inside) us, the fundamental understanding of how they affect the rates of chemical change is very limited. Additionally, there is a lack of awareness about the importance of mechanochemical effects, which is partly related to the scant attention that is devoted to the topic in introductory chemistry textbooks and courses. However, the paucity of information in textbooks could be just traced back to the lack of fundamental knowledge within this field. This work represents a step forward towards remediating some of that gap in knowledge. In the work described in this thesis, the influence of forces on chemical reaction rates was studied at the nanoscale. Using well-defined model systems, we explored the underlying mechanochemical interactions using an atomic force microscope tip to apply a force on a surface covered with methyl thiolates. We analyzed the reaction kinetics of its decomposition under the effect of normal stress. The results are in good agreement with quasi-static first-principles quantum calculations. The thermal activation barrier is obtained by extrapolating the results as the forces tends to zero, and the resulting measured activation barrier is in good agreement with previous studies. Moreover, it is found that change in activation energy as a function of applied stress, scales linearly with the stress-dependent heat of reaction. This suggests that it should be possible to calculate mechanochemical reaction rates by using Evans-Polanyi relations.

Sliding experiments were performed to analyze the influence of the lateral force on the chemical reaction where the imposition of a lateral force results in an increase in the reaction rate. The maximum effect of the shear stress is observed when the lateral force vector is colinear with the minimum energy pathway for diffusion, suggesting that surface diffusion of the adsorbed species plays an important role. The activation volume for the shear-induced process is significant, and it

can be compared to shear activation volumes discussed in the literature for fatty acids in studies on boundary friction.[4]

In order to investigate alternative methods of applying forces and accelerating the rates of chemical reactions, the trapping of noble gases in a nanoporous 2D-aluminosilicate on Ru(0001) was investigated. While useful for fundamental studies, the synthesis of these 2D-aluminosilicates is prohibitively expensive and the amount produced very small for potential practical applications. Taking this into consideration, an alternative synthesis protocol by delamination of a bulk layered material was explored. These aluminosilicates are intended to serve as a playground for studying chemistry in confined spaces, but they can also have important energy applications, including their use in nuclear reactors.

Furthermore, intermolecular forces can promote restructuring on surfaces, and structural changes as a function of coverage and temperature are analyzed for the case of furfural on Pd(111) using infrared reflection absorption spectroscopy. Furfural is a precursor for obtaining more valuable feedstocks, and there is the need for developing catalysts for its chemical conversion with lower toxicity than the ones used at the moment. The results show important restructuring of adsorbed multilayers before chemical reactivity is evident. These conformational changes suggest that furfural crystallizes into a phase favoring the *cis* conformer. This resulting crystalline phase may be related to a long-range hydrogen-bonded network of molecules. The latter will be of interest for studying the influence of furfural molecular ordering in greater detail and providing evidence of temperatures in which chemistry starts to occur on Pd(111).

Finally, a Monte Carlo approach to simulating the self-assembly of nanowires is presented. This approach was later expanded and applied to an experimental system in collaboration with Dr. Dustin Olson (additional work included in his Ph.D. thesis).

References

1. Theophrastus, H. J. Theophrastus's history of stones : with an English version, and critical and philosophical notes, including the modern history of the gems, &c., described by that author, and of many other of the native fossils. *London* (**1774**).

2. Prandtl, L. Ein Gedankenmodell zur kinetischen Theorie der festen Körper. *ZAMM - J. Appl. Math. Mech. / Zeitschrift für Angew. Math. und Mech.* 8, 85–106 (**1928**).

3. Eyring, H. Viscosity, plasticity, and diffusion as examples of absolute reaction rates. *J. Chem. Phys.* 4, 283–291 (**1936**).

4. Spikes, H. Stress-augmented thermal activation: Tribology feels the force. *Friction* 6, (**2018**).

5. Duwez, A. S., Cuenot, S., Jérôme, C., Gabriel, S., Jerome, R., Rapino, S. & Zerbetto, F. Mechanochemistry: Targeted delivery of single molecules. *Nat. Nanotechnol.* 1, 122–125 (**2006**).

6. Konôpka, M., Turanský, R., Reichert, J., Fuchs, H., Marx, D. & Štich, I. Mechanochemistry and thermochemistry are different: Stress-induced strengthening of chemical bonds. *Phys. Rev. Lett.* 100, 115503 (**2008**).

7. Craig, S. L. Mechanochemistry: A tour of force. *Nature* 487, 176–177 (**2012**).

8. James, S. L., Adams, C. J., Bolm, C., Braga, D., Collier, P., Friščic, T., Grepioni, F., Harris, K. D. M., Hyett, G., Jones, W., *et al.* Playing with organic radicals as building blocks for functional molecular materials. *Chem. Soc. Rev.* 41, 413–447 (**2012**).

9. Ribas-Arino, J. & Marx, D. Covalent mechanochemistry: Theoretical concepts and computational tools with applications to molecular nanomechanics. *Chem. Rev.* 112, 5412–5487 (**2012**).

10. Bustamante, C., Chemla, Y. R., Forde, N. R. & Izhaky, D. Mechanical Processes in Biochemistry. *Annu. Rev. Biochem.* 73, 705–748 (**2004**).

11. Brantley, J. N., Bailey, C. B., Wiggins, K. M., Keatinge-Clay, A. T. & Bielawski, C. W. Mechanobiochemistry: Harnessing biomacromolecules for force-responsive materials. *Polym. Chem.* 4, 3916–3928 (**2013**).

12. Sriram, K., Laughlin, J. G., Rangamani, P. & Tartakovsky, D. M. Shear-Induced Nitric Oxide Production by Endothelial Cells. *Biophys. J.* 111, 208–221 (**2016**).

13. Mang, T. & Dresel, W. *Lubricants and Lubrication. Lubricants and Lubrication: Second Edition* (2007). doi:10.1002/9783527610341.

14. Zhang, J. & Spikes, H. On the Mechanism of ZDDP Antiwear Film Formation. *Tribol. Lett.* 63, 1–15 (**2016**).

15. Braun, O. M. & Naumovets, A. G. Nanotribology: Microscopic mechanisms of friction. *Surf. Sci. Rep.* 60, 79–158 (**2006**).

16. Furlong, O. J., Miller, B. P., Li, Z., Walker, J., Burkholder, L. & Tysoe, W. T. The surface chemistry of dimethyl disulfide on copper. *Langmuir* 26, 16375–16380 (**2010**).

17. Bell, G. I. Models for the specific adhesion of cells to cells. *Science (80-.).* 200, 618–627 (**1978**).

18. Boscoboinik, J. A. Small Organic Molecules on Transition Metal Surfaces and Monte Carlo Simulations of Bimetallic Surface Alloys. (Theses and Dissertations, University of Wisconsin Milwaukee, 2010).

19. Becker, W. The turbomolecular pump, its design, operation and theory; calculation of the

pumping speed for various gases and their dependence on the forepump. *Vacuum* 16, 625–632 (**1966**).

20. Henning, J. & Freeman, J. Turbomolecular pumps and their limitations for hydrocarbon-free systems. in *AIP Conference Proceedings* vol. 171 366–375 (AIP, 2008).

21. Gaede, W. Die Diffusion der Gase durch Quecksilberdampf bei niederen Drucken und die Diffusionsluftpumpe. *Ann. Phys.* 351, 357–392 (**1915**).

22. Binnig, G., Quate, C. F. & Gerber, C. Atomic force microscope. *Phys. Rev. Lett.* 56, 930–933 (**1986**).

23. Mate, C. M., McClelland, G. M., Erlandsson, R. & Chiang, S. Atomic-scale friction of a tungsten tip on a graphite surface. *Phys. Rev. Lett.* 59, 1942–1945 (**1987**).

24. UHV 750 Variable Temperature Ultra-High Vacuum Atomic Force Microscope User's Guide. *RHK Technol. Inc.* (**2007**).

25. Meyer, E., Hug, H. J. & Bennewitz, R. *Scanning Probe Microscopy, The Lab on a Tip*. (Springer, 2004). doi:10.1007/978-3-662-09801-1.

26. Gallagher, P., Lee, M., Amet, F., Maksymovych, P., Wang, J., Wang, S., Lu, X., Zhang, G., Watanabe, K., Taniguchi, T., *et al.* Switchable friction enabled by nanoscale self-assembly on graphene. *Nat. Commun.* 7, (**2016**).

27. Khare, H. S., Gosvami, N. N., Lahouij, I., Milne, Z. B., McClimon, J. B. & Carpick, R. W. Nanotribological Printing: A Nanoscale Additive Manufacturing Method. *Nano Lett.* 18, 6756–6763 (**2018**).

28. Tseng, A. A. Removing material using atomic force microscopy with single- and multiple-tip sources. *Small* vol. 7 3409–3427 (**2011**).

29. Kauzman, W. & Eyring, H. The Viscous Flow of Large Molecules. *J. Am. Chem. Soc.* 62, 3113–3125 (**1940**).

30. Spikes, H. & Tysoe, W. On the Commonality between Theoretical Models for Fluid and Solid Friction, Wear and Tribochemistry. *Tribol. Lett.* 59, 1–14 (**2015**).

31. Zhurkov, S. N. Kinetic Concept of the Strength of Solids. *Int. J. Fract. Mech.* 1, 311–323 (**1965**).

32. Schallamach, A. The velocity and temperature dependence of rubber friction. *Proc. Phys. Soc. Sect. B* 66, 386–392 (**1953**).

33. Tomlinson, G. A. CVI. A molecular theory of friction . *London, Edinburgh, Dublin Philos. Mag. J. Sci.* 7, 905–939 (**1929**).

34. Gnecco, E., Bennewitz, R., Socoliuc, A. & Meyer, E. Friction and wear on the atomic scale. *Wear* 254, 859–862 (**2003**).

35. Gosvami, N. N., Bares, J. A., Mangolini, F., Konicek, A. R., Yablon, D. G. & Carpick, R. W. Mechanisms of antiwear tribofilm growth revealed in situ by single-asperity sliding contacts. *Science (80-.).* 348, 102–106 (**2015**).

36. Felts, J. R., Oyer, A. J., Hernández, S. C., Whitener, K. E., Robinson, J. T., Walton, S. G. & Sheehan, P. E. Direct mechanochemical cleavage of functional groups from graphene. *Nat. Commun.* 6, 6467 (**2015**).

37. Raghuraman, S., Elinski, M. B., Batteas, J. D. & Felts, J. R. Driving Surface Chemistry at the Nanometer Scale Using Localized Heat and Stress. *Nano Lett.* 17, 2111–2117 (**2017**).

38. Yeon, J., He, X., Martini, A. & Kim, S. H. Mechanochemistry at solid surfaces: Polymerization of adsorbed molecules by mechanical shear at tribological interfaces. *ACS Appl. Mater. Interfaces* 9, 3142–3148 (**2017**).

39. Chen, L., Wen, J., Zhang, P., Yu, B., Chen, C., Ma, T., Lu, X., Kim, S. H. & Qian, L.

Nanomanufacturing of silicon surface with a single atomic layer precision via mechanochemical reactions. *Nat. Commun.* 9, 1542 (**2018**).

40.   Tysoe, W. On Stress-Induced Tribochemical Reaction Rates. *Tribol. Lett.* 65, 48 (**2017**).

41.   Makarov, D. E. Perspective: Mechanochemistry of biological and synthetic molecules. *J. Chem. Phys.* 144, 030901 (**2016**).

42.   Furlong, O. J., Miller, B. P., Kotvis, P. & Tysoe, W. T. Low-temperature, shear-induced tribofilm formation from dimethyl disulfide on copper. *ACS Appl. Mater. Interfaces* 3, 795–800 (**2011**).

43.   Miller, B., Furlong, O. & Tysoe, W. T. The kinetics of shear-induced boundary film formation from dimethyl disulfide on copper. *Tribol. Lett.* 49, 39–46 (**2013**).

44.   Adams, H., Miller, B. P., Furlong, O. J., Fantauzzi, M., Navarra, G., Rossi, A., Xu, Y., Kotvis, P. V. & Tysoe, W. T. Modeling Mechanochemical Reaction Mechanisms. *ACS Appl. Mater. Interfaces* 9, 26531–26538 (**2017**).

45.   Johnson, K. L. *Contact Mechanics*. (Cambridge University Press: Cambridge [Cambridgeshire], 1989). doi:10.1201/b17110-2.

46.   Johnson, K. L. The adhesion of two elastic bodies withslightly wavy surfaces. *Int. J. Solids Struct.* 32, 423–430 (**1995**).

47.   Adams, H. L., Garvey, M. T., Ramasamy, U. S., Ye, Z., Martini, A. & Tysoe, W. T. Shear induced mechanochemistry: Pushing molecules around. *J. Phys. Chem. C* 119, 7115–7123 (**2015**).

48.   Adams, H., Miller, B. P., Kotvis, P. V., Furlong, O. J., Martini, A. & Tysoe, W. T. In Situ Measurements of Boundary Film Formation Pathways and Kinetics: Dimethyl and Diethyl Disulfide on Copper. *Tribol. Lett.* 62, 12 (**2016**).

49.   Adams, H. L. Investigation of Tribochemical Reactions Using the Model System of Methyl Thiolate on Copper Foil in Ultrahigh Vacuum and Ab-Initio Calculations. (Theses and Dissertations, University of Wisconsin Milwaukee, 2017).

50.   Michaelides, A., Liu, Z. P., Zhang, C. J., Alavi, A., King, D. A. & Hu, P. Identification of general linear relationships between activation energies and enthalpy changes for dissociation reactions at surfaces. *J. Am. Chem. Soc.* 125, 3704–3705 (**2003**).

51.   Evans, M. G. & Polanyi, M. Some applications of the transition state method to the calculation of reaction velocities, especially in solution. *Trans. Faraday Soc.* 31, 875–894 (**1935**).

52.   Logadottir, A., Rod, T. H., Nørskov, J. K., Hammer, B., Dahl, S. & Jacobsen, C. J. H. The Brønsted-Evans-Polanyi relation and the volcano plot for ammonia synthesis over transition metal catalysts. *J. Catal.* 197, 229–231 (**2001**).

53.   Bligaard, T., Nørskov, J. K., Dahl, S., Matthiesen, J., Christensen, C. H. & Sehested, J. The Brønsted-Evans-Polanyi relation and the volcano curve in heterogeneous catalysis. *J. Catal.* 224, 206–217 (**2004**).

54.   Santen, R. A. V., Neurock, M. & Shetty, S. G. Reactivity theory of transition-metal surfaces: A brønsted-evans- polanyi linear activation energy-free-energy analysis. *Chem. Rev.* 110, 2005–2048 (**2010**).

55.   Loffreda, D., Delbecq, F., Vigné, F. & Sautet, P. Fast prediction of selectivity in heterogeneous catalysis from extended brønsted-evans-polanyi relations: A theoretical insight. *Angew. Chemie - Int. Ed.* 48, 8978–8980 (**2009**).

56.   Eyring, H. The Activated Complex in Chemical Reactions. *J. Chem. Phys.* 3, 107–115 (**1935**).

57. Kramers, H. A. Brownian motion in a field of force and the diffusion model of chemical reactions. *Physica* 7, 284–304 (**1940**).
58. Hänggi, P., Talkner, P. & Borkovec, M. Reaction-rate theory: Fifty years after Kramers. *Rev. Mod. Phys.* 62, 251–341 (**1990**).
59. Konda, S. S. M., Brantley, J. N., Bielawski, C. W. & Makarov, D. E. Chemical reactions modulated by mechanical stress: Extended Bell theory. *J. Chem. Phys.* 135, 164103–164108 (**2011**).
60. Avdoshenko, S. M. & Makarov, D. E. Reaction Coordinates and Pathways of Mechanochemical Transformations. *J. Phys. Chem. B* 120, 1537–1545 (**2016**).
61. Bofill, J. M., Ribas-Ariño, J., García, S. P. & Quapp, W. An algorithm to locate optimal bond breaking points on a potential energy surface for applications in mechanochemistry and catalysis. *J. Chem. Phys.* 147, (**2017**).
62. Quapp, W., Bofill, J. M. & Ribas-Ariño, J. Analysis of the Acting Forces in a Theory of Catalysis and Mechanochemistry. *J. Phys. Chem. A* 121, 2820–2838 (**2017**).
63. Quapp, W. & Bofill, J. M. Mechanochemistry on the Müller–Brown surface by Newton trajectories. *Int. J. Quantum Chem.* 118, (**2018**).
64. Remoissenet, M. & Peyrard, M. A new simple model of a kink bearing Hamiltonian. *J. Phys. C Solid State Phys.* 14, (**1981**).
65. Pearson, R. G. Symmetry Rules for Chemical Reactions. *Acc. Chem. Res.* 4, 152–160 (**1971**).
66. Metiu, H., Ross, J., Silbey, R. & George, T. F. On symmetry properties of reaction coordinates. *J. Chem. Phys.* 61, 3200–3209 (**1974**).
67. Li, Z., Thuening, T. & Tysoe, W. T. The adsorption of ethylene on Au/Pd(100) alloy surfaces. *Surf. Sci.* 646, 65–71 (**2016**).
68. Barth, J. V. Transport of adsorbates at metal surfaces: From thermal migration to hot precursors. *Surf. Sci. Rep.* 40, 75–149 (**2000**).
69. Büchner, C., Lichtenstein, L., Yu, X., Boscoboinik, J. A., Yang, B., Kaden, W. E., Heyde, M., Shaikhutdinov, S. K., Włodarczyk, R., Sierka, M., *et al.* Ultrathin silica films: The atomic structure of two-dimensional crystals and glasses. *Chem. - A Eur. J.* 20, 9176–9183 (**2014**).
70. Yao, B., Mandrà, S., Curry, J. O., Shaikhutdinov, S., Freund, H. J. & Schrier, J. Gas Separation through Bilayer Silica, the Thinnest Possible Silica Membrane. *ACS Appl. Mater. Interfaces* 9, 43061–43071 (**2017**).
71. Boscoboinik, J. A. & Shaikhutdinov, S. Exploring zeolite chemistry with the tools of surface science: Challenges, opportunities, and limitations. *Catal. Letters* 144, 1987–1995 (**2014**).
72. McCauley, R. A. Polymorphism and dielectric electric properties of Ba- and Sr-containing feldspars. *J. Mater. Sci.* 35, 3939–3942 (**2000**).
73. Boscoboinik, J. A., Yu, X., Yang, B., Fischer, F. D., Wodarczyk, R., Sierka, M., Shaikhutdinov, S., Sauer, J. & Freund, H. J. Modeling zeolites with metal-supported two-dimensional aluminosilicate films. *Angew. Chemie - Int. Ed.* 51, 6005–6008 (**2012**).
74. Zhong, J. Q., Wang, M., Akter, N., Kestell, J. D., Niu, T., Boscoboinik, A. M., Kim, T., Stacchiola, D. J., Wu, Q., Lu, D., *et al.* Ionization-Facilitated Formation of 2D (Alumino)Silicate–Noble Gas Clathrate Compounds. *Adv. Funct. Mater.* 29, (**2019**).
75. Zhong, J. Q., Wang, M., Akter, N., Kestell, J. D., Boscoboinik, A. M., Kim, T., Stacchiola, D. J., Lu, D. & Boscoboinik, J. A. Immobilization of single argon atoms in

nano-cages of two-dimensional zeolite model systems. *Nat. Commun.* 8, (**2017**).

76. Lee, K. T. & Aswath, P. B. Synthesis of hexacelsian barium aluminosilicate by a solid-state process. *J. Am. Ceram. Soc.* 83, 2907–2912 (**2000**).

77. Besnard, C., Allemand, A., David, P. & Maillé, L. Synthesis of hexacelsian barium aluminosilicate by film boiling chemical vapour process. *J. Eur. Ceram. Soc.* 40, 3494–3497 (**2020**).

78. Xu, X. & Goodman, D. W. New approach to the preparation of ultrathin silicon dioxide films at low temperatures. *Appl. Phys. Lett.* 61, 774–776 (**1992**).

79. Boscoboinik, J. A. Chemistry in confined space through the eyes of surface science - 2D porous materials. *Journal of Physics Condensed Matter* vol. 31 (**2019**).

80. Chheda, J. N., Huber, G. W. & Dumesic, J. A. Liquid-phase catalytic processing of biomass-derived oxygenated hydrocarbons to fuels and chemicals. *Angew. Chemie - Int. Ed.* 46, 7164–7183 (**2007**).

81. Climent, M. J., Corma, A. & Iborra, S. Conversion of biomass platform molecules into fuel additives and liquid hydrocarbon fuels. *Green Chem.* 16, 516–547 (**2014**).

82. Delidovich, I., Leonhard, K. & Palkovits, R. Cellulose and hemicellulose valorisation: An integrated challenge of catalysis and reaction engineering. *Energy Environ. Sci.* 7, 2803–2830 (**2014**).

83. Delidovich, I., Hausoul, P. J. C., Deng, L., Pfützenreuter, R., Rose, M. & Palkovits, R. Alternative Monomers Based on Lignocellulose and Their Use for Polymer Production. *Chem. Rev.* 116, 1540–1599 (**2016**).

84. Medlin, J. W. Understanding and controlling reactivity of unsaturated oxygenates and polyols on metal catalysts. *ACS Catal.* 1, 1284–1297 (**2011**).

85. Serrano-Ruiz, J. C. & Dumesic, J. A. Catalytic routes for the conversion of biomass into liquid hydrocarbon transportation fuels. *Energy Environ. Sci.* 4, 83–99 (**2011**).

86. Lange, J. P., Van Der Heide, E., Van Buijtenen, J. & Price, R. Furfural-A promising platform for lignocellulosic biofuels. *ChemSusChem* vol. 5 150–166 (**2012**).

87. Bohre, A., Dutta, S., Saha, B. & Abu-Omar, M. M. Upgrading Furfurals to Drop-in Biofuels: An Overview. *ACS Sustain. Chem. Eng.* 3, 1263–1277 (**2015**).

88. Mariscal, R., Maireles-Torres, P., Ojeda, M., Sádaba, I. & López Granados, M. Furfural: A renewable and versatile platform molecule for the synthesis of chemicals and fuels. *Energy Environ. Sci.* 9, 1144–1189 (**2016**).

89. Hoydonckx, H. E., Van Rhijn, W. M., Van Rhijn, W., De Vos, D. E. & Jacobs, P. A. Furfural and Derivatives. in *Ullmann's Encyclopedia of Industrial Chemistry* (2007). doi:10.1002/14356007.a12_119.pub2.

90. Liu, D., Zemlyanov, D., Wu, T., Lobo-Lapidus, R. J., Dumesic, J. A., Miller, J. T. & Marshall, C. L. Deactivation mechanistic studies of copper chromite catalyst for selective hydrogenation of 2-furfuraldehyde. *J. Catal.* 299, 336–345 (**2013**).

91. Chen, S., Wojcieszak, R., Dumeignil, F., Marceau, E. & Royer, S. How Catalysts and Experimental Conditions Determine the Selective Hydroconversion of Furfural and 5-Hydroxymethylfurfural. *Chem. Rev.* 118, 11023–11117 (**2018**).

92. O'Driscoll, Leahy, J. J. & Curtin, T. The influence of metal selection on catalyst activity for the liquid phase hydrogenation of furfural to furfuryl alcohol. *Catal. Today* 279, 194–201 (**2017**).

93. Dutta, S., De, S., Saha, B. & Alam, M. I. Advances in conversion of hemicellulosic biomass to furfural and upgrading to biofuels. *Catalysis Science and Technology* vol. 2

2025–2036 (**2012**).

94.   Iqbal, S., Liu, X., Aldosari, O. F., Miedziak, P. J., Edwards, J. K., Brett, G. L., Akram, A., King, G. M., Davies, T. E., Morgan, D. J., *et al.* Conversion of furfuryl alcohol into 2-methylfuran at room temperature using Pd/TiO2 catalyst. *Catal. Sci. Technol.* 4, 2280–2286 (**2014**).

95.   Aldosari, O. F., Iqbal, S., Miedziak, P. J., Brett, G. L., Jones, D. R., Liu, X., Edwards, J. K., Morgan, D. J., Knight, D. K. & Hutchings, G. J. Pd-Ru/TiO 2 catalyst - An active and selective catalyst for furfural hydrogenation. *Catal. Sci. Technol.* (**2016**) doi:10.1039/c5cy01650a.

96.   Pang, S. H. & Medlin, J. W. Adsorption and reaction of furfural and furfuryl alcohol on Pd(111): Unique reaction pathways for multifunctional reagents. *ACS Catal.* 1, 1272–1283 (**2011**).

97.   Wang, S., Vorotnikov, V. & Vlachos, D. G. Coverage-Induced Conformational Effects on Activity and Selectivity: Hydrogenation and Decarbonylation of Furfural on Pd(111). *ACS Catal.* (**2015**) doi:10.1021/cs5015145.

98.   Taylor, M. J., Jiang, L., Reichert, J., Papageorgiou, A. C., Beaumont, S. K., Wilson, K., Lee, A. F., Barth, J. V. & Kyriakou, G. Catalytic Hydrogenation and Hydrodeoxygenation of Furfural over Pt(111): A Model System for the Rational Design and Operation of Practical Biomass Conversion Catalysts. *J. Phys. Chem. C* 121, 8490–8497 (**2017**).

99.   Greenler, R. G., Snider, D. R., Witt, D. & Sorbello, R. S. The metal-surface selection rule for infrared spectra of molecules adsorbed on small metal particles. *Surf. Sci.* 118, 415–428 (**1982**).

100.   Vorotnikov, V., Mpourmpakis, G. & Vlachos, D. G. DFT study of furfural conversion to furan, furfuryl alcohol, and 2-methylfuran on Pd(111). *ACS Catal.* 2, 2496–2504 (**2012**).

101.   Sitthisa, S., Pham, T., Prasomsri, T., Sooknoi, T., Mallinson, R. G. & Resasco, D. E. Conversion of furfural and 2-methylpentanal on Pd/SiO2 and Pd-Cu/SiO2 catalysts. *J. Catal.* 280, 17–27 (**2011**).

102.   Sitthisa, S., Sooknoi, T., Ma, Y., Balbuena, P. B. & Resasco, D. E. Kinetics and mechanism of hydrogenation of furfural on Cu/SiO2 catalysts. *J. Catal.* 277, 1–13 (**2011**).

103.   Ormerod, R. M., Baddeley, C. J., Hardacre, C. & Lambert, R. M. Chemisorption and reactivity of furan on Pd{111}. *Surf. Sci.* 360, 1–9 (**1996**).

104.   Greenler, R. G. Infraredc study of adsorbed molecules on metal surfaces by reflection tehniques. *J. Chem. Phys.* 44, 310–315 (**1966**).

105.   Colthup, N. B., Daly, L. H. & Wiberley, S. E. Vibrational and Rotational Spectra. in *Introduction to Infrared and Raman Spectroscopy* 1–73 (1990). doi:10.1016/b978-0-08-091740-5.50004-1.

106.   Colthup, N. B., Daly, L. H. & Wiberley, S. E. Molecular Symmetry. *Introd. to Infrared Raman Spectrosc.* 109–169 (**1990**) doi:10.1016/b978-0-08-091740-5.50006-5.

107.   Colthup, N. B., Daly, L. H. & Wiberley, S. E. Major Spectra–Structure Correlations By Spectral Regions. in *Introduction to Infrared and Raman Spectroscopy* 387–481 (1990). doi:10.1016/b978-0-08-091740-5.50016-8.

108.   Davis, J. L. & Barteau, M. A. Polymerization and Decarbonylation Reactions of Aldehydes on the Pd(111) Surface. *J. Am. Chem. Soc.* 111, 1782–1792 (**1989**).

109.   Davis, J. L. & Barteau, M. A. Spectroscopic identification of alkoxide, aldehyde, and acyl intermediates in alcohol decomposition on Pd(111). *Surf. Sci.* 235, 235–248 (**1990**).

110.   Allen, G. & Bernstein, H. J. INTERNAL ROTATION: VIII. THE INFRARED AND

RAMAN SPECTRA OF FURFURAL. *Can. J. Chem.* (**1955**) doi:10.1139/v55-121.

111. Little, T. S., Qiu, J. & Durig, J. R. Asymmetric torsional potential function and conformational analysis of furfural by far infrared and Raman spectroscopy. *Spectrochim. Acta Part A Mol. Spectrosc.* 45, 789–794 (**1989**).

112. Rogojerov, M., Keresztury, G. & Jordanov, B. Vibrational spectra of partially oriented molecules having two conformers in nematic and isotropic solutions: Furfural and 2-chlorobenzaldehyde. *Spectrochim. Acta - Part A Mol. Biomol. Spectrosc.* 61, 1661–1670 (**2005**).

113. Seidel, R. W., Goddard, R., Nöthling, N. & Lehmann, C. W. In situ cryocrystallization and solid-state structures of furfural and some derivatives. *CrystEngComm* 21, 3295–3303 (**2019**).

114. Szanyi, J., Kuhn, W. K. & Goodman, D. W. CO adsorption on Pd(111) and Pd(100): Low and high pressure correlations. *J. Vac. Sci. Technol. A Vacuum, Surfaces, Film.* 11, 1969–1974 (**1993**).

115. Schoenbaum, C. A., Schwartz, D. K. & Medlin, J. W. Controlling surface crowding on a Pd catalyst with thiolate self-assembled monolayers. *J. Catal.* 303, 92–99 (**2013**).

116. Pang, S. H., Schoenbaum, C. A., Schwartz, D. K. & Medlin, J. W. Directing reaction pathways by catalyst active-site selection using self-assembled monolayers. *Nat. Commun.* 4, (**2013**).

117. Schoenbaum, C. A., Schwartz, D. K. & Medlin, J. W. Controlling the surface environment of heterogeneous catalysts using self-assembled monolayers. *Acc. Chem. Res.* 47, 1438–1445 (**2014**).

118. Kahsar, K. R., Schwartz, D. K. & Medlin, J. W. Control of metal catalyst selectivity through specific noncovalent molecular interactions. *J. Am. Chem. Soc.* 136, 520–526 (**2014**).

119. Cavin, R. K., Lugli, P. & Zhirnov, V. V. Science and engineering beyond moore's law. in *Proceedings of the IEEE* vol. 100 1720–1749 (2012).

120. Feynman, R. P. There's plenty of room at the bottom. *Eng. Sci.* 22–36 (**1960**).

121. Aviram, A. & Ratner, M. A. Molecular rectifiers. *Chem. Phys. Lett.* 29, 277–283 (**1974**).

122. Xu, B. & Tao, N. J. Measurement of single-molecule resistance by repeated formation of molecular junctions. *Science (80-.).* 301, 1221–1223 (**2003**).

123. Kiguchi, M., Miura, S., Hara, K., Sawamura, M. & Murakoshi, K. Conductance of a single molecule anchored by an isocyanide substituent to gold electrodes. *Appl. Phys. Lett.* 89, (**2006**).

124. Smits, E. C. P., Mathijssen, S. G. J., Van Hal, P. A., Setayesh, S., Geuns, T. C. T., Mutsaers, K. A. H. A., Cantatore, E., Wondergem, H. J., Werzer, O., Resel, R., *et al.* Bottom-up organic integrated circuits. *Nature* 455, 956–959 (**2008**).

125. Crommie, M. F., Lutz, C. P. & Eigler, D. M. Confinement of electrons to quantum corrals on a metal surface. *Science (80-.).* 262, 218–220 (**1993**).

126. Crommie, M. F., Lutz, C. P. & Eigler, D. M. Imaging standing waves in a two-dimensional electron gas. *Nature* 363, 524–527 (**1993**).

127. Yu, B. & Meyyappan, M. Nanotechnology: Role in emerging nanoelectronics. *Solid. State. Electron.* 50, 536–544 (**2006**).

128. Barth, J. V. Fresh perspectives for surface coordination chemistry. *Surf. Sci.* 603, 1533–1541 (**2009**).

129. Barth, J. V. Molecular Architectonic on Metal Surfaces. *Annu. Rev. Phys. Chem.* 58, 375–

407 (**2007**).

130. Whitesides, G. M. & Grzybowski, B. Self-assembly at all scales. *Science* vol. 295 2418–2421 (**2002**).

131. Boscoboinik, J. A., Calaza, F. C., Habeeb, Z., Bennett, D. W., Stacchiola, D. J., Purino, M. A. & Tysoe, W. T. One-dimensional supramolecular surface structures: 1,4-diisocyanobenzene on Au(111) surfaces. *Phys. Chem. Chem. Phys.* 12, 11624–11629 (**2010**).

132. Kestell, J., Abuflaha, R., Boscoboinik, J. A., Bai, Y., Bennett, D. W. & Tysoe, W. T. Linking gold nanoparticles with conductive 1,4-phenylene diisocyanide-gold oligomers. *Chem. Commun.* 49, 1422–1424 (**2013**).

133. Zhou, J., Acharya, D., Camillone, N., Sutter, P. & White, M. G. Adsorption structures and electronic properties of 1,4-phenylene diisocyanide on the Au(111) surface. *J. Phys. Chem. C* 115, 21151–21160 (**2011**).

134. Garvey, M., Kestell, J., Abuflaha, R., Bennett, D. W., Henkelman, G. & Tysoe, W. T. Understanding and controlling the 1,4-phenylene diisocyanide-gold oligomer formation pathways. *J. Phys. Chem. C* 118, 20899–20907 (**2014**).

135. Pordes, R., Petravick, D., Kramer, B., Olson, D., Livny, M., Roy, A., Avery, P., Blackburn, K., Wenaus, T., Würthwein, F., *et al.* The open science grid. *J. Phys. Conf. Ser.* 78, (**2007**).

136. Sfiligoi, I., Bradley, D. C., Holzman, B., Mhashilkar, P., Padhi, S. & Würthwein, F. The pilot way to Grid resources using glideinWMS. *2009 WRI World Congr. Comput. Sci. Inf. Eng. CSIE 2009* 2, 428–432 (**2009**).

137. Wisconsin–Madison, U. of. Directed Acyclic Graph. *Definitions* https://research.cs.wisc.edu/htcondor/dagman/dagman.html (2020).

138. Olson, D., Boscoboinik, A., Manzi, S. & Tysoe, W. T. Chemical Self-Assembly Strategies for Designing Molecular Electronic Circuits: Demonstration of Concept. *J. Phys. Chem. C* 123, 10398–10405 (**2019**).

139. Olson, D., Boscoboinik, A. & Tysoe, W. T. Chemical self-assembly strategies for designing molecular electronic circuits. *Chem. Commun.* 55, 13872–13875 (**2019**).

140. Boscoboinik, A. M., Manzi, S. J., Tysoe, W. T., Pereyra, V. D. & Boscoboinik, J. A. Directed Nanoscale Self-Assembly of Molecular Wires Interconnecting Nodal Points Using Monte Carlo Simulations. *Chem. Mater.* 27, 6642–6649 (**2015**).

141. López, L. G., Linares, D. H., Ramirez-Pastor, A. J., Stariolo, D. A. & Cannas, S. A. Critical behavior of self-assembled rigid rods on two-dimensional lattices: Bethe-Peierls approximation and Monte Carlo simulations. *J. Chem. Phys.* 138, (**2013**).

142. Kawasaki, K. Diffusion constants near the critical point for time-dependent ising models. I. *Phys. Rev.* 145, 224–230 (**1966**).

143. Kestell, J., Boscoboinik, J. A., Cheng, L., Garvey, M., Bennett, D. W. & Tysoe, W. T. Structural Changes in Self-Catalyzed Adsorption of Carbon Monoxide on 1,4-Phenylene Diisocyanide Modified Au(111). *J. Phys. Chem. C* 119, 18317–18325 (**2015**).

Curriculum Vitae

Title of Dissertation:

"Effect of Force and Confinement on Chemical Reaction Kinetics"

Full name:

Alejandro Miguel Boscoboinik

Place and Date of Birth:

Villa Dolores, Córdoba, Argentina

January 12th, 1989

Colleges and Universities:

2016-2020 Ph.D. in Chemistry, Department of Chemistry and Biochemistry, University of Wisconsin Milwaukee, United States.

2007-2013 Lic. in Chemistry, Department of Chemistry and Biochemistry, National University of San Luis, Argentina.

Employment:

Teaching Assistant, Department of Chemistry and Biochemistry, UWM (2016,2018-2020)

Research Assistant, Department of Chemistry and Biochemistry, UWM (2016-2019)

Awards/ Fellowships:

1. YPF fellowship, YPF Foundation (2008-2012)

2. CIN Fellowship: "Becas de Estímulo a las Vocaciones Científicas" program, Consejo Interuniversitario Nacional (CIN) (2012-2013)

3. PhD Fellowship "Beca Doctoral Tipo I" program, Consejo Nacional de Investigaciones Científicas y Técnicas (CONICET) (2014-2015)

4.   Best poster award at VI San Luis Conference on Surfaces, Interfaces and Catalysis 2018 "Studies of Mechanochemically Induced Cleavage of Methyl Thiolates on Cu(100) by Using Contact Mode AFM" (2018)

5.   UWM Chemistry Graduate Student Council travel award (2018)

Publications:

2020

   1.   Measuring and Modeling Mechanochemical Reaction Kinetics

        A.M. Boscoboinik, O. Dustin, H. Adams, N. Hopper, W.T. Tysoe

        Chem. Commun. 2020, DOI: 2020 10.1039/D0CC02992K

   2.   Structural Transformations of Molecular Furfural on Pd(111)

        A.M. Boscoboinik, H. Adams, R. Bavisotto, W.T. Tysoe

        In preparation

   3.   Infrared Spectroscopic Measurements of the Surface Chemistry and Reactivity of Furfural

        on Pd(111)

        R. Bavisotto, **A.M. Boscoboinik**, W.T. Tysoe

        In preparation

   4.   Monte Carlo Simulations of Crystalline to Glass Transitions in 2D-Materials

        A.M. Boscoboinik, S.J. Manzi, W.T. Tysoe, V.D. Pereyra, J.A. Boscoboinik

        In Preparation

2019

5. *ROI* Ionic Two-Dimensional Doped-Silicate Nanoporous Nanosheets Obtained by Delamination of a Layered Ionic Material - Patent currently filed (Boscoboinik et al., - Provisional S.N. 62/946,688 - Filed December 11, 2019 - Application Entitled "Oxide Polygonal Prism Nanocages for Trapping of Gases")

6. The structure of alanine anionic-zwitterionic dimers on Pd(111); formation of salt bridges

   L. Burkholder, S.E. Chamberlin, H. Kraffczyk, M. Michels**, A.M. Boscoboinik**, H. Adams, N. Hopper, G. Held, C. Hirschmugl, W.T. Tysoe

   Surf. Sci. 2019, DOI.org/10.1016/j.susc.2018.08.021

7. Ionization-facilitated formation of two-dimensional (alumino)silicate-noble gas clathrate compounds

   J-Q Zhong1, M. Wang, N. Akter, J.D. Kestell, T. Niu, **A.M. Boscoboinik**, T. Kim, D.J. Stacchiola, Q. Wu, D. Lu, J.A. Boscoboinik

   Adv. Funct. Mater. 2019, DOI:10.1002/adfm.201806583

8. Chemical Self-Assembly Strategies for Designing Molecular Electronic Circuits; Demonstration of Concept

   D. Olson, **A.M. Boscoboinik**, S.J. Manzi, W.T. Tysoe

   J. Phys. Chem. C. 2019, DOI: 10.1021/acs.jpcc.9b00666

9. Chemical Self-Assembly Strategies for Designing Molecular Electronic Circuits

   D. Olson, **A.M. Boscoboinik**, W.T. Tysoe

   Chem. Commun. 2019, DOI: 10.1039/C9CC07200D

2017

10. Immobilization of single argon atoms in nano-cages of two-dimensional zeolite model systems

J.-Q. Zhong, M. Wang, N. Akter, J.D. Kestell, **A.M. Boscoboinik**, T. Kim, D. J. Stacchiola, D. Lu, J.A. Boscoboinik

Nat. Commun. 2017, DOI: 10.1038/ncomms16118

2015

11. Directed Nano-scale Self-Assembly of Molecular Wires Interconnecting Nodal Points using Monte Carlo Simulations

A.M. Boscoboinik, S.J. Manzi, W.T. Tysoe, V.D. Pereyra, J.A. Boscoboinik

Chem. Mater. 2015, DOI: 10.1021/acs.chemmater.5b02413

2013

12. Mecanismo de Autoensamblaje Molecular a través de Simulaciones de Monte Carlo (Mechanism of Molecular Self-Assembly through Monte Carlo Simulations)

A.M. Boscoboinik

Licenciatura Thesis. Universidad Nacional de San Luis. 2013

Conferences and Workshops

1. National Synchrotron Light Source Triennial Review - "Trapping of Noble Gases by an Ultra-Thin Film Nano-Porous Aluminosilicate on Ru (0001)". Brookhaven National Laboratory - Poster Session Presenter (2014)

2. *Workshop on the Publishing Landscape in Applied Physical Science- "Inside Publishing". Organized by AIP Publishing and the Brookhaven Research Library. Brookhaven National Laboratory (2014)*

3. *2016 AVS Prairie Chapter Symposium. Illinois Institute of Technology (2016)*

4. *VI San Luis Conference on Surfaces, Interfaces and Catalysis, Santa Fe, Argentina - Poster Session Presenter (2018)*

5. *2018 AVS Prairie Chapter Symposium - Illinois Institute of Technology - Poster Session Presenter (2018)*

6. *2019 UWM Three Minute Thesis (3MT®) Competition - University of Wisconsin Milwaukee - Contestant (2019)*

7. *2019 UW-Milwaukee Chemistry & Biochemistry Department Research Symposium - Poster Session Presenter (2019)*

8. *79th Physical Electronics Conference, Nottingham Prize Contestant. University of Central Florida, Orlando, Florida. Oral Presenter (2019)*

9. *National Open Science Grid (OSG) User School 2019, University of Wisconsin-Madison, Madison, Wisconsin. (2019)*

10. *2019 AVS Prairie Chapter Symposium - Materials Research Lab, University of Illinois, Chicago. "Feeling the Force - Monitoring Mechanochemical Decomposition of Methyl Thiolates on Cu(100)". Oral Presenter (2019)*

11. *STLE Tribology Frontiers Conference, Chicago, Illinois. "Probing and Understanding Elementary Steps in Tribochemical Reactions" Oral Presenter (2019)*